

Theoretical analysis of free and forced dry and wet vibration of 2-way tapered hollow marine rudder with numerical verification

by

Rahul Jindal
11NA10028

A thesis submitted in partial fulfillment for the award of the degree of
Bachelor of Technology in Ocean Engineering & Naval Architecture

under the guidance of
Dr. N. Datta

Semester Eight (Spring)
Session 2014-15



Department of Ocean Engineering and Naval Architecture
Indian Institute of Technology, Kharagpur
Kharagpur, West Bengal, India
Spring 2015



Department of Ocean Engineering & Naval Architecture
Indian Institute of Technology
Kharagpur, West Bengal, India
Spring 2015

Certificate

*This is to certify that the project entitled, “**Theoretical analysis of free and forced dry and wet vibration of 2-way tapered hollow marine rudder with numerical verification**”, is a bonafide record of the work carried out by **Mr. Rahul Jindal** (Roll No. 11NA10028), under my supervision and guidance, for the partial fulfillment of the requirements for the degree of **Bachelor of Technology** in Ocean Engineering & Naval Architecture, during the academic session 2014-15, in the Department of Ocean Engineering & Naval Architecture, Indian Institute of Technology, Kharagpur.*

Prof. N. Datta
Assistant Professor
Department of Ocean Engineering & Naval Architecture
Indian Institute of Technology, Kharagpur
April 2015



Department of Ocean Engineering & Naval Architecture
Indian Institute of Technology
Kharagpur, West Bengal, India
Spring 2015

Certificate of Examination

*This is to certify that we have examined the thesis entitled, “**Theoretical analysis of free and forced dry and wet vibration of 2-way tapered hollow marine rudder with numerical verification**” submitted by **Mr. Rahul Jindal** (Roll No. 11NA10028), a Honours Degree student of Department of Ocean Engineering & Naval Architecture. We hereby accord our approval of it as a study carried out and presented in manner required for its acceptance in partial fulfillment for the degree of Bachelor of Technology, for which it has been submitted. The approval does not necessarily endorse or accept every statement made, opinion expressed or conclusion drawn, as recorded in this thesis. It only signifies the acceptance of the thesis for the purpose for which it is submitted.*

Prof. N. Datta
Supervisor

Declaration of Authorship

I, RAHUL JINDAL, declare that this thesis titled, ‘THEORETICAL ANALYSIS OF FREE AND FORCED DRY AND WET VIBRATION OF 2-WAY TAPERED HOLLOW MARINE RUDDER WITH NUMERICAL VERIFICATION’, and the work presented in it are my own. I confirm that:

- This work was done wholly or mainly while in candidature for a Bachelor degree at this Institute.
- Where any part of this thesis has previously been submitted for a degree or any other qualification at this Institute or any other institution, this has been clearly stated.
- Where I have consulted the published work of others, this is always clearly attributed.
- Where I have quoted from the work of others, the source is always given. With the exception of such quotations, this thesis is entirely my own work.
- I have acknowledged all main sources of help.
- Where the thesis is based on work done by myself jointly with others, I have made clear exactly what was done by others and what I have contributed myself.

Signed:

Date:



Department of Ocean Engineering & Naval Architecture
Indian Institute of Technology
Kharagpur, West Bengal, India
Spring 2015

Acknowledgements

Though only my name appears on the cover of this thesis, a great many people have contributed to its production. I owe my gratitude to all those people who have made this thesis possible and because of whom my graduate experience has been one that I will cherish forever.

I would like to express my deep gratitude to my B.Tech project adviser, Dr. Nabanita Datta. I have learned immensely since I became her student. She spent sufficient time instructing me how to search for relevant literature, collect and critique data, analyze problems, bring mathematical robustness in my approach, scrutinize results; and how to write a technical paper. I have been amazingly fortunate to have an adviser who gave me the freedom to explore on my own, and at the same time the guidance to recover when my steps faltered. Her patience and support helped me overcome many difficult situations in my research, and successfully complete this project.

I would also like to express my gratitude to Prof. V. Nagarajan, S.K. Satsangi and Prof. R. Datta for their valuable inputs to the project. I also thank Prof. O.P. Sha, Prof. T. Sahoo and Prof. J. Bhattacharjee for valuable inputs during presentations.

I would also like to express my deepest thanks to Mr. P K Panigrahi, Mr. Manu Korulla, Mr. P C Praveen, Mrs. Rajashree, Mr. Ganesh Kumar, Mr. Pritam and whole of NSTL team for their valuable help during the experimental work at NSTL, Vishakhapatnam. During the period of four years, many friends are helpful to color my life. I have to acknowledge all my colleagues specially Ameya and Ankit in research group, wing-mates and other friends for their assistance in many aspects that I cannot list them all because of limited space. Their support and care helped me to stay focused on my undergraduate study. I greatly value their friendship and I deeply appreciate their belief in me.

Last but not the least, I owe more than thanks to my family members which includes my parents, an elder brother and sister-in-law, for their financial support, love and encouragement throughout my life. I would like to express my heart-felt gratitude to them. Without their support, it would have been impossible for me to complete my undergraduate education seamlessly.

Rahul Jindal

Date : April, 2015

Place : IIT Kharagpur

“Do the stuff that only you can do. The urge, starting out, is to copy. And that’s not a bad thing. Most of us only find our own voices after we’ve sounded like a lot of other people. But the one thing that you have that nobody else has is you. Your voice, your mind, your story, your vision.”

Neil Gaiman

Abstract

A theoretical analysis of free dry and wet vibration of a trapezoidal, 2-way tapered, marine spade rudder, is presented. The rudder is considered as a hollow Kirchhoff's plate, with the chord section as a NACA profile. The chord length and the thickness taper from the top to the bottom, over the vertical span. The rudder is pivoted at the top, with the pivot behind the leading edge. The pivot is modelled as a combination of a translational and a rotational spring, in order to include the rigid body modes of the rudder vibration. The span-wise and chord-wise non-uniform beam vibration is first analyzed by the Rayleigh-Ritz method, in order to establish the non-uniform beam modeshapes. The span-wise beam is a linearly tapered vertical cantilever, with non-classical edge at the top and free at the bottom. The chord-wise section is a 2-span beam with the ends free, and four continuity conditions at the pivot. The non-uniform modeshapes, in either direction, is a weighted summation of the uniform beam modeshapes, which also satisfy the boundary/continuity conditions. They now act as admissible spatial functions to the plate vibration, which is analysed by the Galerkin's method. Eigen value analysis generates the plate natural frequencies. A weighted superposition of the product of the beam modeshapes, in either direction, generates the plate modeshapes. Alternately, uniform beam modeshapes are used as admissible functions into the Galerkin's method for the plate natural frequencies and modeshapes. The natural frequencies are generated for various positions of the rudder stock along the chord length. The pivot conditions (in both translational and rotational rigid body degrees of freedom) influence the prominence of the rigid-body modeshapes. This is followed by the wet vibration analysis of the rudder. First, two-dimensional strip theory is used to generate the added mass of each chord section. Constant strength source distribution technique is used to generate the added mass and added mass moment in sway and yaw, respectively, of a 2D aerofoil. Each flexural and torsional mode is associated with its own added mass. Various empirical corrections are done to account for the three-dimensional flow. Finally, 3D panel method is used to generate the modal added masses, and hence the wet natural frequencies. This theoretical study has been verified with numerical analysis using the commercial tool ANSYS. The work is further extended to an experimental analysis of propeller-induced-vibration.

Contents

Certificate	i
Certificate of Examination	ii
Declaration of Authorship	iii
Acknowledgements	iv
Abstract	vi
List of Figures	x
List of Tables	xii
Abbreviations	xiii
Physical Constants	xiv
Nomenclature	xv
1 Introduction	1
1.1 Overview	1
1.2 Literature Review	2
1.3 Gap in literature	2
1.4 Motivation	3
1.5 Present Work	4
1.5.1 Dry vibration	4
1.5.2 Wet vibration	4
2 Problem Definition	6
2.1 Chord-wise beam vibration	7
2.2 Span-wise beam vibration	9
3 Analysis Methodology	11

3.1	Dry vibration	11
3.1.1	Non-uniform beam vibration	11
3.1.2	Plate Vibraion	13
3.2	Wet Vibration : 2D	16
3.2.1	Theoretical technique (Potential flow theory)	17
3.2.1.1	Sway	17
3.2.1.2	Yaw	18
3.2.2	Numerical technique	18
3.2.3	3D Green's function technique	19
3.2.4	Numerical software : ANSYS	20
3.3	Forced Vibration	21
3.3.1	Spade Rudder torque calculations by Harrington method	21
3.3.2	Mode Summation Method	23
3.3.3	Forced wet plate vibration - Dynamic analysis	24
3.3.4	Forced plate vibration - Static analysis	25
4	Results	27
4.1	Rudder model with non-classical pivot (Rudder-I)	27
4.1.1	Dry Vibration	28
4.1.1.1	Non-uniform beam modeshapes	28
4.1.1.2	Plate natural frequencies and modeshapes	31
4.1.1.3	Numerical analysis : ANSYS 15	37
4.1.2	Wet Vibration	38
4.2	Full-scale rudder with classical pivot (Rudder-II)	39
4.2.1	Dry vibration	40
4.2.1.1	Beam Modeshapes	40
4.2.1.2	Plate Modeshapes and frequencies	41
4.2.2	Wet vibration	43
4.2.2.1	Wet free vibration	43
4.2.2.2	Wet forced vibration	44
5	Work Extension : Experimental Work on Rudder - III	47
5.1	Stiffened Rudder Model	48
5.2	Propeller Characteristics	49
5.3	Experimental Procedure	50
5.3.1	Experimental Setup	50
5.3.2	Free Dry Vibration	50
5.3.3	Free Wet Vibration	52
5.3.4	Forced Wet Vibration in Propeller Wake	54
6	Discussion, Conclusion and Future Work	61
6.1	Discussion	61
6.1.1	Rudder - I	61
6.1.2	Rudder - II	61
6.1.3	Rudder - III	62
6.2	Conclusion	62
6.2.1	Rudder - I	62

6.2.2 Rudder - II	62
6.2.3 Rudder - III	63
6.3 Future Work	63
6.3.1 Theoretical	63
6.3.2 Numerical	64
6.3.3 Experimental	64
A Coefficient Matrices	65
A.1 Chord-wise 2-span beam coefficient matrix	65
A.2 Span-wise beam coefficient matrix	66
B Joukowski Transformation	67
B.1 Average chord section thickness	67
B.2 Slenderness ratio in beams	68
B.3 Area of the aerofoil	68
B.4 Centroid of the aerofoil	68
B.5 Moment of inertia of the aerofoil in yaw (about CG)	68
B.6 Normal vector on aerofoil perimeter	69
C Galerkin II : Expansion of biharmonic operator	70
D Source Distribution Technique	71
D.1 3D Constant-Strength Source Distribution Technique	71
D.2 2D Constant-Strength Source Distribution Technique	73
Bibliography	74
Consequent publications	74
About the author	77
Endorsement	78

List of Figures

1.1	Rudder in the propeller wake	1
1.2	Rudder models considered in this work	5
2.1	Rudder model	6
2.2	Rudder section at root chord	7
2.3	Rudder span mathematical model	9
3.1	Rudder model mesh in ANSYS	20
3.2	Hydrodynamic force variation over rudder span for various rudder angles .	23
4.1	Chord-wise beam modeshapes	28
4.2	Frequency (Hz) comparison of non-uniform chord-wise modeshapes for different pivot positions	29
4.3	Span-wise beam modeshapes	30
4.4	Frequency (Hz) comparison of non-uniform span-wise modeshapes for different taper ratios	30
4.5	Thickness distribution of rudder	31
4.6	Variation of flexural rigidity	32
4.7	First (1,1) modeshape	34
4.8	Second (2,1) modeshape	34
4.9	Third (3,1) modeshape	34
4.10	Fourth (1,2) modeshape	35
4.11	Fifth (2,2) modeshape	35
4.12	Sixth (3,2) modeshape	35
4.13	Seventh (1,3) modeshape	36
4.14	Eighth (2,3) modeshape	36
4.15	Ninth (3,3) modeshape	36
4.16	Added mass w.r.t. plate mode number	39
4.17	Span-wise beam modeshapes (model scale 1 : 10)	40
4.18	Chord-wise beam modeshapes (model scale 1 : 10)	41
4.19	Full scale rudder mode shapes	42
4.20	Dry and wet natural frequencies	44
4.21	Maximum deflection and Stress components spatial distribution	45
4.22	Steady deflection and Normal stress in X-direction spatial distribution . .	46
4.23	Steady Normal stress in Y-direction and Twisting Stress about X or Y spatial distribution	46
5.1	Rudder - III	47
5.2	Rudder Model Geometry	48

5.3	Thrust coefficient, Torque coefficient and open water efficiency characteristics versus advance ratio	49
5.4	Experimental configuration for forced wet vibration test	50
5.5	Accelerometer Position in Free Dry Vibration	51
5.6	Acceleration results in frequency domain for configuration D3A	51
5.7	Acceleration results in frequency domain for configuration D3C	51
5.8	Acceleration results in frequency domain for configuration D5A	52
5.9	Acceleration results in frequency domain for configuration D5C	52
5.10	Accelerometer Position in Free Wet Vibration	52
5.11	Acceleration results in frequency domain for configuration W3A	53
5.12	Acceleration results in frequency domain for configuration W3C	53
5.13	Acceleration results in frequency domain for configuration W5A	53
5.14	Acceleration results in frequency domain for configuration W5C	54
5.15	Accelerometer Position in Wet forced Vibration	54
5.16	Rudder in the wake of propeller during wet vibration test under propeller gust at NSTL, Vizag	55
5.17	Acceleration results in frequency domain for configuration 1B	56
5.18	Acceleration results in time domain for configuration 1B	56
5.19	Acceleration results in frequency domain for configuration 2C	56
5.20	Acceleration results in time domain for configuration 2C	56
5.21	Acceleration results in frequency domain for configuration 3B	57
5.22	Acceleration results in time domain for configuration 3B	57
5.23	Acceleration results in frequency domain for configuration 4A	57
5.24	Acceleration results in time domain for configuration 4A	57
5.25	Acceleration results in frequency domain for configuration 5A	58
5.26	Acceleration results in time domain for configuration 5A	58
5.27	Acceleration results in frequency domain for configuration 5D	58
5.28	Acceleration results in time domain for configuration 5D	58
5.29	Acceleration results in frequency domain for configuration 3B at non-zero speed	59
5.30	Acceleration results in time domain for configuration 3B at non-zero carriage speed	59

List of Tables

2.1	Geometric and Material Properties	7
3.1	Basic KCS ship data	21
3.2	Normal force and hydrodynamic torque on the rudder, at various rudder angles	22
4.1	Family of problems for rudder I	27
4.2	Weight matrix in chord-wise direction	29
4.3	Weight matrix in span-wise direction	31
4.4	Dry frequencies of Rudder I from theoretical analysis	32
4.5	Modal participation in non-uniform beam vibration	33
4.6	Dry plate vibration frequency variation in ANSYS	37
4.7	Joukowski transformation error analysis	38
4.8	3D added mass by strip theory	39
4.9	Family of problems for Rudder II	40
4.10	Dry frequencies of Rudder-II with classical pivot	42
4.11	Modal participation of rudder with classical pivot	43
4.12	Maximum Dynamic Stresses and Deflection for different rudder angles . .	44
4.13	Maximum Steady Stresses and Deflection for different rudder angles . .	46
5.1	Family of problems for Rudder III	47
5.2	Rudder full-scale and model information	48
5.3	Propeller Model Particulars	49
5.4	Average Thrust, Torque and RPM data from dynamometer	55
5.5	Comparison of free dry and wet natural frequencies for different configuration of accelerometer	60
5.6	Comparison of excitation frequencies with the blade passing frequencies (PIV) for different configuration of accelerometer	60

Abbreviations

PIV Propeller Induced Vibration

FEM Finite Element Method

RR Rayleigh Ritz

AVMI Added Virtual Mass Increment

Physical Constants

Modulus of elasticity	$E = 2.1 \times 10^{11} \text{ Nm}^{-2}$
Bulk modulus	$B = 1.6667 \times 10^{11} \text{ Nm}^{-2}$
Shear modulus	$G = 7.6923 \times 10^{10} \text{ Nm}^{-2}$
Density of steel	$\rho = 7850 \text{ kgm}^{-3}$
Density of fresh water	$\rho_{fw} = 1000 \text{ kgm}^{-3}$
Density of sea water	$\rho_{sw} = 1025 \text{ kgm}^{-3}$
Coefficient of thermal expansion	$= 1.2 \times 10^{-5} \text{ C}^{-1}$
Specific heat	$= 434 \text{ kg}^{-1}\text{C}^{-1}$
Thermal conductivity	$= 60.5 \text{ Wm}^{-1}\text{C}^{-1}$
Resistivity	$= 1.7 \times 10^{-7} \text{ ohm m}$
Poisson's ratio	$\mu = 0.3$

Nomenclature

x	Space variable along span	m
y	Space variable along chord	m
t	Time variable	m
L	Span length	m
E	Modulus of elasticity	Nm^{-2}
L	Span length	m
ρ	Density of material	kgm^{-3}
m_s	Mass per unit length (Span-wise)	kgm^{-1}
m_c	Mass per unit length (Chord-wise)	kgm^{-1}
m	Mass per unit plate area	kgm^{-2}
I_s	2^{nd} moment of section for span-wise beam vibration	m^4
I_c	2^{nd} moment of section for chord-wise beam vibration	m^4
$\varphi_c(y)$	Chord-wise uniform beam mode shape	
$\varphi_s(x)$	Span-wise uniform beam mode shape	
$\phi_c(y)$	Chord-wise non-uniform beam mode shape	
$\phi_s(x)$	Span-wise non-uniform beam mode shape	
β_s	Frequency parameter (span-wise)	m^{-1}
β_c	Frequency parameter (chord-wise)	m^{-1}
$\Phi(x, y)$	Rudder plate mode shapes	
$\Psi(x, y; t)$	2D Velocity potential	m^2s
K_T	Translational spring constant	Nm^{-2}
$K_{\theta c}$	Rotational chord-wise spring constant	N-m
$K_{\theta s}$	Rotational span-wise spring constant	N-m
a_{ij}^s	Coefficient of uniform beam modeshapes (span-wise)	
a_{ij}^c	Coefficient of uniform beam modeshapes (chord-wise)	
A_{ij}^k	Coefficient for k^{th} rudder plate modeshapes	

$F_P(t)$	Principal coordinate for plate deflection	
$F(t)$	Principal coordinate for beam deflection	
e	Fineness ratio of aerofoil	
$P(x, y, z)$	Field point in 3D source distribution	
$Q(\xi, \eta, \zeta)$	Source point in 3D source distribution	
$\Psi(Q)$	Source potential	m^2s
$G_{PQ}(x, y; \xi, \eta)$	Green's function	m^2s
C_R, C_T, C_M, b	Root chord, Tip chord, Mean Chord, half-chord	m
λ	Taper ratio	
$D(x, y)$	Plate flexural rigidity	Nm
$h(x, y)$	Plate thickness	m
$Z(x, y; t)$	Plate deflection	m
$u(y, t)$	Span-wise beam deflection	m
$v(x, t)$	Chord-wise beam deflection	m
μ	Poisson's ratio	
h_m	Mean thickness of mean chord section	m
D_x, D_y, D_{xy}	Components of plate flexural rigidity	Nm
δ	Rudder angle	degrees
σ_x	Normal stress in span-wise direction	Nm^{-2}
σ_y	Normal stress in chord-wise direction	Nm^{-2}
τ_{xy}	Shear stress in twisting direction	Nm^{-2}

Dedicated to my loved ones....

Chapter 1

Introduction

1.1 Overview

Flexural dynamics of marine rudders has become an increasingly important area of research in the last few decades. Rudder flutter is a major concern in operating vessels, pressing on the need for sound structural design of the rudder and its pivot. The rudder is exposed to the oscillating hydrodynamic loads, in the turbulent propeller slipstream behind the ship; which causes the rudder to vibrate in its translational and torsional modes.

The excitation frequency of this **propeller-**

induced vibration (PIV) is of the order of propeller shaft frequency into the number of propeller blades. Along with the flexural modes, rigid body modes mainly in sway and yaw (w.r.t.the ship coordinate system), also get excited due to PIV. The rudder is often likely to suffer flutter, a non-linear parasitic phenomenon, which involves a combination of flexural and rigid-body translational and twisting modes of the rudder. The rudder generally operates fully under water (in the Loaded Departure, Loaded Arrival and Light Departure conditions), which leads to the geometry-dependent hydrodynamic inertia, which reduces the natural frequencies of structure. In the lightship (Light Arrival) condition, the rudder operates in a partially submerged condition. The rudder free wet natural frequency should not resonate with PIV frequency, which leads to detrimental large amplitude vibrations.



FIGURE 1.1: Rudder in the propeller wake

1.2 Literature Review

Eftekhari and Jafari (2013)[1] developed an accurate variational form to study the vibration problems of variable thickness thin plates with edge elastically restraint against both rotation and translation. Kannamwar and Datta (2014)[2] did the vibration analysis of a fully one-sided clamped spade rudder by theoretical, numerical and analytical means. Liu and Xing (2011)[3] obtained the exact closed-form solution of orthotropic Mindlin's plates by using the separation-of-variables method, and compared the solutions with those of the isotropic plates. Leissa (1973) [4] studied the free vibration of rectangular plates with 21 different classical edge conditions. El-Sayad and Ghazy (2012)[5] developed the RayleighRitz method for free vibration of Mindlin's trapezoidal plates by accounting the effect of trapezoidal shape itself into the uniform beam modesshapes. Gupta and Khanna (2007)[3] studied the effect of linear thickness variation in the both directions on the vibration of visco-elastic rectangular plate having clamped boundary conditions on all the four edges. Bae et al(2003)[6] studied the non-linear characteristics of an aircraft wing with a control surface by double-hybrid method. Bahmyari and Rahbar-Ranji (2011)[7] investigated the vibration behavior of a thin square orthotropic plate resting on non-uniform elastic foundation with varying thickness. Gupta et al (1995) [8] analyzed the vibrations of non-uniform plates with exponentially varying thickness by using the Chebychev polynomials. Ergin and Ugurlu (2002)[9] analyse the dynamic behavior i.e. natural frequencies and modesshapes of the cantilever plates partially in contact with the fluid. For wet plate vibration study, McCormick and Caracoglia (2004)[10] modified the 3D added mass of a rectangular plates obtained with strip theory by including the three-dimensional correction factors derived from the theory of Yu (1945) using thin airfoil assumptions of Theordorsen (1935). Yadykin at al (2002) [11] studied the fundamental properties of added mass of a flexible plate oscillating in fluid.

1.3 Gap in literature

- Investigations of marine rudder flexural dynamics have been limited to numerical and rare experimental work
- Modelling of a marine rudder as a plate has hardly been attempted, given its structural complexity.
- The pivot condition of spade rudder is not analysed in any form as of now in any literature.
- A orthotropic plate with varying thickness along with the taper on both sides (trapezoidal plate) is not analysed.

- The vibration analysis of a marine spade rudder in the wake of propeller gust, is not done till now.
- The formulation of the spatial distribution of the external forcing on the rudder due to propeller wake is not present in literature.

The literature for the forced wet plate vibration for concerned boundary conditions is not available, therefore it can be of interest to naval architects while designing the marine rudders while considering wake loading of the propeller.

1.4 Motivation

The following research questions may be asked after the above literature study.

1. Can a marine rudder be modelled as a plate?
2. Is the marine rudder a thick plate or a thin plate?
3. What are the boundary conditions of the rudder?
4. How is the pivot modelled for the theoretical plate vibration analysis?
5. How is the two-way taper in the rudder geometry considered for the plate vibration analysis?
6. What is the added mass virtual mass increment of a submerged rudder and how it is calculated?

Research in the theoretical analysis of marine rudder vibration is limited, given the complex rudder geometry, and the increasingly sophisticated pivot and support structures. the combined complications of the problem attempted in this work are as follows

- The rudder is not a uniform structure but has a two way taper.
- The rudder is hollow with intermediate stiffeners in it.
- The pivot may or may not allow for the rigid-body dynamics of the rudder, depending on the stock length and its fixity.

Hydrodynamic analysis of the rudder is also a big challenge given that the rudder acts in the extremely turbulent propeller slipstream. The spatial distribution of the hydrodynamic load on the rudder plan-form, at various rudder angles, follows a complex estimation process. The fundamental frequency of the rudder, inclusive of the fluid inertia, differs for different drafts of the ship. The rudder should be designed such that, its wet natural frequency of the rudder should not match with the propeller-induced-vibration $\pm 5\%$

1.5 Present Work

In this work, the free dry and wet vibration of a hollow, two-way tapered, trapezoidal spade rudder with three different structural configurations. The overview of all the three models is shown in **Fig. 1.2**.

1. First model (Rudder I) : In the *first* model, the marine spade rudder is considered to have a non-classical pivot at root chord. Here, rudder stock is considered to be piercing along the total span and is clamped at root chord by translational and torsional springs. It has been scaled down to 1:10 from the actual model.
2. Second model (Rudder II) : In the *second* model, rudder is considered to be clamped by classical pivot at root chord and considered to be a FFFF plate and the deflection and slope at the pivot is considered to be zero. It's scale is same as that of full scale rudder.
3. Third model (Rudder III) : The *third* model, the rudder stock goes till the mean chord and the bulkheads are present. It is scaled down by 1:31.25 from the actual KCS (Korean Container Ship) rudder.

1.5.1 Dry vibration

The rudder is considered as a Kirchhoff's plate, ignoring shear deformation and rotary inertia. The curvature of the hollow sheet is very small, and the average thickness in span-wise direction obeys the 'pure' bending criteria. The rudder is *not* a 'slender' beam in the chord-wise direction. However, since the rudder is hollow, it is approximated as an Euler-Bernoulli beam. Free dry vibration analysis of rudder with non-classical boundary conditions, is done by **Galerkin's method**. Two methodologies are followed here. In the *first* method, the non-uniform beam modeshapes, in either direction, are estimated by the **Rayleigh-Ritz (R-R) method**, which act as the admissible functions to the plate modeshapes. Here, the plate flexural rigidity has three components: D_x , D_y , and D_{xy} . In the *second* method, the uniform beam modeshapes themselves act as admissible functions in the Galerkin's method, bypassing the beam-wise R-R method. Here, the plate flexural rigidity is considered as a continuous bicubic function along the span and the chord, $D(x,y)$.

1.5.2 Wet vibration

After the dry vibration analysis, the dynamic inertia of the sea water surrounding the rudder is *included* in the free vibration governing differential equation. This decreases the natural frequencies of the rudder considerably. The radiation force, of the otherwise calm fluid, is in-phase with the acceleration of the structure. The radiation damping

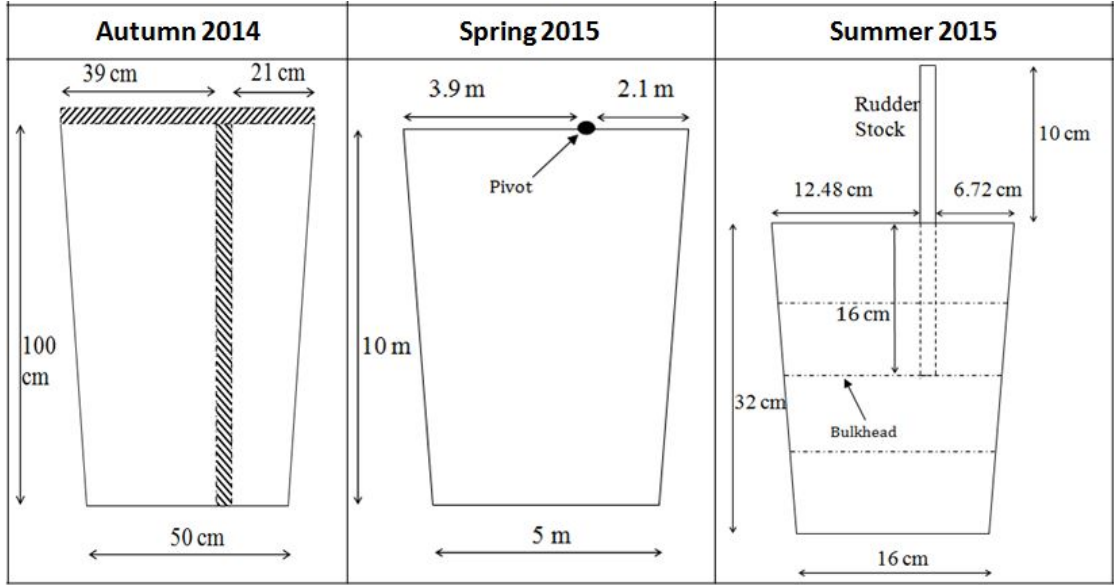


FIGURE 1.2: Rudder models considered in this work

of the water surface waves can be neglected. The fully immersed rudder vibrates under water, without interfering with the calm water surface. The partially submerged rudder, inclusive of the fluid inertia, interferes with the air-water interface, but still vibrates at a frequency large enough to keep the water surface calm. The high frequency limit of the combined free surface boundary condition of the fluid, is satisfied to create a *double body problem*, which causes the rudder to act as if vibrate in an infinite fluid domain.

The added mass (fluid inertia force per unit body acceleration) of Kirchhoff's plate is calculated by using the **2D Strip theory**. The 2D added mass of the aerofoil section, in both sway and roll, are calculated by theoretical potential flow hydrodynamics, and verified by the 2D source distribution technique. However, Strip theory is valid for longish bodies, where each strip can be assumed to be hydrodynamically independent of the adjacent one. Since the aspect ratio of the rudder (span-to-chord ratio) is 1:0.55, the 3D nature of the flow cannot be ignored. 3D correction factors are included (Van Eysden and Sader (2006)[12]), which depend both on the flexural modes and torsional modes; in contrast to the 3D corrections by Yu (1945), and McCormick and Caracoglia (2004)[10], which are independent of mode number. The Strip theory over-predicts the fluid kinetic energy. The 3D source distribution technique is done in order to calculate the 3D added mass associated with each plate modeshape (derived from the Galerkin's method), and estimate the corresponding decrease in the wet natural frequencies of the rudder. For the third rudder model, only experimental work is done at Naval Science and Technological Laboratory, DRDO; Vishakhapatnam, Seemandhra.

Chapter 2

Problem Definition

A two-way tapered hollow marine spade rudder is modelled as a Kirchhoff's plate, shown in **Fig 2.1**, with geometric and material properties as in **Table 2.1**. The scale ratio of the model to the rudder is 1:10. The span length 'L' of rudder is 1m. The root chord C_R is 0.6 m, while the tip chord C_T is 0.5 m. The chord-wise cross section of the rudder is a NACA0018 aerofoil, i.e. the maximum thickness-to-chord ratio is 0.18, at any given section. The planform of the rudder tapers linearly from the root to the tip. In order to have the same aerofoil profile in every chord-wise cross-section, the thickness of the rudder plate also decreases linearly downwards. Thus, the span-wise cross section of the rudder is a linearly tapered cantilever. The pivot of the rudder is located at the root chord (i.e. at the top), at 35% of the root chord length behind the leading edge. It is modelled as a combination of translational and rotational constraints. The rudder is hollow inside, with the enclosing peripheral metal sheet thickness of 3 mm. As the chord-wise beam is hollow, it is assumed that the shear deformation and the rotary inertia will be minimal. The thin metal thickness in the cross-section provides negligible shear area. Also, its moment of inertia in bending is negligible, providing minimal rotational inertia of each infinitesimal beam element along the length of the beam. Thus, both beams are modelled as Euler-Bernoulli beams, whose weighted combination leads to a Kirchhoff's plate. For simplicity, the stiffeners/bulkheads inside the hollow rudder are not considered in this analysis.

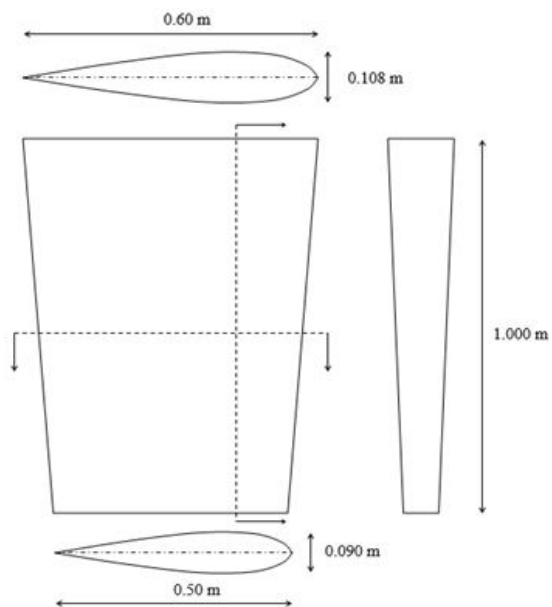


FIGURE 2.1: Rudder model

TABLE 2.1: Geometric and Material Properties

Span	1	<i>m</i>
Root chord	0.6	<i>m</i>
Tip chord	0.5	<i>m</i>
Aerofoil profile	NACA0018	
Taper ratio	1.2	
Pivot position	35% from the leading edge	
Material	Mild steel	
Density	7850	<i>kgm</i> ⁻³
Sheet thickness	3	<i>mm</i>

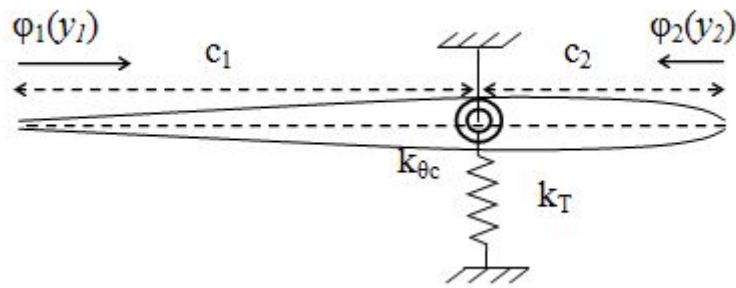


FIGURE 2.2: Rudder section at root chord

This helps us avoid a non-mathematical distribution of the mass and stiffness of the rudder along either axis. Stiffeners cause sudden sharp discontinuities in the mass and stiffness distributions, both along the span and along the chord.

2.1 Chord-wise beam vibration

In the chord-wise direction, a NACA0018 aerofoil shape is considered as a non-uniform Euler-Bernoulli beam, with a non-classical pivot located at 65% of its length from trailing edge. The pivot is modelled as a combination of a translational spring (spring constant K_T (N/m) and a torsional spring (spring constant $K_{\theta c}$ ($N\cdot m/rad$)), as shown in **Fig 2.2**.

First, the uniform beam modeshapes, along the span and the chord, need to be established. The governing differential equation, for free vibration of a uniform Euler-Bernoulli beam, along the chord is:

$$m_c \frac{\partial^2 v(y; t)}{\partial t^2} + EI_c \frac{\partial^4 v(y; t)}{\partial y^4} = 0 \quad (2.1)$$

Here, m_c is the mass per unit length (kg/m) and EI_c is the flexural rigidity (Nm^2) along the chord-section of the rudder. The total mass is calculated by considering the

perimeter of the aerofoil section, multiplied by the metal thickness t (mm) and the metal density ρ_s (kg/m^3); and integrating it over the span length L.

By applying the method of separation of variables, the dynamic deflection $v(y,t)$ in Eq. 2.1 is written as:

$$v(y,t) = \sum_{j=1}^{\infty} \varphi_{1j}^c(y) f_j(t) \quad \text{for } 0 < y < l \quad (2.2)$$

$$v(y,t) = \sum_{j=1}^{\infty} \varphi_{2j}^c(y-l) f_j(t) \quad \text{for } l < y < B \quad (2.3)$$

Here, φ_1^c and φ_2^c represent the modeshapes of trailing and leading edge, respectively, and $f(t)$ is the time-varying component. The 2-span modeshape is a linear combination of $\varphi_1^c(y)$ and $\varphi_2^c(y)$, satisfying the *four* boundary and the *four* continuity conditions at the pivot. The bending moment and shear force at the ends vanish at the leading edge and at the trailing edge as in Eq.2.4. Therefore, the boundary conditions are expressed as:

$$\frac{d^2\varphi^c(0)}{dy^2} = 0; \quad \frac{d^3\varphi^c(0)}{dy^3} = 0; \quad \frac{d^2\varphi^c(l)}{dy^2} = 0; \quad \frac{d^3\varphi^c(l)}{dy^3} = 0 \quad (2.4)$$

At the pivot, the continuity conditions are:

$$\varphi_1^c(l) = \varphi_2^c(0); \quad \frac{d\varphi_1^c(l)}{dy} = -\frac{d\varphi_2^c(0)}{dy} \quad (2.5)$$

$$EI \frac{d^3\varphi_1^c(l)}{dy^3} - \frac{d^3\varphi_2^c(0)}{dy^3} = K_T \varphi_1^c(l) \quad (2.6)$$

$$EI \frac{d^2\varphi_1^c(l)}{dy^2} - \frac{d^2\varphi_2^c(0)}{dy^2} = K_{\theta c} \frac{d\varphi_1^c(l)}{dy} \quad (2.7)$$

Eq. 2.5-2.7 represent the continuity in deflection and slope, and discontinuities in the bending moment and the shear force, respectively. The shear force discontinuity equals the restoring force exerted by translational spring; and the bending moment discontinuity equals the torsional restoring moment exerted by torsional spring. The general expression of piece-wise modeshapes are expressed as:

$$\varphi_1^c(y) = A_1 \cos(\beta_y y) + A_2 \sin(\beta_y y) + A_3 \cosh(\beta_y y) + A_4 \sinh(\beta_y y) \quad (2.8)$$

$$\varphi_2^c(y) = B_1 \cos(\beta_y y) + B_2 \sin(\beta_y y) + B_3 \cosh(\beta_y y) + B_4 \sinh(\beta_y y) \quad (2.9)$$

By substituting Eq. 2.8, 2.9 in Eq. 2.4-2.7, we arrive at:

$$[M]\{AB\} = 0 \quad (2.10)$$

Here,

$$\{AB\} = [A_1 \quad A_2 \quad A_3 \quad A_4 \quad B_1 \quad B_2 \quad B_3 \quad B_4]^T \quad (2.11)$$

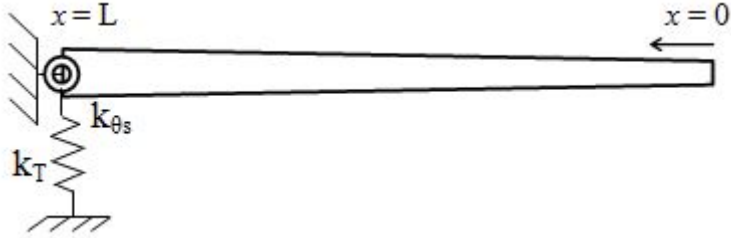


FIGURE 2.3: Rudder span mathematical model

$$[M] = \begin{bmatrix} M_{11} & \dots & M_{18} \\ \vdots & \ddots & \vdots \\ M_{81} & \dots & M_{88} \end{bmatrix} \quad (2.12)$$

In Eq. 2.12, each of the $8 \times 8 = 64$ terms, are shown in **Appendix A.1**. For a non-trivial solution, the determinant of square matrix $[M]$ equals zero, which gives the frequency equation of the two-span beam. This is satisfied by an infinite number of distinct frequency parameters, each corresponding to a unique 2-span modeshape. The Eigen vector of this matrix gives the linear dependence between φ_1^c and φ_2^c , thereby generating the uniform 2-span beam modeshape. These elementary modeshapes act as *admissible functions* to the non-uniform beam chord-wise modeshapes, which satisfy the same boundary and continuity conditions.

2.2 Span-wise beam vibration

In the span-wise direction, a linearly tapered beam is considered, with non-classical fixity at one end, and the other end free. The fixed end is modelled as combination of a translational and a torsional spring (**Fig 2.3**). The governing differential equation, of free vibration of uniform Euler-Bernoulli beam, is:

$$m_s \frac{\partial^2 u(x; t)}{\partial t^2} + EI_s \frac{\partial^4 u(x; t)}{\partial x^4} = 0 \quad (2.13)$$

Here, m_s is the mass per unit length (kg/m) and EI_s is the flexural rigidity (Nm^2) along the span-section of the rudder.

By the method of separation of variables, the flexural displacement $u(x, t)$ in Eq. 2.13 can be written as

$$u(x, t) = \sum_{j=1}^{\infty} \varphi_j^s(x) f_j(t) \quad (2.14)$$

Here $\varphi_j^s(x)$ is the j^{th} uniform modeshape in span-wise direction satisfying the following boundary conditions Eq. (2.15-2.16) defined as:

$$\frac{d^2 \varphi_j^s(0)}{dx^2} = K_{\theta s} \frac{d \varphi_j^s(0)}{dx}; \quad \frac{d^3 \varphi_j^s(0)}{dx^3} = K_T \varphi_j^s(0) \quad (2.15)$$

$$\frac{d^2\varphi^s(L)}{dx^2} = 0; \quad \frac{d^3\varphi^s(L)}{dx^3} = 0 \quad (2.16)$$

The general expression of the span-wise uniform modeshape is:

$$\varphi^s(x) = C_1 \cos(\beta_x x) + C_2 \sin(\beta_x x) + C_3 \cosh(\beta_x x) + C_4 \sinh(\beta_x x) \quad (2.17)$$

Substituting value of $\varphi^s(x)$ from Eq. 2.17 in Eq. 2.15 and in Eq. 2.16, we arrive at homogeneous system of equations as follows:

$$[N]\{C\} = 0 \quad (2.18)$$

Here,

$$\{C\} = [C_1 \quad C_2 \quad C_3 \quad C_4]^T \quad (2.19)$$

$$[N] = \begin{bmatrix} N_{11} & \dots & N_{14} \\ \vdots & \ddots & \vdots \\ N_{41} & \dots & N_{44} \end{bmatrix} \quad (2.20)$$

In Eq. 2.20, each of the $4 \times 4 = 16$ terms, are shown in the **Appendix A.2**. For a non-trivial solution, the determinant of square matrix equals zero, which give the frequency equation of the uniform beam. This equation is satisfied by an infinite number of distinct frequency parameters, each corresponding to a unique modeshape. These elementary modeshapes act as *admissible functions* to the non-uniform span-wise beam modeshapes, which satisfies the same boundary conditions.

Chapter 3

Analysis Methodology

This chapter deals with the detailed analysis procedure for the free dry and wet vibration of the rudder. The free vibration analysis of the spade rudder is done for the dry condition, to first find the dry natural frequencies and modeshapes. The dry vibration analysis involves the Rayleigh-Ritz method to first generate the non-uniform beam modeshapes along the span and the chord. They are then combined into the energy based Galerkin's method, to analyse the Kirchhoff's plate vibration. This generates the dry plate natural frequencies and modeshapes. These modeshapes are used to find the corresponding added mass distribution for sway and yaw modes. As the rudder is usually underwater, the free wet vibration analysis is done by considering the effect of the added virtual mass increment (AVMI), which lowers the frequencies. The pulsating radiation pressure of the surrounding water is in phase with the flexural acceleration of the structure.

3.1 Dry vibration

The spade rudder is considered as a weighted spatial combination of two perpendicular beam modes in the chord-wise and the span-wise directions. Thus, the free dry vibration analyses of both are separately done, to find the non-uniform modeshapes and frequencies. The beam modeshapes are further used to analyze the dry vibration of the plate by the Galerkin's method.

3.1.1 Non-uniform beam vibration

The uniform beam modeshapes can be obtained by solving the governing differential equation of Euler-Bernoulli's beam, after applying the appropriate boundary and continuity conditions both in span and chord-wise directions (Chapter 2). However, due to the varying the cross-sections, the mass and stiffness distributions of both the beams vary over their respective lengths. The governing differential equation, for free vibration

of a non-uniform chord-wise and span-wise Euler-Bernoulli beams, respectively, are as follows:

$$m_c(y) \frac{\partial^2 v(y; t)}{\partial t^2} + EI_c(y) \frac{\partial^4 v(y; t)}{\partial y^4} = 0; \quad m_s(x) \frac{\partial^2 u(x; t)}{\partial t^2} + EI_s(x) \frac{\partial^4 u(x; t)}{\partial x^4} = 0$$

The chord-wise and span-wise mass and stiffness distributions are:

$$m_c(y) = 2\rho t L; \quad I_c(y) = \frac{Lt^2(\xi(y))^2}{2}$$

$$m_s(x) = 2\rho b(x); \quad I_s(x) = \frac{2b(x)th_m^2(x)}{2}$$

Assuming small-amplitude vibrations, the dynamic deflections can be expressed as linear superposition of the modal displacements, as follows:

$$v(y, t) = \sum_{j=1}^{\infty} \varphi_j^c(y) f_j(t); \quad u(x, t) = \sum_{j=1}^{\infty} \varphi_j^s(x) f_j(t)$$

Here, φ_j^c is the j^{th} uniform chord-wise modeshape and φ_j^s is the j^{th} uniform span-wise modeshape. $f_j(t)$ is the j^{th} principal coordinate. In the conservative system, the maximum potential energy is equal to the maximum kinetic energy. As the basic assumption of the energy-based **Rayleigh-Ritz method**, the non-uniform beam modeshapes φ_j^s and φ_j^c in either direction are assumed to be a weighted summation of corresponding uniform beam modeshapes, i.e.

$$\phi_j^s(x) = \sum_{k=1}^{\infty} a_{jk} \varphi_k^s(x); \quad \phi_j^c(y) = \sum_{k=1}^{\infty} a_{jk} \varphi_k^c(y) \quad (3.1)$$

The unknown coefficients a_{jk} are estimated by minimizing the natural frequency ω of the beam. The square of frequency can be expressed as a ratio of the maximum strain potential energy and maximum kinetic energy.

$$\omega_{span}^2 = \frac{\int_0^l EI(x) \left(\frac{d^2 \phi^s(x)}{dx^2} \right)^2 dx}{\int_0^l m(x) [\phi^s(x)]^2 dx}; \quad \omega_{chord}^2 = \frac{\int_0^l EI(y) \left(\frac{d^2 \phi^c(y)}{dy^2} \right)^2 dy}{\int_0^l m(y) [\phi^c(y)]^2 dy} \quad (3.2)$$

For the minimum natural frequency, after substituting value of $\phi_j^s(x)$ and $\phi_j^c(y)$ from Eq. 3.1; the derivatives of Eq. 3.2, with respect to the weighted coefficients, are zero. Thus, the frequency ω , of non-uniform beam vibration in each direction, is the solution of set of linear equations Eq. 3.3:

$$|(K_{i,j}^s - \omega_{span}^2 M_{i,j}^s)| = 0; \quad |(K_{i,j}^c - \omega_{chord}^2 M_{i,j}^c)| = 0 \quad (3.3)$$

where the stiffness and the mass matrices are as follows :

$$K_{i,j}^s = \int_0^l EI(x) \frac{d^2\phi_i^s(x)}{dx^2} \frac{d^2\phi_j^s(x)}{dx^2} dx; \quad M_{i,j}^s = \int_0^l m(x)\phi_i^s(x)\phi_j^s(x) dx \quad (3.4)$$

$$K_{i,j}^c = \int_0^l EI(y) \frac{d^2\phi_i^c(y)}{dy^2} \frac{d^2\phi_j^c(y)}{dy^2} dy; \quad M_{i,j}^c = \int_0^l m(y)\phi_i^c(y)\phi_j^c(y) dy \quad (3.5)$$

Here, a_{jk} is the coefficient of the weighted summation of j^{th} non-uniform modeshape, for the k^{th} element of Eigen vector, obtained by substituting the i^{th} solution of ω in the matrix $[K_{i,j} - \omega^2 M_{i,j}]$. Substituting them in Eq. 3.1 generates the non-uniform beam modeshapes in each direction.

3.1.2 Plate Vibraion

Once the beam-wise modeshapes along the span and the chord are ready; one can proceed to the plate vibration analysis. The free dry vibration of the rudder is analyzed by the energy-based Galerkin's method. The average thickness-to-span ratio is less than 0.025. However, in chord-wise direction, this ratio is greater than 0.025 (**Appendix B**). But, since the aerofoil is hollow, the plate is considered as a 'thin' Kirchhoff's plate. The governing differential equation for free vibration of an orthotropic Kirchhoff's plate, is given as:

$$m(x,y) \frac{\partial^2 Z(x,y;t)}{\partial t^2} + \left[D_x \frac{\partial^4 Z(x,y;t)}{\partial x^4} + 2D_{xy} \frac{\partial^4 Z(x,y;t)}{\partial x^2 y^2} + D_y \frac{\partial^4 Z(x,y;t)}{\partial y^4} \right] = 0 \quad (3.6)$$

with flexural rigidity as $D_x = D_y = \frac{6Eh_m^2 t}{12(1-\mu^2)}$; $D_{xy} = \frac{\mu 6Eh_m^2 t}{12(1-\mu^2)}$. Here, h_m is the mean thickness of the mean chord, i.e. $h_m = \frac{c}{4}\pi e$ (refer **Appendix B**).

$m(x,y)$ is the mass per unit area of the plate (kg/m^3) and $Z(x,y;t)$ is the total transverse out-of-plane flexural displacement of the plate as a function of space and time. In a more generalized form, the GDE Eq. 3.6 can also be written as :

$$m(x,y) \frac{\partial^2 Z(x,y;t)}{\partial t^2} + \nabla^4 [D(x,y)Z(x,y;t)] = 0 \quad (3.7)$$

Here, $m(x,y)$ is the mass per unit area (kg/m^2), and $D(x,y)$ is the flexural rigidity of the plate ($N\cdot m$) which can be expressed as:

$$D(x,y) = \frac{6Eh^2 t}{12(1-\mu^2)} f^2(x)g^2(y) = D_0 p(x)q(y) \quad (3.8)$$

where $D_0 = \frac{Eh^2 t}{2(1-\mu^2)}$. As the beams are non-uniform, their modeshapes are *not* orthogonal in nature, and the modulus of flexural rigidity will vary in the two perpendicular

directions. Let ‘ h ’ be the local thickness of plate in both the directions, such that

$$h(x, y) = h_0 f(x) g(y)$$

where h_0 is thickness at the origin (located at the tip chord), and ‘ t ’ is sheet thickness. Here

$$f(x) = \left(1 + \frac{x}{5L}\right); \quad g(y) = \left(\frac{y}{b}\right) \sqrt{\left(1 - \left(\frac{y-b}{b}\right)^2\right)}; \quad (3.9)$$

$$p(x) = f^2(x); \quad q(y) = g^2(y) \quad (3.10)$$

The total transverse out-of-plane flexural displacement of the plate, ignoring shear deformation and rotary inertia $Z(x, y; t)$ in Eq. 3.6 and Eq. 3.7 can be expressed as a superposition of the modal displacements as:

$$Z(x, y; t) = \sum_{k=1}^{\infty} \Phi_k(x, y) F_k^p(t) \quad (3.11)$$

In the first GDE Eq. 3.6, the plate modeshape $\Phi_k(x, y)$ is expressed as a weighted superposition of the product of the *non-uniform beam* modeshapes:

$$\Phi_k(x, y) = \sum_{i=1}^{\infty} \sum_{j=1}^{\infty} A_{ij}^k \phi_i^s(x) \phi_j^c(y) \quad (3.12)$$

For the second GDE Eq. 3.7, the plate modeshape $\Phi_k(x, y)$ is expressed as a weighted superposition of the product of the *uniform beam* modeshapes:

$$\Phi_k(x, y) = \sum_{i=1}^{\infty} \sum_{j=1}^{\infty} A_{ij}^k \varphi_i^s(x) \varphi_j^c(y) \quad (3.13)$$

Expanding biharmonic operator and multiplying the first GDE (3.6) by the Galerkin’s premultiplier $H_{rs} = \varphi_r^s(x) \varphi_s^c(y)$ and integrating it over the plate surface, and substituting the flexural rigidity components D_x, D_y, D_{xy} , the spatial term can be written as

$$\sum_{i=1}^{\infty} \sum_{j=1}^{\infty} A_{ij}^k \left[D_x \frac{\partial^4 \phi_i^s(x)}{\partial x^4} \phi_j^c(y) + 2D_{xy} \frac{\partial^2 \phi_i^s(x)}{\partial x^2} \frac{\partial^2 \phi_j^c(y)}{\partial y^2} + D_y \phi_i^s(x) \frac{\partial^4 \phi_j^c(y)}{\partial y^4} \right] \quad (3.14)$$

Expanding biharmonic operator, multiplying the second GDE Eq. 3.7 by the Galerkin’s premultiplier $H_{rs} = \phi_r^s(x) \phi_s^c(y)$ and integrating it over the plate surface, and substituting value of $D(x, y)$ from (3.8) in (3.7), the spatial term can be written as

$$\nabla^4 [D(x, y) \Phi(x, y)] = [p_{xxxx} q \Phi + 4p_{xxx} q \Phi_x + 6p_{xx} q \Phi_{xx} + 4p_x q \Phi_{xxx}]$$

$$+ pq\Phi_{xxxx}] + [2p_{xx}q_{yy}\Phi + 4p_xq_{yy}\Phi_x + 2_{yy}\Phi_{xx} + 4p_{xx}q_y\Phi_y + 16(1 - \mu)p_xq_y\Phi_{xy} + \\ 4pq_y\Phi_{xxy} + 2_{xx}q\Phi_{yy} + 4p_xq\Phi_{xyy} + 2pq\Phi_{xxyy}] + [pq_{yyyy}\Phi + 4pq_{yyy}\Phi_y + \\ 6pq_{yy}\Phi_{yy} + 4pq_y\Phi_{yyy} + pq\Phi_{yyyy}]$$

where, the subscript to any function represents its partial derivative with respect to that subscript. The derivatives in system (3.14) can be written as $\frac{d^{2a}\phi_i^s(x)}{dx^{2a}} = \beta_x^{2a}\phi_i^s(x)$ $\frac{d^{2a}\phi_i^c(y)}{dy^{2a}} = \beta_y^{2a}\phi_i^c(y)$; for $a = 1, 2, \dots$. Here, β_x and β_y are the frequency parameters in the span-wise and chord-wise directions respectively.

In either way, the GDE is then converted into an Eigen value problem by applying the ‘separation of variables’ method in the temporal and spatial components. Performing the Eigen value analysis, $m\omega^2$ represents the Eigen values, and the weighted summation coefficient A_{ij} matrix represents the Eigen vector matrix, which defines the shape of rudder modes. Each column in the A_{ij} matrix represents an Eigen vector. The Eigen value problem can be written as:

$$[K - m\omega^2 I]\{A_{ij}\} = \{0\} \quad (3.15)$$

[K] is generated by pre-multiplying with the Galerkin’s pre-multiplier and integrating over the surface area and can be expressed as:

$$[K] = \int_0^L \int_0^C \left[(\phi_i^s \phi_j^c) \right]^{-1} \phi_r^s(x) \phi_s^c(y) \times \\ \left[D_x \frac{\partial^4 \phi_i^s(x)}{\partial x^4} \phi_j^c(y) + 2D_{xy} \frac{\partial^2 \phi_i^s(x)}{\partial x^2} \frac{\partial^2 \phi_j^c(y)}{\partial y^2} + D_y \phi_i^s(x) \frac{\partial^4 \phi_j^c(y)}{\partial y^4} \right] dx dy \quad (3.16)$$

In the more generalized Galerkin’s method, [K] matrix derived from GDE (3.7) can be expressed as:

$$[K] = \left[\sum_{i=1}^5 F_i + \sum_{i=1}^9 M_i + \sum_{i=1}^5 L_i \right] \quad (3.17)$$

In Eq. 3.19, each of the $5+9+5 = 19$ terms, are shown in **Appendix 3**. In the present study, the first three flexural modes, in each direction, are considered; along with sway and yaw *rigid body* mode shapes. The natural frequencies are obtained by solving $|K - m\omega^2 I| = 0$ and the Eigen vectors are obtained by substituting each Eigen value in Eq. 3.15. Each Eigen vector has one dominant term, showing the prominence of the contribution of each of the chord-wise and span-wise beam modeshapes. Suppose A_{ij}^k is large: it shows that the i^{th} span-wise beam mode and the j^{th} chord-wise beam mode together have a large contribution in the k^{th} plate modeshape. The Eigen vectors from Eq. 3.16 are substituted back into Eq. 3.12, and multiplied by the product of the non-uniform beam modeshapes, in order to generate the final plate modeshape. The

Eigen vectors from Eq. 3.17 are substituted back into Eq. 3.13, and multiplied by the product of the uniform beam modeshapes, to generate the final plate modeshape.

3.2 Wet Vibration : 2D

In the fully loaded condition of the ship, the rudder is completely submerged, while in the lightship condition, it is partially dry (15%-20% of the span length). The natural frequencies of vibration decrease considerably due to the fluid inertia. The added mass in span-wise flexural vibration, and the added mass moment of inertia in torsional vibration; are both calculated theoretically and by the 2D constant-strength source distribution technique. The solid inertia of the plate is augmented by the fluid inertia, calculated by the 3D constant strength source distribution technique. The governing differential equation for the free, wet vibration, of the chord-wise Euler-Bernoulli's beam is:

$$m_s(x) \frac{\partial^2 u(x, t)}{\partial t^2} + EI_s(x) \frac{\partial^4 u(x, t)}{\partial y^4} = - \oint \rho \frac{\partial \Psi^{2D}}{\partial t} \vec{k} \cdot \vec{n} |dl| \quad (3.18)$$

The RHS of Eq. 3.18 is the fluid radiation pressure for sway motion of the rudder. Here, Ψ^{2D} is the pulsating radiation potential. The linear hydrodynamic pressure, $\rho \frac{\partial \Psi^{2D}(y, z; t)}{\partial t}$, at each x -location, acting normally (direction \vec{n}) on the surface, is integrated over the perimeter $|dl|$ of the aerofoil section, in the direction of the sway motion k . For the 2D radiation pressure of the chord-wise section, the NACA profile of aerofoil is approximated by the Kutta-Joukowski transformation, in order to ease the calculation of the 2-D sectional added mass. The pressure distribution over the circle can be directly mapped onto an aerofoil by the Joukowski transformation. The transformation parameter 'e', i.e. the fineness ratio, is chosen after considering three error parameters:

- (i) Aerofoil cross-sectional area
- (ii) Aerofoil perimeter
- (iii) The position of the maximum thickness along the chord.

Here, a circle in the plane (x, y) is transformed into a symmetric aerofoil in the plane (ξ, ς) .

$$\xi(\theta) = b \cos \theta; \quad \varsigma(\theta) = b e(1 + \cos \theta) \sin \theta \quad (3.19)$$

where θ is the local parameter ($\in (0, 2\pi)$), $2b$ is the chord-length. The 2D sectional sway added mass and yaw added mass moment can be calculated theoretically, by assuming a radiation problem around an oscillating dipole in an otherwise calm fluid. The fluid is assumed to be inviscid and incompressible, and the flow irrotational. Potential flow theory is used to determine the radiation pressure distribution over a circle, and transformed to that over an aerofoil. Using the no-penetration body boundary condition (BBC), the velocity potential in sway and yaw can be calculated. This gives the radiation pressure, whose surface integral in the sway direction gives the radiation force

in sway; and the moment of the radiation force in yaw gives the added mass moment in yaw. The details are shown in the following sub-sections.

3.2.1 Theoretical technique (Potential flow theory)

For analyzing the free or forced vibration of the rudder under water the added mass must be calculated; as it has a considerable influence on the natural frequencies. Added mass is calculated for heave and roll motion. The geometry is changed from a circle to an airfoil, by the *Joukowski transformation*, such that the pressure distribution over the circle perimeter is directly mapped onto an aerofoil by *conformal mapping*, which leads to the added mass calculation.

3.2.1.1 Sway

The hydrodynamic influence of a circular cylinder in an ideal fluid can be mathematically represented as a doublet. Velocity potential for a doublet is given by

$$\psi(r, \theta) = \frac{\mu \cos(\theta)}{2\pi r} \quad (3.20)$$

where

μ : Dipole moment

r : Distance of the field point from the centre of the doublet

The sway velocity is assumed as $\dot{\eta}(t)$. Therefore, at $r = a$, the radial velocity of fluid V_r must be equal to the radial component of sway velocity.

$$V_r = \frac{\partial \psi(r, \theta)}{\partial r} \Big|_{r=a} = -\frac{\mu \cos(\theta)}{2\pi a^2} = \dot{\eta} \cos(\theta) \quad (3.21)$$

where

μ : $-2\pi a^2 \dot{\eta}(t)$

Substituting value of the dipole moment μ in Eq.3.20

$$\psi(a, \theta; t) = -a \dot{\eta} \cos(\theta) \quad (3.22)$$

The linear hydrodynamic pressure can be expressed as:-

$$p = -\rho \frac{\partial \psi}{\partial t} = \rho a \ddot{\eta} \cos(\theta) \quad (3.23)$$

The added mass can be obtained by transforming pressure distribution over circle to aerofoil by *Joukowski transformation*, multiplying it by corresponding normal and dividing the radiation force by the body's acceleration $\ddot{\eta}$. The details of normal are

shown in **Appendix B.6**

$$\text{Added mass in sway} = \oint_l \frac{p}{\dot{\eta}} \vec{n} \cdot \hat{k} |\vec{dl}| \quad (3.24)$$

Here,

- \vec{n} : Normal to aerofoil perimeter ;
 \hat{k} : Unit vector in the vertical direction .

3.2.1.2 Yaw

Here, the boundary condition is the no-slip condition, i.e. tangential velocity at radius a must be equal to the yaw velocity

$$V_\theta = \frac{1}{r} \frac{\partial \psi(r, \theta)}{\partial \theta} = -\frac{\mu \sin \theta}{2\pi a^2} = \omega a \sin \theta \quad (3.25)$$

where

- ω : Roll angular velocity
 μ : $-2\pi a^3 \omega$

Substituting value of the dipole moment μ in Eq.3.20

$$\psi(a, \theta; t) = -\omega a^2 \cos \theta \quad (3.26)$$

Therefore, the linear hydrodynamic pressure can be written as

$$p = -\rho \frac{\partial \psi}{\partial t} = \rho a^2 \dot{\omega} \cos \theta \quad (3.27)$$

The added mass moment of inertia can be obtained by dividing the radiation torque with the body's angular acceleration $\dot{\omega}$;

$$\text{i.e. Added mass moment of inertia} = \oint_l \frac{p}{\dot{\omega}} \vec{r} \times \hat{n} |\vec{dl}| \quad (3.28)$$

Here,

- \vec{n} : Normal to aerofoil perimeter ;
 \vec{r} : Arm length from centre of gravity to the element $|\vec{dl}|$;

3.2.2 Numerical technique

The total added mass and added mass moment of inertia is also been calculated numerically. 2D constant sources of unknown strength are distributed over the perimeter of

aerofoil section, and the 2D boundary value problem is solved for the velocity potential of each source.

The 2D constant strength Green's function is assumed as

$$G(P, Q) = \frac{1}{2\pi} \ln(\vec{r} - \vec{r}_0)$$

Here, $\vec{r}(y, z)$ is position vector of field point P and $\vec{r}_0(\eta, \varsigma)$ is position vector of source point Q. Therefore, the distance between P and Q is

$$|\vec{r} - \vec{r}_0| = \sqrt{(y - \eta)^2 + (z - \varsigma)^2} \quad (3.29)$$

The radiation potential $\Psi^{2D}(y, z; t)$ on the surface of the body, can also be solved by 2D constant-strength source distribution technique as :

$$\frac{1}{2} \Psi^{2D}(y, z; t) = \int_{\Delta S} \left[\Psi^{2D}(\eta, \varsigma; t) \frac{\partial G_{PQ}(y, z; \eta, \varsigma)}{\partial n_Q} - G_{PQ}(y, z; \eta, \varsigma) \frac{\partial \Psi^{2D}(\eta, \varsigma; t)}{\partial n_Q} \right] ds \quad (3.30)$$

ds is the infinitesimal perimeter, and ΔS is the panel length. The spatial derivatives in the above can be expressed as

$$\frac{\partial G_{PQ}(y, z; \eta, \varsigma)}{\partial n_Q} = \frac{\partial G_{PQ}(y, z; \eta, \varsigma)}{\partial \eta} \vec{n}_y + \frac{\partial G_{PQ}(y, z; \eta, \varsigma)}{\partial \varsigma} \vec{n}_z \quad (3.31)$$

The BBCs of 'no penetration' (normal velocity is continuous) are :

$$\frac{\partial \Psi^{2D}(Q)}{\partial n_Q} = \vec{n}_3 \quad \text{for sway;} \quad \frac{\partial \Psi^{2D}(Q)}{\partial \vec{n}_Q} = (\vec{r} \times \vec{n})_1 \quad \text{for yaw} \quad (3.32)$$

By considering the influence of each source point on each field point, an $(n \times n)$ system of equations can be obtained, where n is the total number of 2D panels. By solving for each velocity potential, the radiation pressure distribution and the added mass can be calculated. The correction factor J is included for considering the effects of the ends of beam while transforming the 2D added mass into 3D, as strip theory is a good approximation only for bodies of very high aspect ratio (longish bodies). Here, J is the ratio of the 3D fluid kinetic energy to the 2D Strip theory based fluid kinetic energy, i.e. $J < 1$.

3.2.3 3D Green's function technique

The effect of modeshape on the added mass and added mass moment of inertia calculations is significant, as these values decrease as the mode number increases. But the 2D added mass calculation does not consider the effect of mode number. The governing differential equation for free wet vibration of a Kirchhoff's plate, with water on both

sides, is:

$$m(x, y) \frac{\partial^2 Z(x, y; t)}{\partial t^2} + D \nabla^4 Z(x, y; t) = \oint -\rho i \omega \Psi_k^{3D}(x, y, z; t) \vec{k} \cdot \vec{n} |dl| \quad (3.33)$$

Ψ_k^{3D} in Eq. 3.33 is assumed as the linear superposition of infinite modal velocity potentials, each satisfying the 3D boundary value problem. We express

$$\Psi_k^{3D}(x, y, z; t) = \Psi_k^*(x, y, z) \frac{dq_k(t)}{dt} \quad (3.34)$$

where $\Psi_k^*(x, y, z)$ is the velocity potential per unit modal velocity of the structure (auxiliary velocity potential). The details are shown in Datta and Troesch (2012)[13]. The 3D Green's function is assumed as potential of a 3D source (Appendix D.2) as $G(P, Q) = \frac{1}{4\pi|\vec{r}-\vec{r}_0|}$. The rudder is in touch with water on both the sides, but as the frequency of vibration is very high, the “mirror effect” takes place on both sides. The double body problem is set up at the high frequency range of oscillations. The *body boundary condition* for 3D boundary value problem of rudder for k^{th} mode can be expressed as:

$$\frac{\partial \Psi_k^{3D}}{\partial z} = \Phi_k q_k \quad \text{at } z = 0 \quad (3.35)$$

The total added mass is twice of the added mass on each side. After substituting $\Psi_k^{3D}(x, y, z; t)$ from (3.34) in GDE (3.33), and writing $Z(x, y; t) = \sum_{k=1}^{\infty} \Phi_k(x, y) q_k(t)$, the GDE becomes

$$\sum_{k=1}^{\infty} m(x, y) \Phi_k(x, y) \frac{d^2 q_k(t)}{dt^2} + \nabla^4 D(x, y) \sum_{k=1}^{\infty} \Phi_k(x, y) q_k(t) = -\rho \sum_{k=1}^{\infty} \Psi_k^*(x, y, 0) \frac{d^2 q_k(t)}{dt^2} \quad (3.36)$$

Pre-multiplying this equation with r^{th} plate modeshape $\Phi_r(x, y)$, and integrating over the surface area $L \times B$, gives the generalized added mass, which is in-phase with the solid inertia, and contributes in reducing the natural frequencies of vibration.

3.2.4 Numerical software : ANSYS

The dry frequencies of the spade rudder also calculated by using ANSYS 15, where the pivot is fixed with rudder with a ‘fixed joint’ and also clamped to the ground. The other three ends are considered to be free. Here, the rudder is modelled as a sheet of 3 mm thickness plate, using the

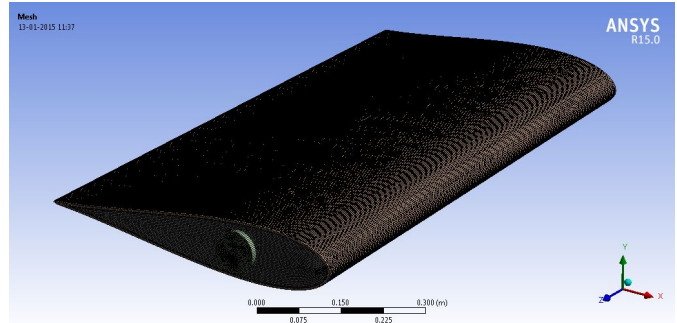


FIGURE 3.1: Rudder model mesh in ANSYS

ANSYS design module. The sketch of aerofoil section is drawn using Bezier curves. The mesh is generated with the help of 252981 nodes and 253116 elements. The material properties used for the rudder are for mild steel i.e. density is 7850 kg/m^3 and Poissons ratio $\mu = 0.3$. The Young's modulus is taken to be 200 GPa. The values are selected to maintain the analysis as realistic as possible. The 'smeared' thickness of the plate material is taken to be 3 mm. The minimum mesh size used is 0.3 mm. Three-dimensional tetrahedral mesh was used for the analysis. The size of mesh is very fine in the higher curvature regions, whereas it is coarse in the smooth regions. The size of mesh was selected taking care of the thinnest component of the rudder i.e. the metal sheet of the rudder. The minimum mesh size is less than 50% of the thinnest plate thickness.

3.3 Forced Vibration

A marine rudder mostly operates fully submerged under water, except for the lightweight condition. Its aerofoil section generates lift and drag at oblique angles of attack, which leads to hydrodynamic forces on the rudder. These forces and moments are calculated by following the computational details given by Harrington [14].

3.3.1 Spade Rudder torque calculations by Harrington method

The basic ship data of the Korean Container Ship (KCS), to which this rudder belongs, is given in **Table 3.1**. The propeller thrust is calculated from the total resistance of the ship, which is obtained by the Holtrop and Mennen[15] emperical formulae.

TABLE 3.1: Basic KCS ship data

Number of rudders	1	
Length on Waterline (L)	232.5	m
Draught (mean) (T)	10.8	m
Max. Design speed ahead (V)	24	knots
Froude number	0.259	
Thrust deduction fraction (t)	0.165	
Wake fraction (w)	0.275	
Propeller diameter (D)	7.9	m
Speed of advance (V_A)	8.944	ms^{-1}
Propeller thrust (T)	2288247	N
Dynamic pressure (P)	87.707	kNm^{-2}

The lift coefficient C_{L_1} , the drag coefficient C_{D_1} and the centre of pressure CP_{C_1} for uncorrected taper ratios obtained from figures given in Whicker and Fehlner (1958) and DTMP report. This data is further corrected as C_{L_2} , C_{D_2} and CP_{C_2} respectively by

using empirical formulae by taking account of structural non-linearity due to the aerofoil shape, which finally leads to normal force and hydrodynamic torque calculations given in **Table 3.2**.

TABLE 3.2: Normal force and hydrodynamic torque on the rudder, at various rudder angles

δ (rudder angle)	0^0	7^0	14^0	21^0	28^0	35^0
M (local variable)	1	0.943	0.886	0.829	0.771	0.714
α (angle of attack)	0^0	6.6^0	12.4^0	17.4^0	21.6^0	25^0
a_1 (aspect ratio)	0.909	0.951	0.991	1.028	1.062	1.09
C_{L_1}	0	0.1813	0.3052	0.4752	0.6396	0.7900
C_{D_1}	0	0.025	0.064	0.12	0.169	0.244
$CP_{\bar{C}_1}$	0	0.145	0.1813	0.2163	0.235	0.262
ΔC_L	0	0.0087	0.0296	0.0563	0.0840	0.1096
C_{L_2}	0	0.1901	0.3349	0.5315	0.7236	0.8996
ΔC_D	0	0.0014	0.0080	0.0232	0.0453	0.0714
C_{D_2}	0	0.0264	0.0724	0.1432	0.2147	0.3157
C_{N_1}	0	0.183	0.312	0.489	0.657	0.819
C_{N_2}	0	0.192	0.343	0.55	0.752	0.949
$C_{M\bar{C}4_2}$	0	0.015	0.007	-0.012	-0.032	-0.065
$CP_{\bar{C}_2}$	0	1.226	0.71	0.475	0.376	0.332
Normal Hydrodynamic force (kN)	0	925.4	1652.8	2653.3	3626.8	4576.9
Hydrodynamic torque (kN-m)	0	107.8	192.7	309.3	422.8	533.6

The total hydrodynamic force is calculated from the lift and the drag coefficients by following Harrington's empirical formulae (Eq. 3.37), but the variation of the lift coefficient along the span is considered to be *parabolic*, with maximum at mean chord of rudder [16] as shown in Eq. 3.37, which yields the variation of normal hydrodynamic force over rudder span, for different rudder angles, as shown in **Fig.3.2**.

$$C_{Ll}(x) = C_L \frac{4}{\pi} \sqrt{1 - \left(\frac{x - L/2}{L/2} \right)^2} \quad (3.37)$$

Thus the total pulsating hydrodynamic force may be expressed as:

$$|F_{ext}(t)|_{total} = p\bar{c}X_3C_N\cos(\omega_e t) \quad (3.38)$$

Here,

p : Hydrodynamic pressure (N/m^2) ; \bar{c} : Mean Chord (m);

X_3 : Rudder span (m) ; ω_e : Blade passing frequency (rad/sec);

C_N : $C_L \cos \alpha + C_D \sin \alpha$

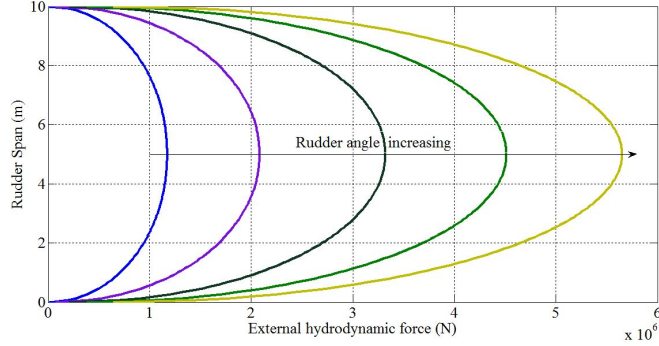


FIGURE 3.2: Hydrodynamic force variation over rudder span for various rudder angles

3.3.2 Mode Summation Method

The governing differential equation for the forced vibration of the Kirchhoff's plate, by taking three components of flexural rigidity, is given as:

$$m(x, y) \frac{\partial^2 Z(x, y; t)}{\partial t^2} + \left[D_x \frac{\partial^4 Z(x, y; t)}{\partial x^4} + 2D_{xy} \frac{\partial^4 Z(x, y; t)}{\partial x^2 y^2} + D_y \frac{\partial^4 Z(x, y; t)}{\partial y^4} \right] = F(x, y; t) \quad (3.39)$$

The total out-of-plane dynamic deflection of the plate is approximately a linear superposition of the modal deflections $Z_k(x, y, t)$, as given as:

$$Z(x, y; t) = \sum_{k=1}^{\infty} \Phi_k(x, y) q_k^p(t) \quad (3.40)$$

with the 3-D plate modeshape (shape function) $\Phi_r(x, y)$ is defined as a series summation as follows

$$\Phi_k(x, y) = \sum_{j=1}^{modex} \sum_{l=1}^{modey} A_{jl}^k \phi_j^s(x) \phi_l^c(y) = \sum_{j=1}^{modex} \sum_{l=1}^{modey} A_{jl}^k G_{jl}(x, y) \quad (3.41)$$

i.e. $G_{jl}(x, y) = \phi_j^s(x) \phi_l^c(y)$, $modex$ is the number of modes considered in the x -direction, $modey$ is the number of modes considered in the y -direction, and $\phi_j^s(x)$ and $\phi_l^c(y)$ are the respective 2-D non-uniform beam modeshapes. A_{jl}^k is the amplitude of each $G_{jl}(x, y)$ for the k^{th} natural frequency of vibration. Substituting for the plate modeshape in the GDE :

$$m \sum_{k=1}^{\infty} \Phi_k(x, y) \ddot{q}_k(t) + \sum_{k=1}^{\infty} \left[D_x \frac{\partial^4 \Phi_k(x, y)}{\partial x^4} + 2D_{xy} \frac{\partial^4 \Phi_k(x, y)}{\partial x^2 y^2} + D_y \frac{\partial^4 \Phi_k(x, y)}{\partial y^4} \right] q_k(t) = F(x, y; t) \quad (3.42)$$

Pre-multiplying by the plate modeshape and integrating over the plate surface area :

$$\int_0^L \int_0^C \Phi_r(x, y) m \sum_{k=1}^{\infty} \Phi_k(x, y) \ddot{q}_k(t) dx dy + \int_0^L \int_0^C \Phi_r(x, y) \sum_{k=1}^{\infty} \left[\frac{D_x \partial^4 \Phi_k(x, y)}{\partial x^4} + \right.$$

$$2D_{xy} \frac{\partial^4 \Phi_k(x, y)}{\partial x^2 y^2} + D_y \frac{\partial^4 \Phi_k(x, y)}{\partial y^4} q_k(t) dx dy = \int_0^L \int_0^C \Phi_r(x, y) F(x, y; t) dx dy \quad (3.43)$$

In the matrix form, the system of governing differential equation is:

$$\sum_{k=1}^{modey} M_{rk}^p \ddot{q}_k(t) + \sum_{k=1}^{modey} K_{rk}^p q_k(t) = GF_r^p(t) \quad (3.44)$$

where the generalized mass, stiffness and forcing are the following respectively :

$$M_{rk}^p = m \int_0^L \int_0^C \Phi_r(x, y) \Phi_k(x, y) dx dy \\ = m \int_0^L \int_0^C \left[\sum_{r=1}^{modey} \sum_{s=1}^{modey} A_{rs}^p \phi_r^s(x) \phi_s^c(y) \right] \left[\sum_{j=1}^{modey} \sum_{l=1}^{modey} A_{jl}^k \phi_j^s(x) \phi_l^c(y) \right] dx dy \quad (3.45)$$

$$K_{rk}^p = \int_0^L \int_0^C \Phi_r(x, y) \left[\frac{D_x \partial^4 \Phi_k(x, y)}{\partial x^4} + 2D_{xy} \frac{\partial^4 \Phi_k(x, y)}{\partial x^2 y^2} + D_y \frac{\partial^4 \Phi_k(x, y)}{\partial y^4} \right] dx dy \\ = D_x \int_0^L \int_0^C \left[\sum_{r=1}^{modey} \sum_{s=1}^{modey} A_{rs}^p \phi_r^s(x) \phi_s^c(y) \right] \left[\sum_{j=1}^{modey} \sum_{l=1}^{modey} A_{jl}^k \frac{\partial^4 \phi_j^s(x)}{\partial x^4} \phi_l^c(y) \right] dx dy \\ + 2D_{xy} \int_0^L \int_0^C \left[\sum_{r=1}^{modey} \sum_{s=1}^{modey} A_{rs}^p \phi_r^s(x) \phi_s^c(y) \right] \left[\sum_{j=1}^{modey} \sum_{l=1}^{modey} A_{jl}^k \frac{\partial^2 \phi_j^s(x)}{\partial x^2} \frac{\partial^2 \phi_l^c(y)}{\partial y^2} \right] dx dy \\ + D_y \int_0^L \int_0^C \left[\sum_{r=1}^{modey} \sum_{s=1}^{modey} A_{rs}^p \phi_r^s(x) \phi_s^c(y) \right] \left[\sum_{j=1}^{modey} \sum_{l=1}^{modey} A_{jl}^k \phi_j^s(x) \frac{\partial^4 \phi_l^c(y)}{\partial y^4} \right] dx dy \quad (3.46)$$

$$GF_r^p = \int_0^L \int_0^C \Phi_r(x, y) F(x, y; t) dx dy = \int_0^L \int_0^C \sum_{r=1}^{modey} \sum_{s=1}^{modey} A_{rs}^p \phi_r^s(x) \phi_s^c(y) F(x, y; t) dx dy \quad (3.47)$$

3.3.3 Forced wet plate vibration - Dynamic analysis

The governing differential equation for the forced wet vibration of the Kirchhoff's plate, by taking three components of flexural rigidity, is given as:

$$\left[m(x, y) + \oint -\rho i \omega \Psi_j^{3D}(x, y, z; t) \vec{k} \cdot \vec{n} |d\vec{l}| \right] \frac{\partial^2 Z(x, y; t)}{\partial t^2} + \\ \left[D_x \frac{\partial^4 Z(x, y; t)}{\partial x^4} + 2D_{xy} \frac{\partial^4 Z(x, y; t)}{\partial x^2 y^2} + D_y \frac{\partial^4 Z(x, y; t)}{\partial y^4} \right] = F(x, y; t) \quad (3.48)$$

The total out-of-plane dynamic deflection of the plate is approximately a linear superposition of the modal deflections $Z_k(x, y, t)$, as given as:

$$Z(x, y; t) = \sum_{k=1}^{\infty} \phi_k^p(x, y) q_k^p(t) \quad (3.49)$$

Substituting the deflection in GDE, pre-multiplying it by the plate modeshape and integrating over the plate surface area, system of equations form as

$$\sum_{k=1}^{mode_x \times mode_y} [M_{rk}^p + A_{rk}^p] \ddot{q}(t) + \sum_{k=1}^{mode_x \times mode_y} K_{rk}^p q(t) = GF_r^p(t) \quad (3.50)$$

Here, M_{rk}^p : Mass matrix ; A_{rk}^p : Added mass matrix

K_{rk}^p : Stiffness matrix ; GF_r^p : Generalized force,

such that, the principle co-ordinates can be expressed as

$$q_k(t) = [[K] - \omega^2 [[M] + [A]]]^{-1} GF_k(t) \quad (3.51)$$

The principal coordinates are multiplied with the respective plate modeshapes in order to generate the total deflection $Z(x, y; t)$, and the associated dynamic stresses can be expressed as:

$$\begin{aligned} \sigma_x(x, y; t) &= \sum_{k=1}^{\infty} \frac{Eh_m}{(1-\mu^2)} \left[\frac{\partial^2 \Phi_k(x, y)}{\partial x^2} + \mu \frac{\partial^2 \Phi_k(x, y)}{\partial y^2} \right] F_k^p(t) \\ \sigma_y(x, y; t) &= \sum_{k=1}^{\infty} \frac{Eh_m}{(1-\mu^2)} \left[\mu \frac{\partial^2 \Phi_k(x, y)}{\partial x^2} + \frac{\partial^2 \Phi_k(x, y)}{\partial y^2} \right] F_k^p(t) \\ \tau_{xy}(x, y; t) &= \sum_{k=1}^{\infty} \frac{Eh_m}{(1+\mu)} \left[\frac{\partial^2 \Phi_k(x, y)}{\partial x \partial y} \right] F_k^p(t) \end{aligned}$$

where σ_x is the normal stress along the span and σ_y is the normal stress along the chord, and τ_{xy} is the shear stress.

3.3.4 Forced plate vibration - Static analysis

The governing differential equation for the forced wet vibration of the Kirchhoff's plate, by taking three components of flexural rigidity, is given as:

$$\left[D_x \frac{\partial^4 Z(x, y)_{static}}{\partial x^4} + 2D_{xy} \frac{\partial^4 Z(x, y)_{static}}{\partial x^2 \partial y^2} + D_y \frac{\partial^4 Z(x, y)_{static}}{\partial y^4} \right] = |F(x, y)|_{rms} \quad (3.52)$$

Here, $|F(x, y)|_{rms} = \frac{p\bar{c}X_3C_N}{\sqrt{2}}$. The total out-of-plane static deflection of the plate is approximately a linear superposition of the modal deflections $Z_{static}(x, y)$, which can be

expressed as

$$Z(x, y)_{static} = \sum_{i=1}^{\infty} \sum_{j=1}^{\infty} A_{ij(static)}^p \phi_i^s(x) \phi_j^c(y) \quad (3.53)$$

The static weight matrix can be obtained by again following the modal superposition method as described for the dynamic deflection.

Chapter 4

Results

After detailing the analysis methodology of the dry and wet vibration of the rudder, this chapter deals with the results from the theoretical and numerical analysis. The chapter is divided into two parts, one for Rudder-I and the other for Rudder-II. Each part is subdivided into the dry vibration and the wet vibration results. The dry vibration section gives the

- Non-uniform beam modeshape
- plate vibration frequencies and
- plate modeshapes.

The wet vibration section gives the wet natural frequencies of the submerged plate. The theoretical results of each rudder is followed by the numerical results from ANSYS and comparative studies.

4.1 Rudder model with non-classical pivot (Rudder-I)

The family of problems solved for this rudder model are shown in **Table 4.1**. The theoretical analysis is done for the free dry and wet vibration. The numerical verification has been done only for the dry vibration.

TABLE 4.1: Family of problems for rudder I

	Theoretical	Numerical	Experimental
Free dry vibration	✓	✓	
Free wet vibration	✓		
Forced wet vibration			

4.1.1 Dry Vibration

4.1.1.1 Non-uniform beam modeshapes

The first three chord-wise beam modeshapes are shown in **Fig. 4.1**. The solid lines are the non-uniform modeshapes, while the dashed lines are the corresponding uniform beam modeshapes. The results are shown for the root chord, which is 0.6 m long. The pivot occurs at 65% of the chord length from the trailing edge, i.e. at $0.65 \times 0.6 = 0.39$ m from the trailing edge. This point, being modelled as a combination of stiff translational and torsional springs, develops a node of the modeshape and thus has minimal deflection. The beam deflection and the slope are seen to remain continuous at the pivot, as formulated in Chapter 2. All the modeshapes are normalized, i.e. they vary between ± 1 . Comparing the elementary (uniform) modeshapes to the derived (non-uniform) modeshapes, it is observed that due to the fourth-order non-uniformity in the thickness profile chord-wise aerofoil section, the non-uniform chord-wise beam modeshapes deviate considerably from uniform chord-wise beam modeshapes. The LHS is the trailing edge, while the RHS is the leading edge. The natural frequencies get changed from uniform to non-uniform chord-wise modes. This change is due to the increased strain potential energy of the thicker mid region of the aerofoil, and the lower kinetic energy of the thinner free ends.

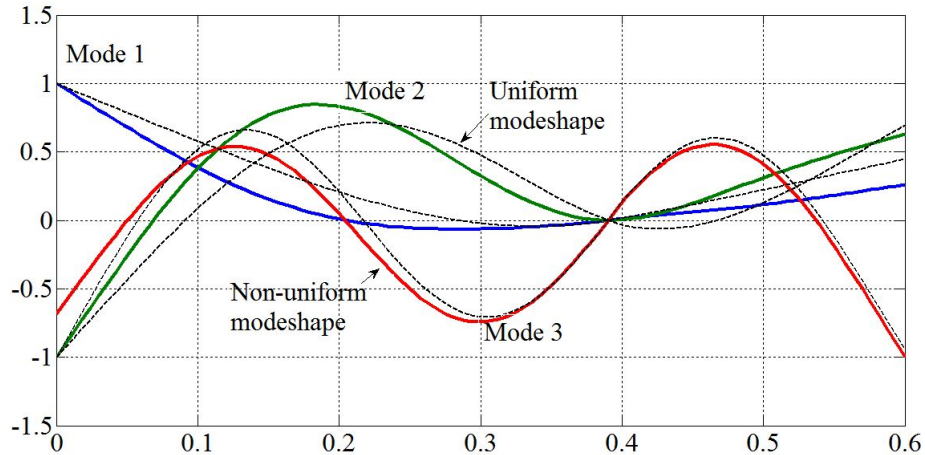


FIGURE 4.1: Chord-wise beam modeshapes

The position of the pivot also influences the natural frequencies of the non-uniform two-span beam. It is varied from 50 % to 75 % of the chord length from the trailing edge. **Fig. 4.2** shows the frequency variation for change in pivot position from the trailing edge. The maximum thickness of the rudder, according to (3.19), occurs at 75% of the chord length from the trailing edge. The first non-uniform mode is the stiffest with the pivot at 61 %, however, the second mode is the tenderest with the pivot at 67 %.

This trend reversal is reverted for the third mode where the pivot at 61 % again shows the stiffest behavior. For superior hydrodynamic performance and directional stability of the ship, the centre of fluid pressure for the flow past the aerofoil should always be *ahead* of the rudder stock. For superior structural integrity and ease of construction, the rudder stock should be as close to the maximum thickness location as possible.

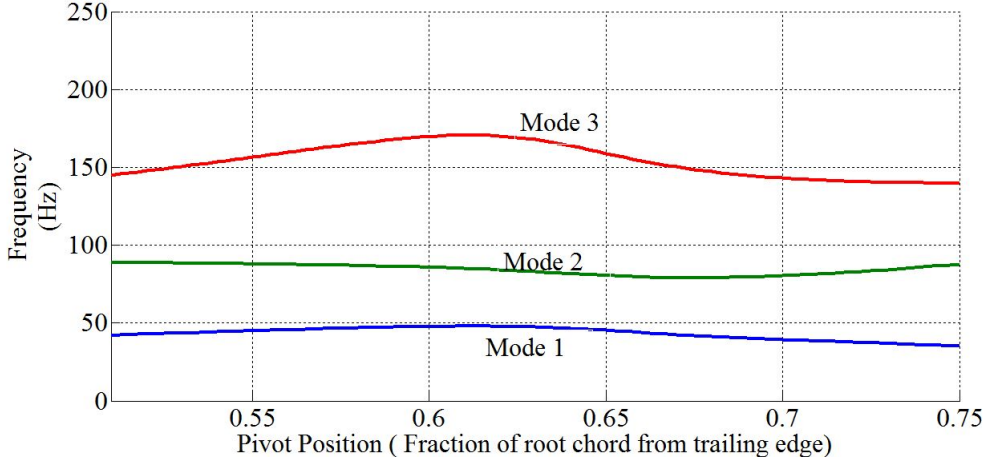


FIGURE 4.2: Frequency (Hz) comparison of non-uniform chord-wise modeshapes for different pivot positions

Table 4.2 shows the weight matrix a_{ij} for the non-uniform beam modeshape in the chord-wise direction, for two different pivot position, i.e. 65 % pivot and 70 % pivot. In both the 3×3 matrices, the diagonal dominates showing a strong self-coupling. This means that the j^{th} uniform beam modeshape has the largest contribution to the j^{th} non-uniform modeshape. The cross-coupling is highlighted by the presence of small, yet non-negligible, non-diagonal terms in the weight matrix. The signs of the non-diagonal elements are skew-symmetric, i.e. a_{ij} and a_{ji} are always opposite in sign. The weight matrix changes for changing pivot positions, still keeping the diagonal dominant.

TABLE 4.2: Weight matrix in chord-wise direction

$\frac{l}{C_R} = 0.65$			$\frac{l}{C_R} = 0.7$		
0.966	0.256	0.019	0.959	0.281	-0.017
-0.245	0.942	-0.226	-0.256	0.896	0.361
-0.076	0.213	0.973	0.117	-0.342	0.932

The first three non-uniform span-wise beam flexural modeshapes, with increasing taper ratio, are shown in **Fig 4.3**. The left side is the free end, while the right side is the fixed end. The fixity is modelled as a combination of stiff translational and rotational springs, which makes the end early clamped. Here, since the taper ratio $\lambda = 1.2$, is very mild, the uniform and non-uniform beam modeshapes almost overlap on each other. With the increase in taper ratio, the potential energy at the clamped end increases. However, the

kinetic energy, which is directly proportional to mass per unit length of beam, decreases. Since the natural frequency of vibration is the ratio of potential energy to kinetic energy ($\omega^2 = \frac{P.E}{K.E^*}$), the natural frequency of vibration increases.

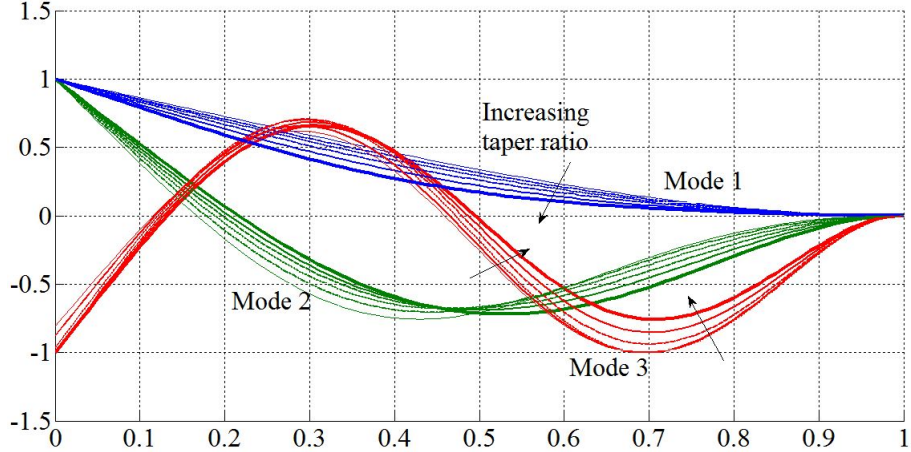


FIGURE 4.3: Span-wise beam modeshapes

The variation of frequency of span-wise beam modeshapes with increase in taper ratio is also shown in **Fig 4.4**. Increasing the taper ratio increases the curvature of the modeshape, leading to stiffer frequencies. At a taper ratio = 1, the Rayleigh-Ritz method returns the uniform beam frequencies and modeshapes. The taper ratio is defined as the ratio of the root chord to the tip chord. As the taper ratio increases, the beam becomes more and more like a wedge, i.e. taper ratio $\rightarrow \infty$. Correspondingly the natural frequencies increase and asymptote to those of a wedge.

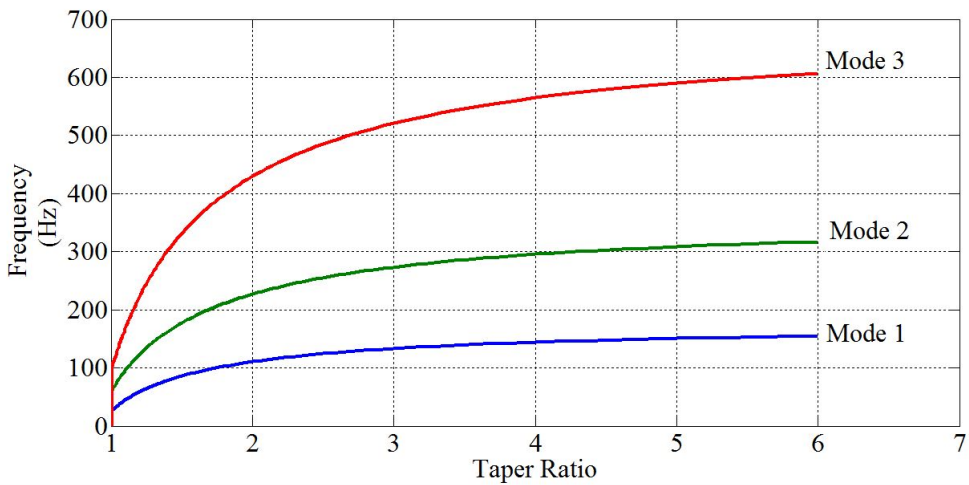


FIGURE 4.4: Frequency (Hz) comparison of non-uniform span-wise modeshapes for different taper ratios

If the taper ratio is one, i.e. the beam is uniform, the weight matrix of span-wise beam

modeshapes (**Table 4.3**) is exactly diagonal. The self-coupling is absolute and the cross-coupling is zero for a uniform beam. As the taper ratio increases, the contribution of non-diagonal terms begin to rise, because of the increasingly stronger cross coupling between the admissible functions (uniform beam modeshapes). Compared to the diagonal terms in **Table 4.2**, the diagonal terms are much larger, showing weaker cross-coupling for a milder non-uniformity. Once again, the signs of the non-diagonal elements are skew-symmetric.

TABLE 4.3: Weight matrix in span-wise direction

$\lambda = 0$	$\lambda = 1.2$			$\lambda = 3$		
1 0 0	0.999	0.023	-0.002	0.992	-0.123	-0.01
0 1 0	-0.02	0.997	0.068	0.121	0.965	0.231
0 0 1	0.003	-0.068	0.997	-0.021	-0.230	0.972

4.1.1.2 Plate natural frequencies and modeshapes

Fig. 4.5 and **Fig. 4.6** represent the variation of the thickness of rudder plate over the whole area, and the variation of flexural rigidity over the both axes, respectively. The maximum thickness at the root is 0.108 m and at the tip is 0.09 m.

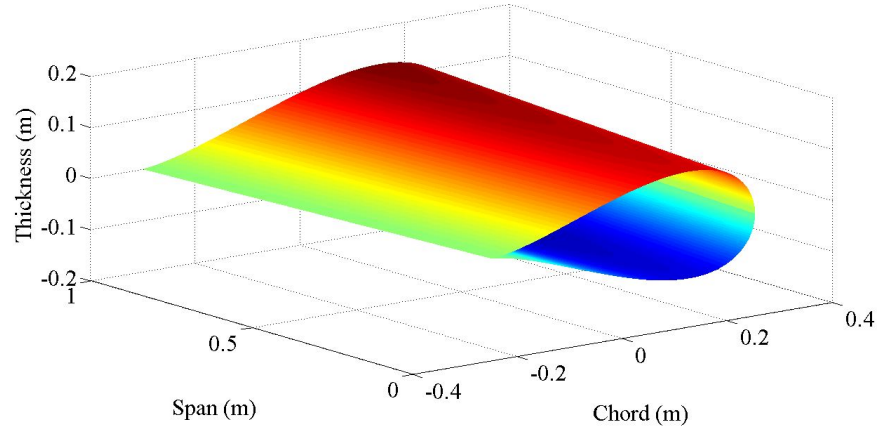


FIGURE 4.5: Thickness distribution of rudder

The distribution of flexural rigidity is cubic (w.r.t. the thickness) for a solid plate. However, since the rudder is hollow, the distribution of the flexural rigidity is quadratic (w.r.t. the thickness), multiplied by the metal sheet thickness. Since the thickness is zero at both the leading edge and the trailing edge, the flexural rigidity is also zero there as shown in **Fig. 4.6**. Over the chord length from the trailing edge to the leading edge, it is the third-quarter of the aerofoil section, that stores the maximum strain potential energy leading to increased natural frequencies.

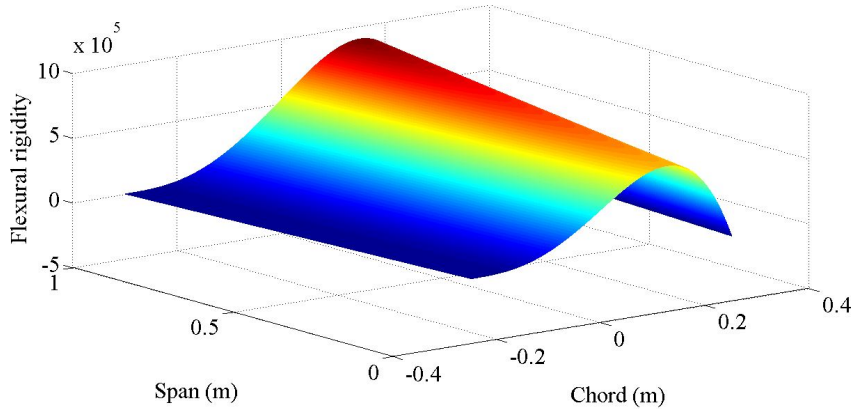


FIGURE 4.6: Variation of flexural rigidity

Table 4.4 shows the dry frequencies of rudder vibration, with ‘ k ’ as the plate mode number, and ‘ j ’ and ‘ l ’ represent the *dominant* span-wise and chord-wise beam mode number. Galerkin’s-I slightly overpredicts the natural frequencies, due to the approximate estimation of the plate flexural rigidity components. In this method; D_x , D_y and D_{xy} have been calculated based on the average thickness of the mean chord. Galerkin’s-II considers the local thickness, $h(x,y)$, thus providing a more accurate spatial distribution of the plate flexural rigidity, $D(x,y)$. In the fundamental frequency of the plate, the contributions of the fundamental beam modeshapes from both the directions are prominent. The last column shows the percentage difference of Galerkin’s-II results w.r.t. Galerkin’s-I results. The higher order modeshapes show a large difference in frequencies calculated in the two methods. This is because the averaged stiffness distribution used in Galerkin-I becomes a crude approximation as the wave number in each direction increases. Since Galerkin’s-II follows the exact local thickness and stiffness distribution, it gives more acceptable lower natural frequencies.

TABLE 4.4: Dry frequencies of Rudder I from theoretical analysis

k	j	l	Frequency (Hz) (Galerkin’s I)	Frequency (Hz) (Galerkin’s II)	Difference (%)
1	1	1	66.00	65.20	1.21
2	1	2	75.92	75.35	0.75
3	1	3	125.98	125.31	0.53
4	2	1	133.89	129.79	3.06
5	2	2	140.28	134.04	4.45
6	2	3	146.23	144.07	1.48
7	3	1	321.50	312.13	2.91
8	3	2	332.97	319.73	3.98
9	3	3	346.09	331.27	4.28

The modal participation of each non-uniform beam modeshape, in either direction, to each plate modeshape is shown in **Table 4.5**. Each elements stands for A_{jl}^k , with $j = 1\text{-}3$, $l = 1\text{-}3$ and $k = 1\text{-}9$. In each of the nine weight matrices for the respective nine modeshapes, one term is dominant and the others are a fraction of it. For example, for $A_{2,3}^6$, the product of the second span-wise modeshape and the third chord-wise modeshape dominates, giving the maximum weight to the element (2,3) in the respective weight matrix.

TABLE 4.5: Modal participation in non-uniform beam vibration

Mode	$j = 1$			$j = 2$			$j = 3$		
	$k = 1$			$k = 4$			$k = 7$		
$l = 1$	-1.000	-0.146	0.096	0.243	0.038	-0.027	-0.007	-0.052	-0.014
	-0.025	-0.004	0.003	-1.000	-0.162	0.090	-0.045	0.059	0.013
	-0.084	-0.013	0.009	0.044	0.006	-0.004	1.000	0.458	-0.056
	$k = 2$			$k = 5$			$k = 8$		
$l = 2$	0.311	-1.000	-0.136	0.127	-0.429	-0.056	0.128	-0.48	-0.074
	-0.064	0.191	0.025	0.341	-1.000	-0.133	-0.082	0.226	0.034
	0.067	-0.118	-0.018	0.084	-0.037	-0.012	0.900	-1.000	-0.166
	$k = 3$			$k = 6$			$k = 9$		
$l = 3$	-0.033	-0.052	-1.000	0.037	-0.019	-0.214	-0.053	0.026	0.291
	0.023	0.012	0.273	0.064	0.048	1.000	0.029	0.003	0.138
	0.003	-0.003	-0.053	-0.038	-0.014	-0.302	0.125	0.046	1.000

Fig. 4.7-4.15 shows the first $3 \times 3 = 9$ flexural modeshapes of the rudder, modelled as Kirchhoff's plate. **Fig. 4.7** shows the *fundamental* ($k = 1$) plate modeshape with the dominance of the *first* ($j = 1$, $l = 1$) beam mode in both chord-wise and span-wise directions, whereas, **Fig. 4.10** shows the *fourth* ($k = 4$) modeshape with dominance of *first* ($l = 1$) beam modeshape in chord-wise direction and of *second* ($j = 2$) beam modeshape in span-wise direction. For $k = 1$, root chord is the only nodal line. For $l = 1$ as j increases, nodal lines parallel to the chord begin to appear. Keeping j constant, as l increases, nodal lines parallel to the span begin to appear. The respective boundary conditions are obeyed by all the four edges of the plate, since they are a combination of the non-uniform beam modeshapes, which have already satisfied the boundary conditions.

If the rigid body modeshapes for the chord had been included, two trivial modeshapes, with lower natural frequencies, would have also participated from the Galerkin's method. They would stand for the pure bending and pure twisting of the plate along and about its span respectively.

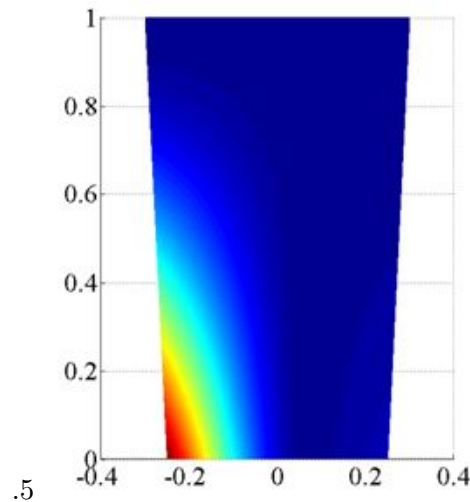


FIGURE 4.7: First (1,1) modeshape

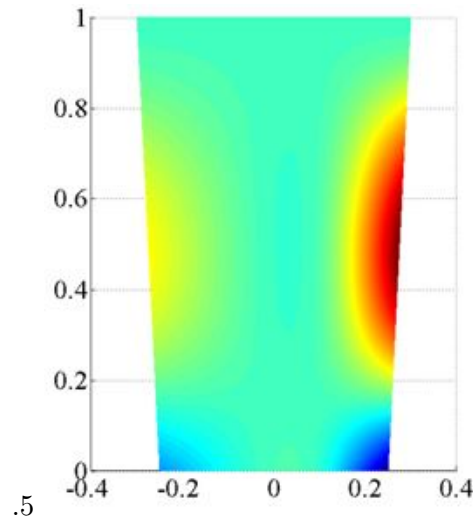


FIGURE 4.8: Second (2,1) modeshape

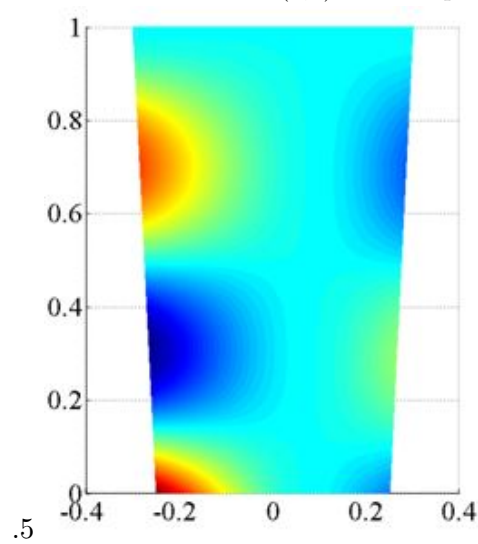


FIGURE 4.9: Third (3,1) modeshape

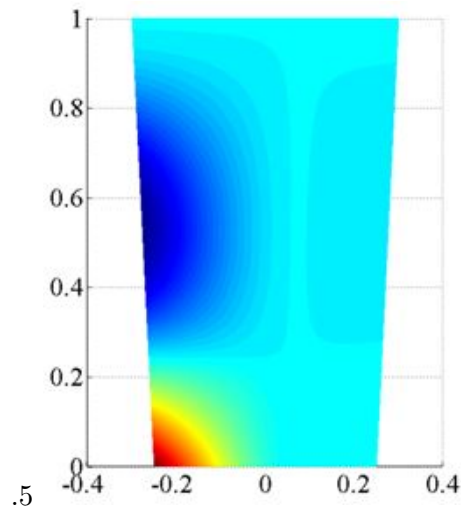


FIGURE 4.10: Fourth (1,2) modeshape

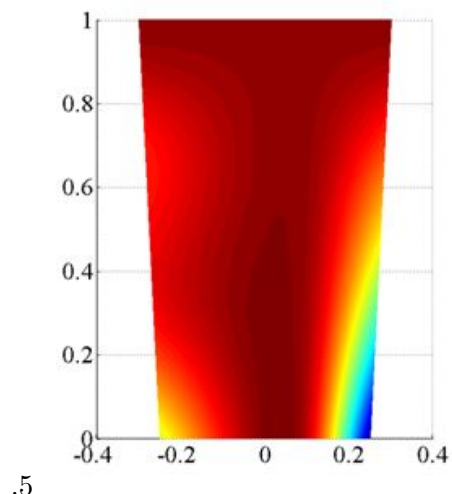


FIGURE 4.11: Fifth (2,2) modeshape

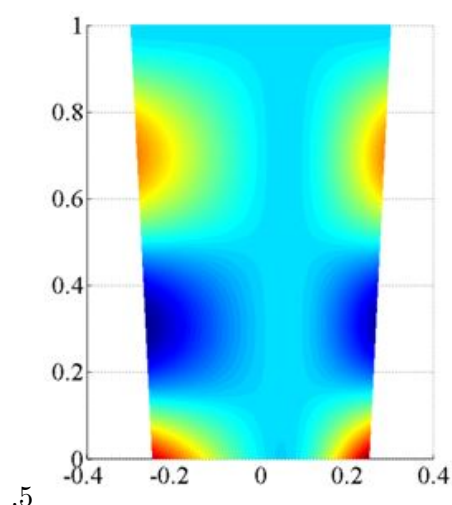


FIGURE 4.12: Sixth (3,2) modeshape

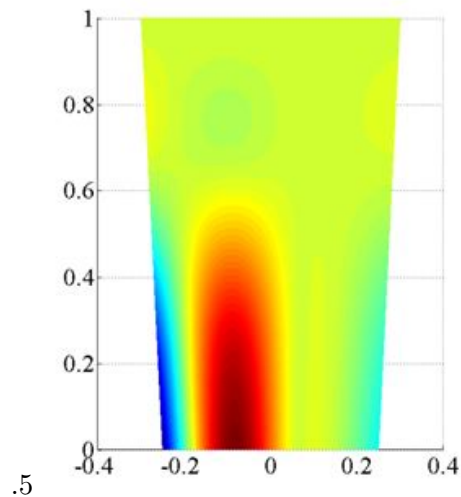


FIGURE 4.13: Seventh (1,3) modeshape

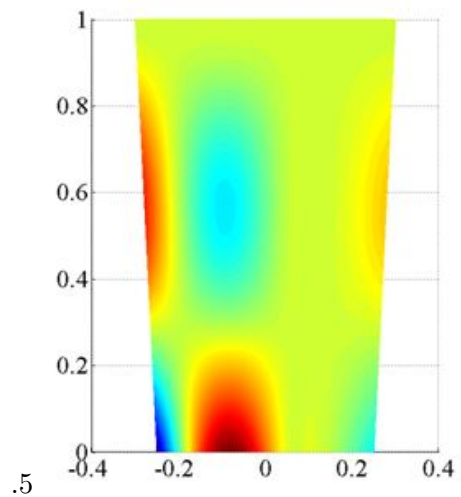


FIGURE 4.14: Eighth (2,3) modeshape

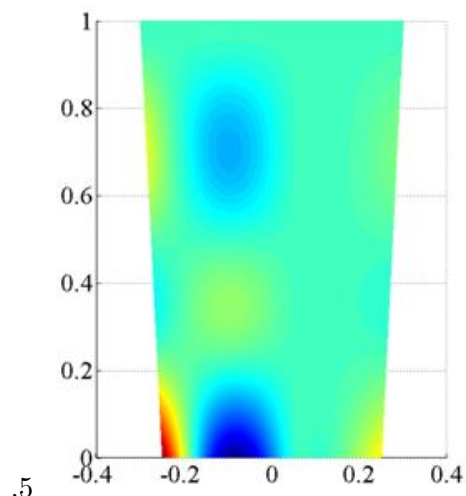


FIGURE 4.15: Ninth (3,3) modeshape

A closed form solution to the plate vibration is not possible, since the governing differential equation can not be decomposed into two ordinary differential equations in x and y . Hence a series solution is reached through the Galerkin's method. Longer the series, more is the accuracy of the resulting frequency. Each beam modeshape, in either direction, contributes to the natural frequency of plate vibration. As the number of modeshapes taken increases, the natural frequency converges to a constant value, showing that modeshapes higher than this do not participate in plate vibration. The Galerkin's method involves a integration of the inner product of the beam modeshapes and their derivatives. If this integration is done analytically, the accuracy of the Galerkin's method is enhanced. But since the modeshapes contain a combination of sinusoidal and hyperbolic functions, the analytical integration of their product becomes extremely tedious and computationally expensive. Thus numerical integration of the inner products becomes an efficient way to avoid the above. However, as a limitation of all numerical procedures, the number of discrete elements affects the accuracy of the results. The spatial discretization in each direction should be sufficient to smoothly generate the higher order spatial wavelengths.

The model-scale frequencies can be converted to that of actual full-scale rudder, by using the non-dimensional similarity. The non-dimensional frequency is a ratio of the dimensional frequency to the non-dimensionalizing term, i.e $\omega_{Non-D} = \frac{\omega}{\sqrt{D/mL^2B^2}}$, where 'D' is the flexural rigidity, 'L' is the rudder span length and 'B' is the root chord length. The full-scale geometrical and material properties known, the full-scale natural frequency can be calculated.

4.1.1.3 Numerical analysis : ANSYS 15

Table 4.6 shows the variation of dry plate vibration frequencies for first 10 modes. Because ANSYS is a numerical tool, it also considers the effect of rigid body modeshapes both translational and rotational. Hence, the frequencies are lower compared to those obtained from theoretical analysis. Comparing with **Table 4.4**, the frequencies corresponding to mode number 1,3,4,5 are seen in ANSYS results with some error. The frequency corresponding to mode *two* can be obtained by increasing the discretization.

TABLE 4.6: Dry plate vibration frequency variation in ANSYS

Mode	Frequency (Hz)	Mode	Frequency (Hz)
1	55.963	6	108.43
2	66.361	7	111.92
3	67.607	8	129.73
4	86.030	9	138.49
5	104.80	10	139.51

4.1.2 Wet Vibration

With the preliminary dry vibration analysis done, this sub-section deals with the wet free vibration of the plate. The fluid inertia is estimated by two ways:

- Potential flow theory
- Two-dimensional Green's function technique

The NACA0018 aerofoil profile is approximated as a Joukowski aerofoil (section) by minimizing the error in terms of three distinct parameters, i.e. (i) area, (ii) perimeter, and (iii) maximum thickness (**Table 4.7**). The fineness ratio e is adjusted to optimize the aerofoil shape to be as close and similar as possible to a NACA profile. Among the three parameters, the perimeter optimization is a priority, because all hydrodynamic forces are generated by integrating the hydrodynamic pressure over the perimeter. The area of the Joukowski aerofoil can be expressed as πeb^2 , and maximum thickness as $\frac{be(3\sqrt{3})}{2}$, which occurs at $0.5b$ from the leading edge. This is detailed in **Appendix 2**.

TABLE 4.7: Joukowski transformation error analysis

Aerofoil	e	Error % Area	Error % Perimeter	Error % Maximum thickness
NACA0015	0.122	6.80	-0.45	-5.56
NACA0018	0.146	7.05	-0.56	-5.36
NACA0021	0.171	6.69	-0.722	-5.78

The 2D sway added mass of a the aerofoil can be expressed as $a_{2D} = \rho A a_{2D,NonD}$, where $a_{2D,NonD}$ is the 2D sway non-dimensional added mass, which is equal to 1.0. Here, $A = \pi eb^2$ is area of aerofoil section. The 2D yaw added mass moment of a Kutta-Joukowski aerofoil can be expressed as $am_{2D} = \rho Ac^2 am_{2D,NonD}$, where $am_{2D,NonD}$ is the 2D yaw non-dimensional added mass moment, and c is chord of aerofoil. Such non-dimensional coefficients can be estimated by theoretical hydrodynamics, by representing the flow as a combination of dipoles, and by satisfying the no-penetration body boundary conditions

The 3D sway added mass and yaw added mass moment are calculated by integrating their 2D counterparts over the span of the rudder, followed by empirical 3D corrections (McCormick et al (2004)). The resultant 3D sway added mass and yaw added mass moment calculated by the Potential flow theory, and by the 2D source distribution technique is shown in **Table 4.8**.

TABLE 4.8: 3D added mass by strip theory

Aerofoil	Sway added mass (Theoretical)	Sway added mass (Numerical)	Error (%)
NACA0015	29.79	30.60	2.71
NACA0018	35.65	36.70	2.94
NACA0021	41.76	43.10	3.20

The 3D corrections are independent of mode number (order) of vibration of the rudder. For higher order modes, the mode shape approaches a sinusoidal function, and the corresponding hydrodynamic functions are assumed to be proportional to the corresponding displacements. The comparison of dry and wet vibration frequencies of rudder is shown in **Fig. 4.16**. The modal added mass depends on the actual three-dimensional plate mode shape $\Phi_k(x, y)$. It is also a function of the boundary conditions and the aspect ratio of the plate. Structural acceleration of a particular mode shape is likely to influence the radiation pressure associated with another mode shape. However, the cross-coupling terms in the fluid inertia matrix are ignored as of now.

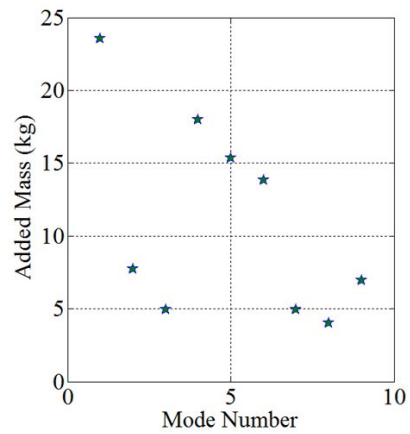


FIGURE 4.16: Added mass w.r.t. plate mode number

4.2 Full-scale rudder with classical pivot (Rudder-II)

In this section, a spade rudder has been modeled as a hollow unstiffened Kirchhoff's plate, with variable thickness both along the span and along the chord. It has an identical geometry as Rudder-I, except that its linear dimensions are scaled up ten times, to match the actual geometry of the Korean Container Ship. The edges of the plate are considered to be completely free; except at the **pivot**, where the displacement is zero. The family of problems solved for this rudder model are shown in **Table 4.9**. Theoretical analysis has been done for the free dry and wet vibration. The dry vibration has been verified for numerical analysis. Additionally, forced vibration analysis has been done theoretically, to study the dynamic response to propeller-induced-vibration (PIV). The hydrodynamic load on the rudder is estimated empirically, while the response is calculated by the modal-superposition technique.

TABLE 4.9: Family of problems for Rudder II

	Theoretical	Numerical	Experimental
Free dry vibration	✓	✓	
Free wet vibration	✓		
Forced wet vibration	✓		

4.2.1 Dry vibration

The free dry vibration is studied by the energy-based Galerkin's method. The wet natural frequencies are calculated by the 3D constant-strength source distribution technique. The hydrodynamic loading is estimated from the Harrington's power prediction method. The wet forced vibration of the idealized rudder is studied, generating the dynamic stress components as functions of space and time, for a range of rudder angles.

4.2.1.1 Beam Modeshapes

Fig. 4.17 and **Fig. 4.18** shows the first three uniform and non-uniform modeshapes in span-wise and chord-wise directions respectively. The solid lines represent the non-uniform beam modeshapes, while the dashed lines represent the uniform beam modeshapes. In **Fig. 4.17**, the left side is the free end (tip chord) while the right side is the pivoted end (root chord). However, due to high non-uniformity of the chord-wise section's NACA0018 airfoil shape, the non-uniform modeshapes deviate considerably from uniform ones in chord-wise direction.

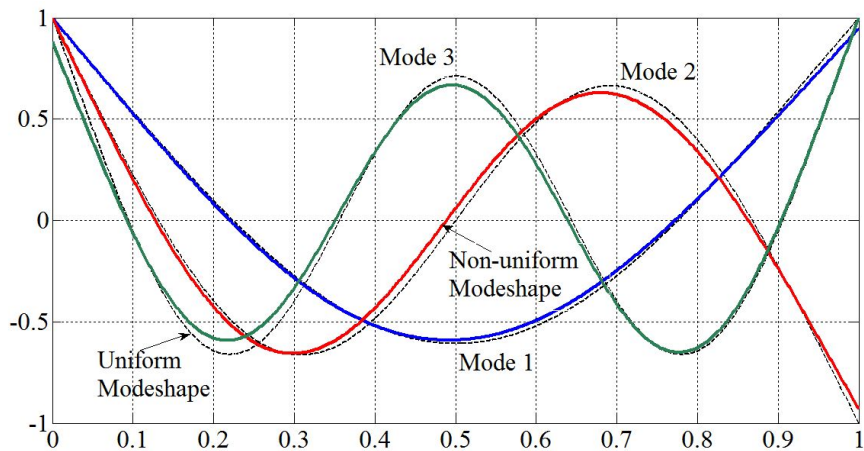


FIGURE 4.17: Span-wise beam modeshapes (model scale 1 : 10)

In **Fig. 4.18**, the left side is the trailing edge while the right side is the leading edge. The chord-wise modeshapes are shown for the mean chord. In the span-wise direction, the deviation of the non-uniform modeshape from the uniform (elementary) ones, is just

marginal; due to a very mild taper. The uniform modeshapes are symmetric or anti-symmetric about the midpoint, depending on whether it is an even or an odd mode. The non-uniformity causes the beam to lose its symmetry/anti-symmetry, as evident in **Fig. 4.17, 4.18**. All the modeshapes are normalized, i.e. they vary between ± 1 .

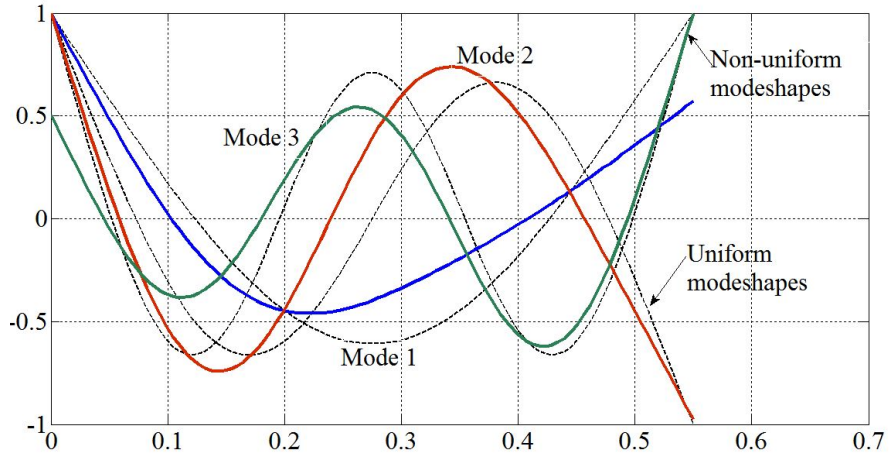


FIGURE 4.18: Chord-wise beam modeshapes (model scale 1 : 10)

4.2.1.2 Plate Modeshapes and frequencies

The first $3 \times 3 = 9$ dry plate modeshapes are shown in **Fig. 4.19**. In first row has the first span-wise modeshape dominantly coupling with the first, the second, and the third chord-wise modeshape (left to right). The first column has the first chord-wise modeshape dominantly coupling with the first, the second, and the third span-wise modeshape (top to bottom). As the chord-wise mode index increases, nodal lines parallel to the span begin to appear. As the span-wise mode index increases, nodal lines parallel to the chord begin to appear. The first sub-figure represents the domination of first modeshape both in span and chord-wise directions, while the last sub-figure shows the domination of third modeshape in both span and chord-wise directions. In each sub-figure of **Fig. 4.19** has deflection zero at the pivot point only.

The dry natural frequencies, in Hz, are shown in **Table 4.10**, where ' j ' denotes the dominating mode in span-wise direction and ' l ' represents dominating one in chord-wise direction. The fundamental non-dimensional frequency is 2.3, when the first chord-wise and first span-wise modeshape dominates to generate the plate modeshape. For $(j,l)=(2,1)$, the frequency increases to 4.7; while for $(j,l)=(1,2)$, the frequency increases to 6.3. This is because the second chord-wise mode has more bending strain than the second span-wise mode. If the plate was uniform and square, the frequencies corresponding to $(j,l)=(2,1)$ and $(j,l)=(1,2)$, would have been equal with mirror image modeshapes. The same pattern is seen in $(1,3)$ and $(3,1)$.

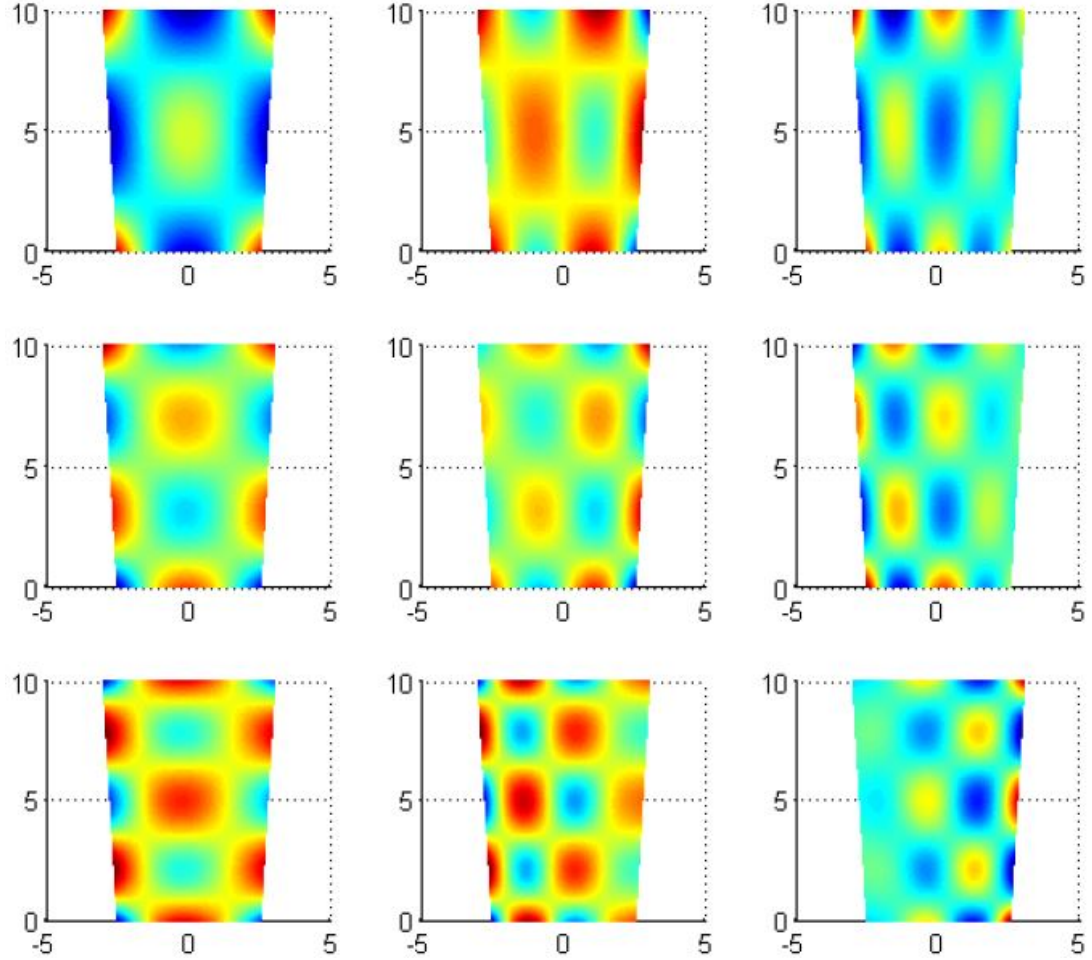


FIGURE 4.19: Full scale rudder mode shapes

TABLE 4.10: Dry frequencies of Rudder-II with classical pivot

k	j	l	Frequency (Non-D)	Frequency (Hz)
1	1	1	2.30	57.90
2	2	1	4.712	118.27
3	1	2	6.304	158.239
4	3	1	8.443	211.929
5	2	2	8.566	215.008
6	1	3	9.353	234.753
7	2	3	10.903	273.662
8	3	3	12.246	307.360
9	3	2	14.428	362.134

The modal participation of each non-uniform beam modeshape, in either direction, to each plate modeshape, is shown in **Table 4.11**. Here, for $(j,l)=(1,1)$, it shows the domination of first beam modeshape in both span-wise and chord-wise directions in

first plate modeshape. Similarly, $(j,l)=(3,2)$ represents the domination of third beam modeshape in span-wise direction and second beam modeshape in chord-wise direction in corresponding plate modeshape. Each element of the weight matrix represent the weight A_{jl}^k ; i.e. the weight of the contribution of the product of the j^{th} span-wise non-uniform modeshape and the l^{th} chord-wise non-uniform modeshape, to the k^{th} plate modeshape. The first row stands for the dominant chord-wise modeshape, while the first column stands for the dominant span-wise modeshape, to the respective plate modeshape $\Phi_k(x, y)$.

TABLE 4.11: Modal participation of rudder with classical pivot

Mode No.	$l=1$			$l=2$			$l=3$			
	$k = 1$			$k = 3$			$k = 6$			
$j=1$	-1.0 - .192 0			-.1978 1.0 -.5856			-.0909 .5734 1.0			
	-.0277 -.0053 0			-.0054 .028 -.0165			-.0012 .017 .0285			
	.001 .0002 .0001			.002 -.0014 .0008			.0205 .0005 .0014			
$j=2$	$k = 2$			$k = 5$			$k = 7$			
	.0279 .0044 .0002			-.0058 .0298 -.0216			.001 -.026 -.033			
	-1.0 -.1528 -.0096			.1895 -1.0 .8012			-.055 .84 1.0			
$j=3$	$k = 4$			$k = 8$			$k = 9$			
	-.02 .017 -.025			.041 .012 .159			.013 .11 .082			
	-.067 -.01 .0005			.012 -.033 .076			-.003 .072 .035			
-1.0 -.109 -.019			.162 -.516 1.0			-.039 1.0 .456				

4.2.2 Wet vibration

In order to study, the propeller-induced-vibration of a submerged rudder behind the propeller wake, it is important to first calculate the wet natural frequencies of the rudder. During operation, the PIV frequency should not resonate with one of the wet natural frequency.

4.2.2.1 Wet free vibration

Fig. 4.20 shows the deviation of first $3 \times 3 = 9$ in wet plate vibration frequencies, from the corresponding dry plate vibration frequencies, due to the effect of added mass. The modal added masses have been calculated by the 3D constant strength source distribution technique, as detailed in **Appendix D**. The magnitude of the added mass associated with each modeshape depends on the volume enclosed by the plate mode-shape. The dry and the wet frequencies follows a consistent trend. The fluid inertia lowers the natural frequencies by nearly 50 %.

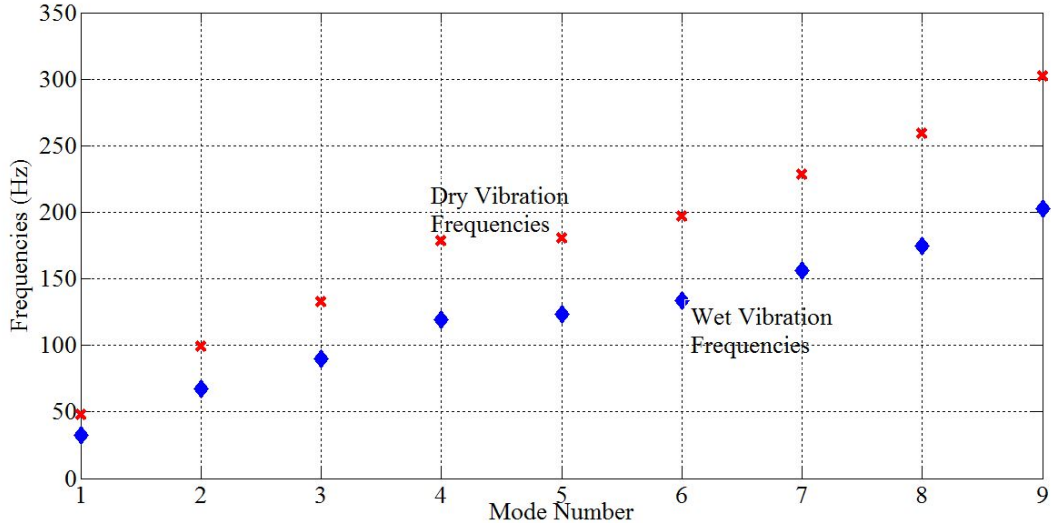


FIGURE 4.20: Dry and wet natural frequencies

4.2.2.2 Wet forced vibration

Table 4.12 shows the maximum magnitudes of the three stress components of the dynamic plane stress problem, at a range of rudder angles. The corresponding maximum deflections are also tabulated. The total hydrodynamic force is calculated by the Harrington's power prediction method. The variation of the lift coefficient is considered to be parabolic over the span of the rudder, and the corresponding force distribution is calculated. The force is assumed to be harmonic in time, oscillating at the PIV frequency. More accurately, the force is periodic in time, acting as repeated impulses. If the duration between two consecutive impulses is more than the fundamental natural period of the plate, the free vibration of the rudder is also seen.

TABLE 4.12: Maximum Dynamic Stresses and Deflection for different rudder angles

Rudder angle δ	$\delta = 7^0$	$\delta = 14^0$	$\delta = 21^0$	$\delta = 28^0$	$\delta = 35^0$
Max. Deflection (mm)	0.052	0.091	0.142	0.0188	0.0227
Max. σ_x (MPa)	16.13	27.94	43.33	57.48	69.66
Max. σ_y (MPa)	40.05	69.36	107.56	142.69	172.93
Max. τ_{xy} (MPa)	20.54	35.58	55.17	73.19	88.70

The normal stresses distributions in x and y direction, and the twisting stress spatial distribution about x or y direction, are calculated and shown in **Fig. 4.21**. The spatial distribution of the total deflection for different rudder angles is also shown in **Fig. 4.21**. The maximum deflection and the maximum bending stress magnitudes occur in phase with each other, while the maximum twisting moment magnitude occurs at a phase difference of $\pi/2$. The deflection and the twisting moment is zero at the pivot, while the bending stresses are maximum there.

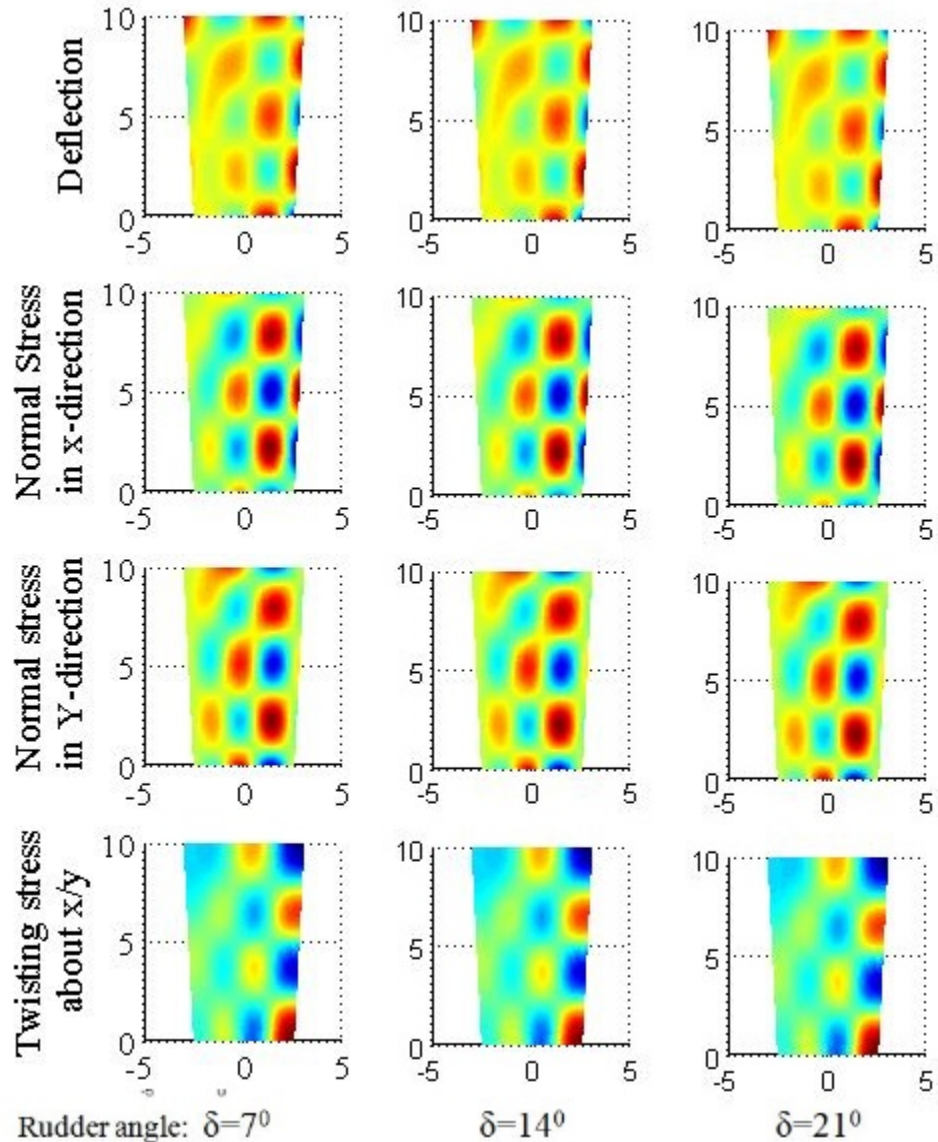


FIGURE 4.21: Maximum deflection and Stress components spatial distribution

The spatial distribution of the static deflection and stress components in a steady flow is shown in **Fig. 4.22** and **Fig. 4.23**. The static deflection is nearly similar to the fundamental modeshape. The parabolic distribution of the force matches with the first span-wise mode. The maximum value of deflection and stress components in steady flow for different rudder angles is shown in **Table 4.13**. Comparing **Table 4.12** and **Table 4.13**, the maximum deflection in the static deflection is seen to be larger than the maximum dynamic deflection. The static analysis involves the dry inertia term only; while the wet dynamic analysis includes the wet inertia term, which reduces the magnitudes of the dynamic deflections and the dynamic stresses.

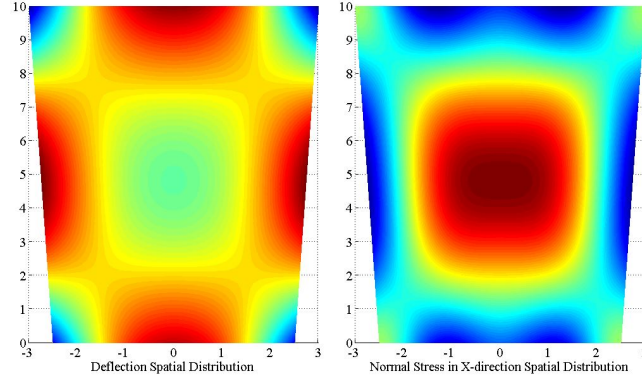


FIGURE 4.22: Steady deflection and Normal stress in X-direction spatial distribution

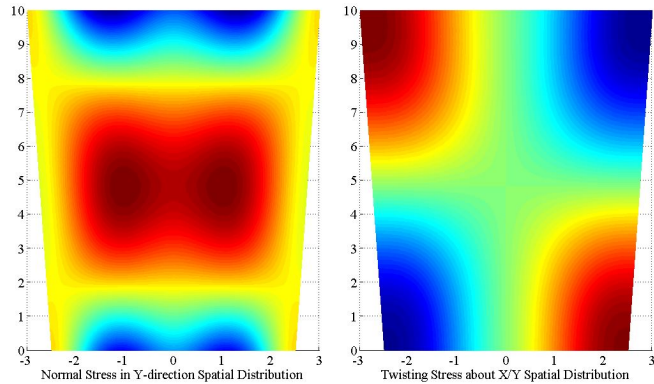


FIGURE 4.23: Steady Normal stress in Y-direction and Twisting Stress about X or Y spatial distribution

TABLE 4.13: Maximum Steady Stresses and Deflection for different rudder angles

Rudder angle δ	$\delta = 7^0$	$\delta = 14^0$	$\delta = 21^0$	$\delta = 28^0$	$\delta = 35^0$
Max. Deflection (mm)	0.83	1.4	2.2	3.0	3.6
Max. σ_x (MPa)	40.5	70.1	108.5	143.8	174.0
Max. σ_y (MPa)	78.3	135.6	209.9	278.2	336.6
Max. τ_{xy} (MPa)	93.1	161.0	249.1	329.8	398.6

Chapter 5

Work Extension : Experimental Work on Rudder - III

This chapter is an extension of the previous work detailed in Chapter 4. The theoretical work was verified by numerical analysis. The third angle of scientific and numerical integration, has been attempted here. A realistic mild steel rudder was fabricated for three separate tests:

- (i) Dry free vibration impact test : frequencies measured,
 - (ii) Wet free vibration impact test : frequencies measured,
 - (iii) Forced vibration behind propeller slipstream tested;
- as shown in **Table 5.1**. The experiments were done in High Speed Towing Tank (HSTT) of Hydrodynamic Research Wing (HRW) at the **Naval Science and Technological Laboratory (NSTL), DRDO**, Vishakhapatnam, Seemandhra; under the authorization of Mr. Manu Korulla (Associate Director, Sc G). The rudder model was constructed at **AP Engineering works, Kolkata**, by Mr. Chiranjeev Naskar, and was named *Asha* (**Fig. 5.1**).



FIGURE 5.1: Rudder - III

TABLE 5.1: Family of problems for Rudder III

	Theoretical	Numerical	Experimental
Free dry vibration		✓	✓
Free wet vibration			✓
Forced wet vibration			✓

The family of problems solved for Rudder-III are shown in **Table 5.1**. The free and forced vibration study is done experimentally. The free dry vibration is compared with

the numerical analysis.

5.1 Stiffened Rudder Model

The rudder model (**Fig. 5.1**) is a scaled-down model of a Korean Container Ship (KCS) rudder, whose dimensions are shown in **Table 5.2**. The rudder model is on the scale of 1:31.25 to full scale. The rudder is stiffened by five transverse equally-spaced bulkheads, with first and last bulkhead at the root chord and the tip chord respectively. The span of rudder stock outside rudder is 10 cm and it goes deep inside rudder till 3rd bulkhead, i.e. till the middle of rudder span as shown in **Fig. 5.2**.

TABLE 5.2: Rudder full-scale and model information

	Full-scale	Model	Dimensions
Span	10	0.32	m
Mean chord	5.5	0.176	m
Root chord	6	0.192	m
Tip chord	5	0.16	m
Support	Stock	Stock	
Diameter of Propeller	7.9	0.25	m
Stock Diameter	375	12	mm
Speed of ship	12	2.1	$k\text{gm}^{-1}$
RPM of propeller	100	562	Rev. per min

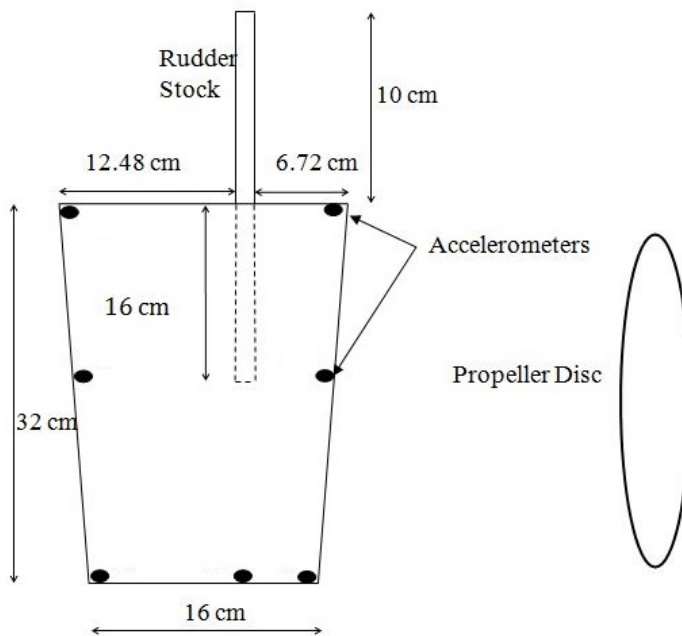


FIGURE 5.2: Rudder Model Geometry

5.2 Propeller Characteristics

A four-bladed propeller was used to develop the wake loading on the rudder placed behind it. The propeller model particulars are shown in **Table 5.3**. The variation of its thrust coefficient (K_T), torque coefficient (K_Q) and the open water efficiency (η_0) as functions of the advance ratio (J) is shown in **Fig. 5.3** and their formulations are shown as follows :

$$K_T = \frac{T}{\rho n^2 D^4} ; \quad K_Q = \frac{Q}{\rho n^2 D^5} ; \quad J = \frac{V_A}{2\pi} ; \quad \eta_0 = \frac{K_T}{K_Q} \frac{J}{2\pi}$$

where,

T : Thrust ; Q : Torque ; V_A = Advance velocity;

n : rev.per sec. ; D : Diameter of Propeller ; ρ : Density of water.

TABLE 5.3: Propeller Model Particulars

Propeller type	FPP
Sense of rotation	Right
No. of propeller blades	4
Propeller model diameter	250 mm
Propeller immersion	0.253 m
Blade area ratio (A_e/A_o)	0.5500
Pitch ratio at 0.75 R	1.0750
Chord length at 0.75 R	0.0723 m
Blade thickness at 0.75 R	0.0034 m

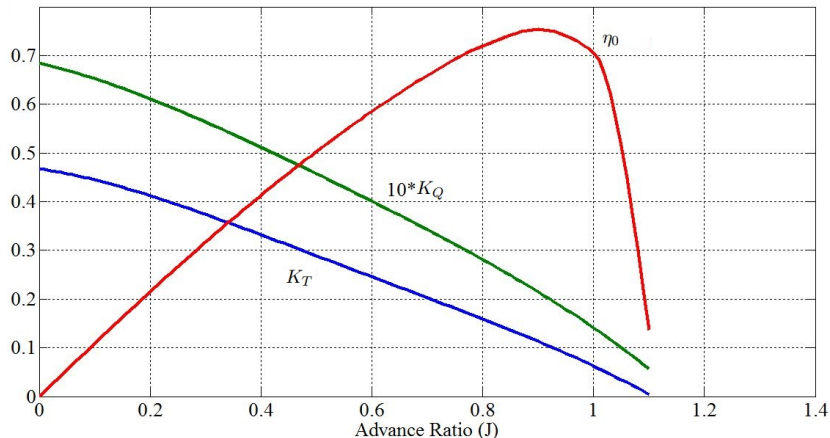


FIGURE 5.3: Thrust coefficient, Torque coefficient and open water efficiency characteristics versus advance ratio

5.3 Experimental Procedure

5.3.1 Experimental Setup

The experimental configuration of rudder with the propeller is shown in **Fig. 5.4**. The rudder was fixed to a hanger by inserting the rudder stock inside a holding stock, and its position with respect to the calm waterline was fixed with the help of M8 bolts. The vertical position of rudder stock was chosen with respect to that of propeller such that **no air suction takes place** due to the rotation of propeller. The distance between the leading edge of rudder at the root chord and the centre of propeller was taken to be 12% of the propeller diameter i.e. 30 mm.

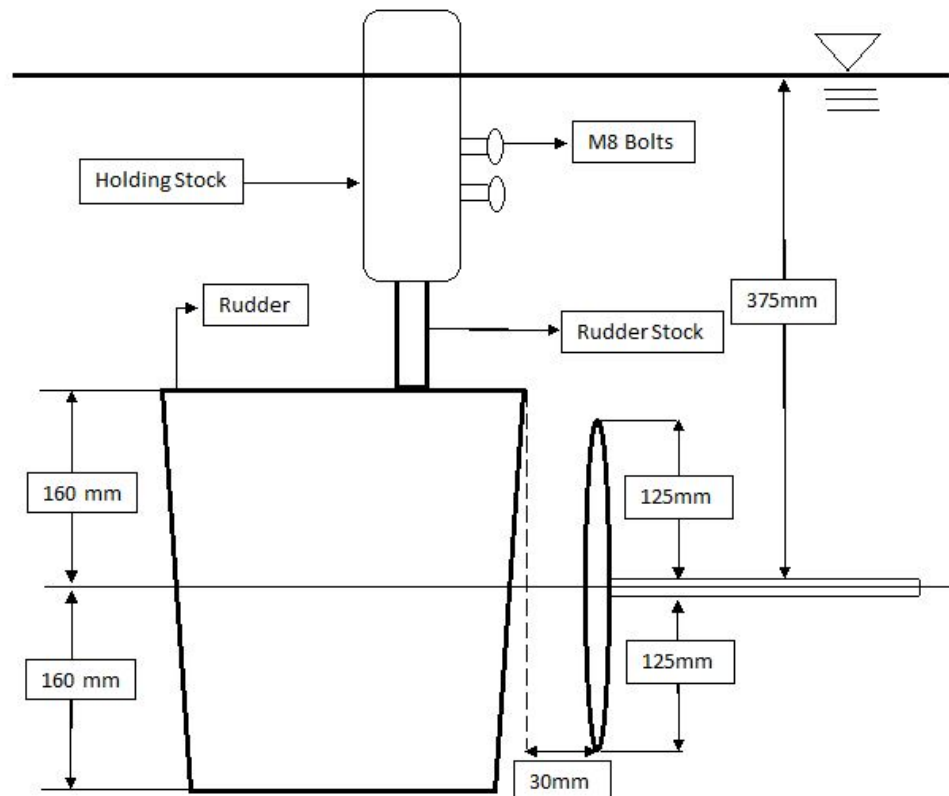


FIGURE 5.4: Experimental configuration for forced wet vibration test

5.3.2 Free Dry Vibration

First, the free dry vibration test was performed outside the water without any external forcing. The deflections and accelerations were measured with the help of an accelerometer at 8 different locations denoted as DA_1, DA_2, \dots , as shown in **Fig. 5.5**. The results were converted from the time-domain to the frequency-domain, by using NV-GATE OROS software in order to get the frequencies.

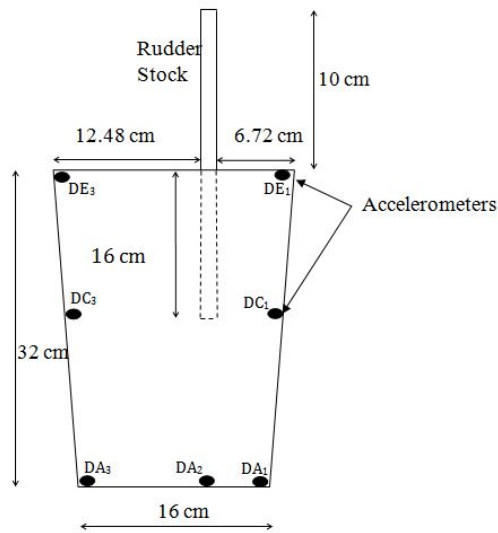


FIGURE 5.5: Accelerometer Position in Free Dry Vibration

The results of the acceleration versus frequency, for different positions of the accelerometer, of free wet vibration are shown in **Fig. 5.6-5.9**. The distinct peaks in the frequency spectrum denote the distinct natural frequencies. The higher the spectrum ordinate of a frequency, the more strongly its is excited, i.e. it has a large amplitude and hence, acceleration amplitude.

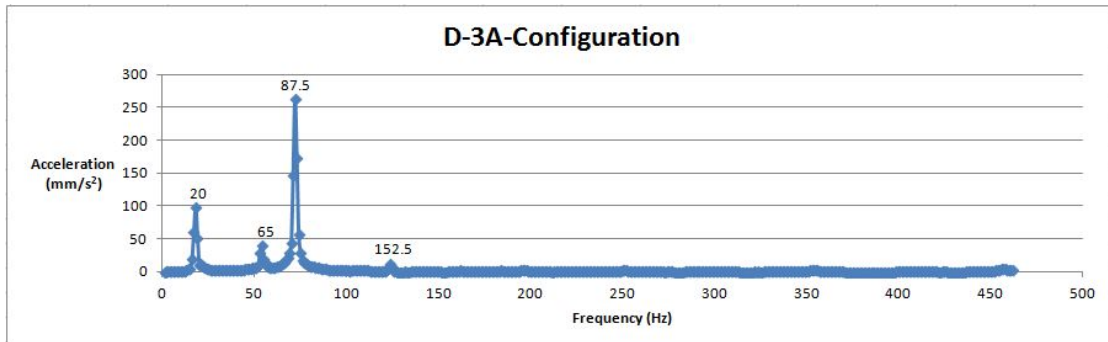


FIGURE 5.6: Acceleration results in frequency domain for configuration D3A

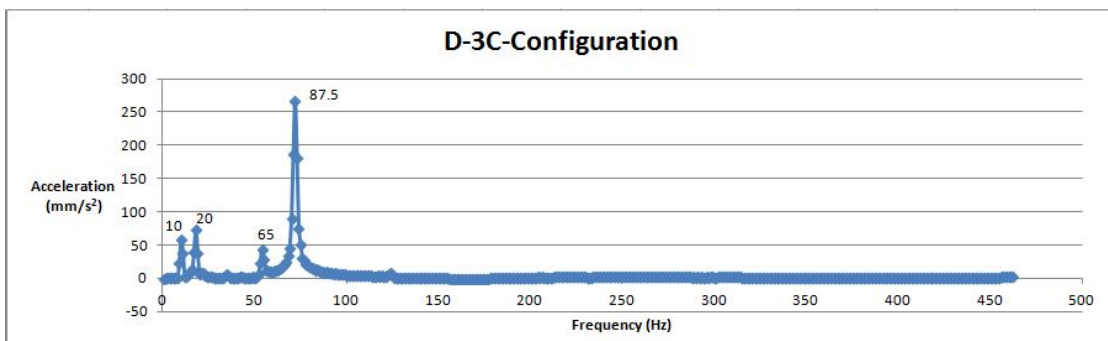


FIGURE 5.7: Acceleration results in frequency domain for configuration D3C

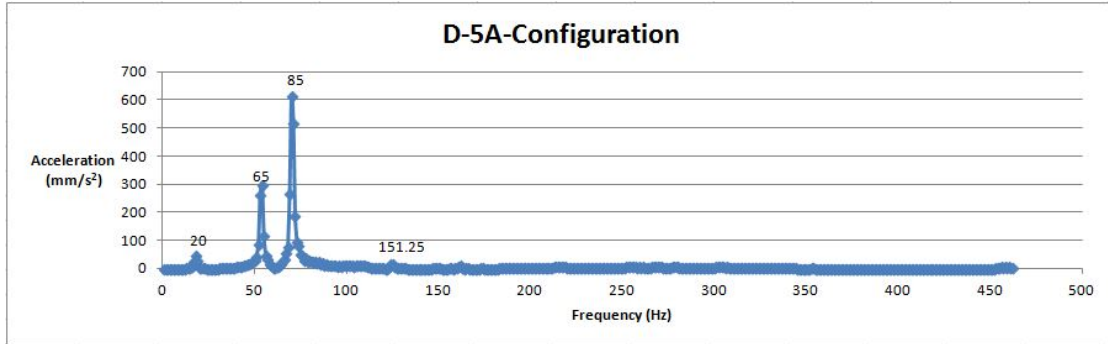


FIGURE 5.8: Acceleration results in frequency domain for configuration D5A

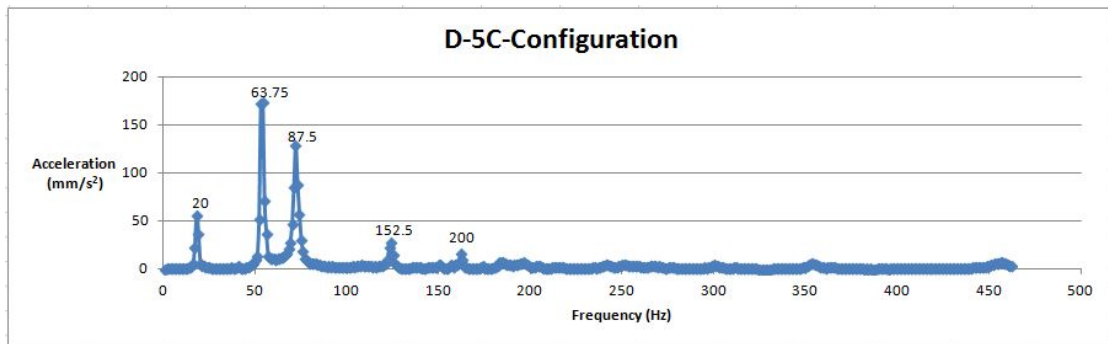


FIGURE 5.9: Acceleration results in frequency domain for configuration D5C

5.3.3 Free Wet Vibration

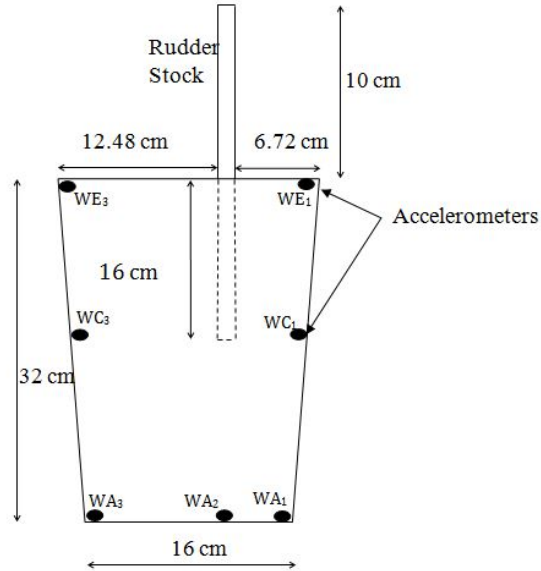


FIGURE 5.10: Accelerometer Position in Free Wet Vibration

The free wet vibration test of the rudder model was done inside the otherwise calm water, without any external propeller gust or wake forcing. The deflections and accelerations were measured with the help of wet accelerometers at 8 different locations denoted as

$WA_1, WA_2\dots$ (shown in **Fig. 5.10**) and the results were again converted from the time domain to the frequency domain, by using NV-GATE OROS software, in order to generate the wet natural frequencies. The results of the acceleration versus frequency for different configurations of free wet vibration as shown in **Fig. 5.10** are shown in **Fig. 5.11-5.14**. For all configurations of the accelerometer, the position of the impact remains the same, which was just on the side of the rudder stock on the root chord. The distinct peaks in the frequency spectrum denote the distinct wet natural frequencies, such as 10, 28.75, 56.25, 117.5 Hz, etc. As the peak corresponding to 56.25 Hz has maximum ordinate, it is the interpreted fundamental wet natural frequency.

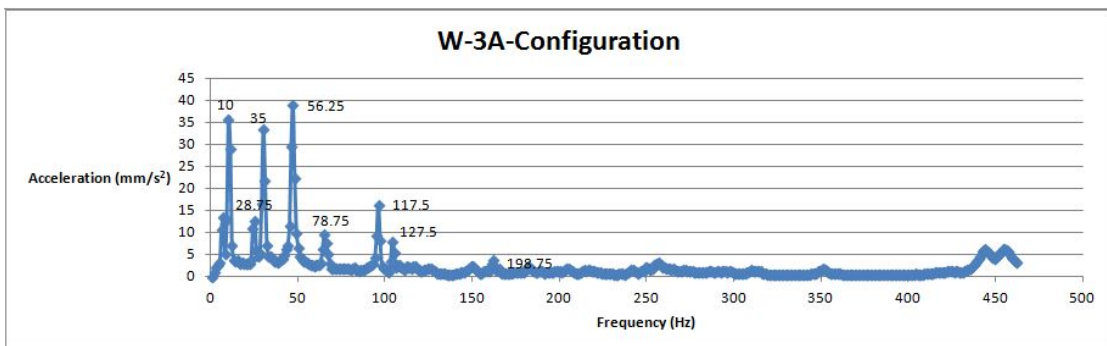


FIGURE 5.11: Acceleration results in frequency domain for configuration W3A

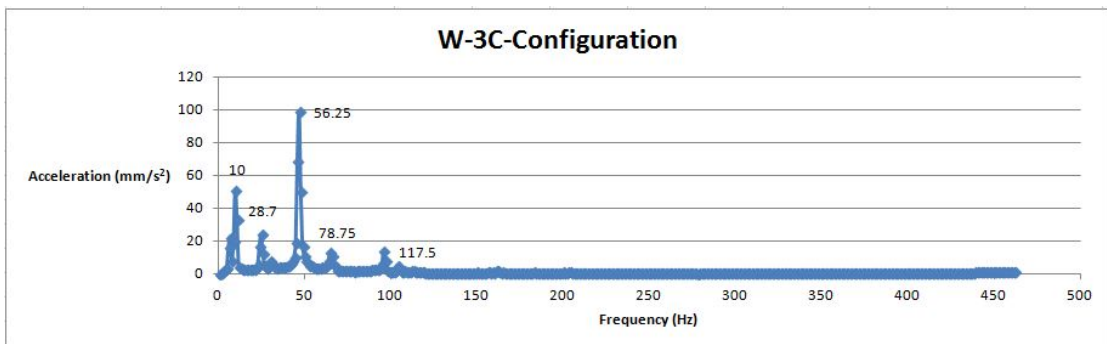


FIGURE 5.12: Acceleration results in frequency domain for configuration W3C

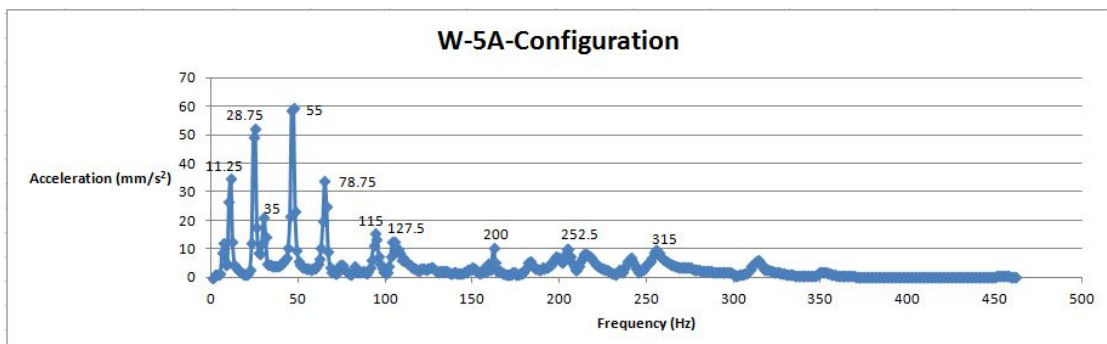


FIGURE 5.13: Acceleration results in frequency domain for configuration W5A

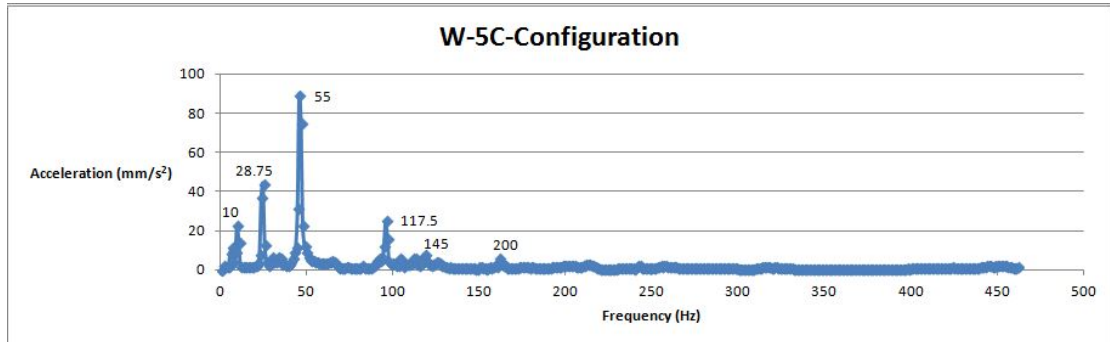


FIGURE 5.14: Acceleration results in frequency domain for configuration W5C

5.3.4 Forced Wet Vibration in Propeller Wake

The rudder vibration analysis was done under the loading of gust of the propeller wake. The readings of deflections were taken at various positions such as A_1, B_1 etc. as shown in **Fig.5.15**.

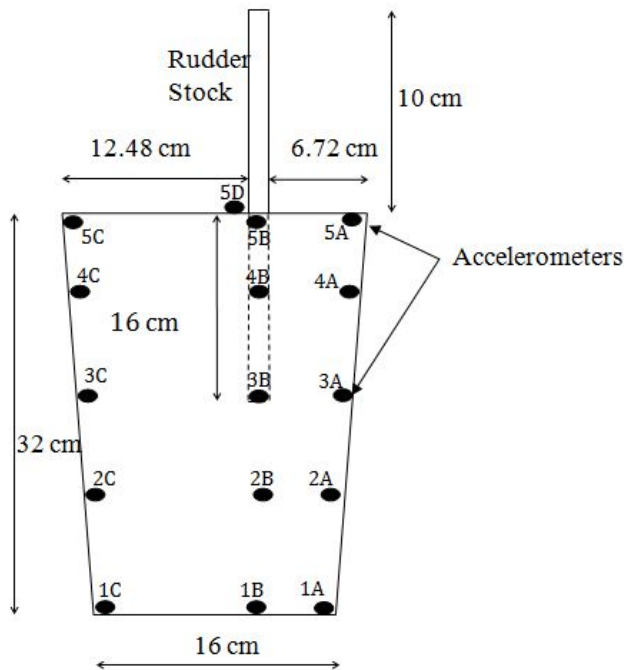


FIGURE 5.15: Accelerometer Position in Wet forced Vibration

Fig. 5.16 shows the actual view of the rudder in the wake of the propeller during the experiment. The discrepancies which occur due to the rudder stock in water are not studied here. In the actual case of the ship, this part is inside the ship hull, and hence does not influence the flow. The thrust and torque applied by the propeller on rudder listed in **Table 5.4**, were calculated by the dynamometer for both at bollard pull condition and at non-zero forward velocity. When the carriage speed was 2.1 m/s , a suitable rpm (500) for the rudder is chosen by considering thrust and torque identities,

such that it match with the actual thrust and torque of actual rudder of KCS ship by Froude Number similarity.

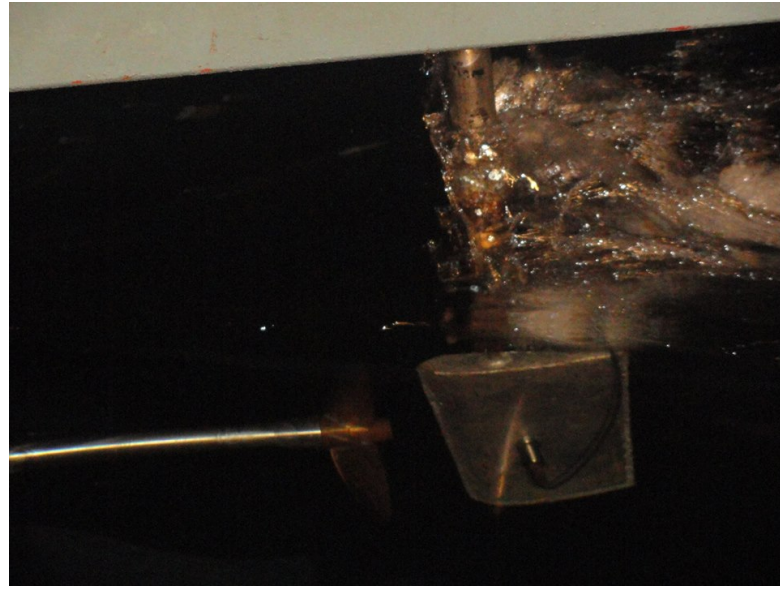


FIGURE 5.16: Rudder in the wake of propeller during wet vibration test under propeller gust at NSTL, Vizag

TABLE 5.4: Average Thrust, Torque and RPM data from dynamometer

Position	Speed (m/s)	Thrust (N)	Torque (Nc)	RPM
A_1	0	-194.651	-1366.05	700.494
A_2	0	-199.134	-1399.94	707.685
A_3	0	-198.900	-1404.77	707.591
B_1	0	-196.542	-1382.37	707.087
B_2	0	-195.112	-1374.86	708.818
B_3	0	-198.538	-1403.66	705.892
C_1	0	-196.403	-1375.99	715.312
C_2	0	-199.316	-1398.08	706.332
C_3	0	-181.636	-1274.12	697.056
D_1	0	-201.051	-1418.06	707.995
D_2	0	-191.080	-1334.27	707.272
D_3	0	-203.999	-1445.50	714.018
E_1	0	-199.969	-1398.81	715.370
E_2	0	-197.818	-1388.19	716.031
E_3	0	-201.526	-1417.17	715.721
C_2 – moving	2.1	-37.159	-229.975	536.240

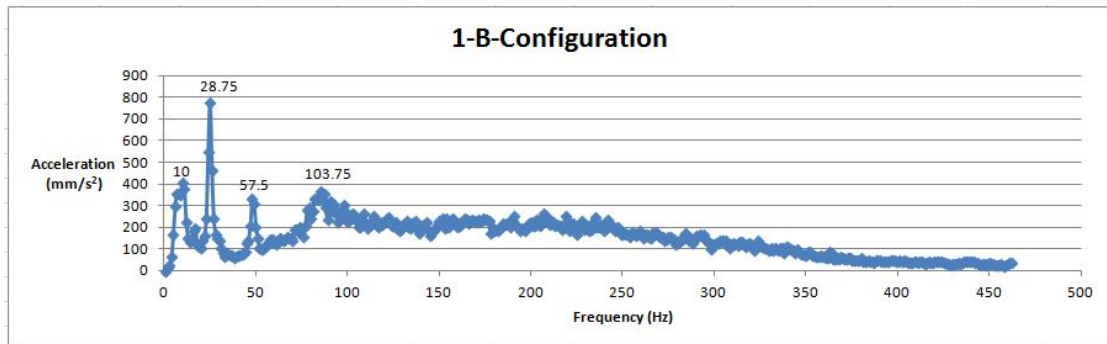


FIGURE 5.17: Acceleration results in frequency domain for configuration 1B

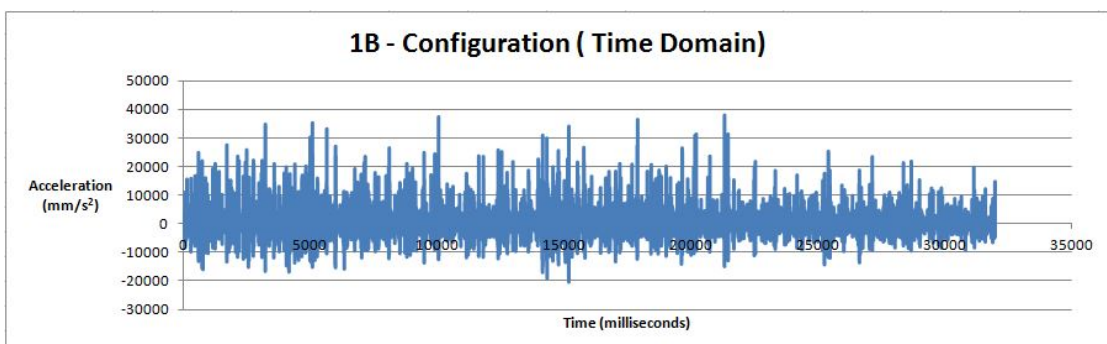


FIGURE 5.18: Acceleration results in time domain for configuration 1B

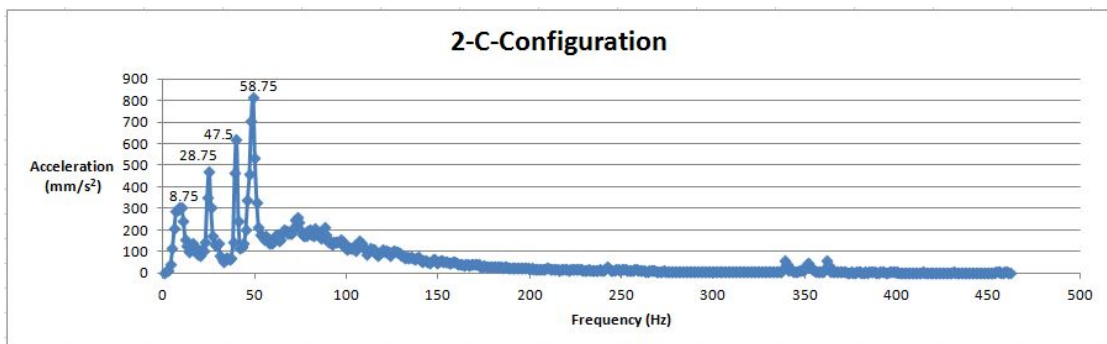


FIGURE 5.19: Acceleration results in frequency domain for configuration 2C

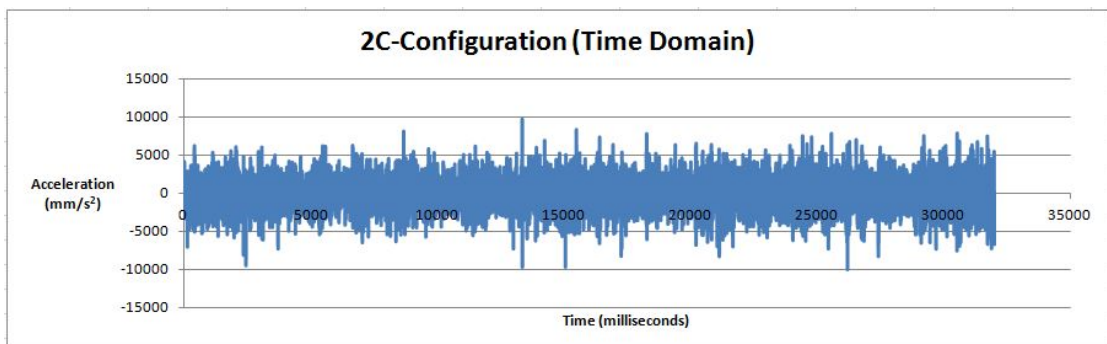


FIGURE 5.20: Acceleration results in time domain for configuration 2C

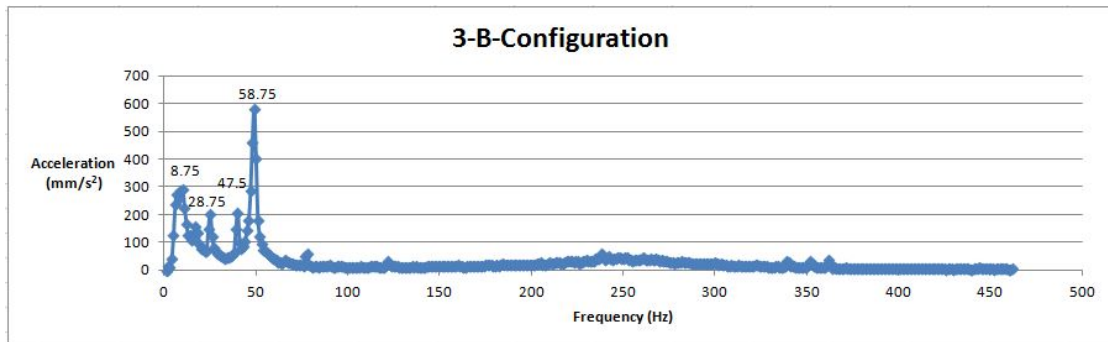


FIGURE 5.21: Acceleration results in frequency domain for configuration 3B

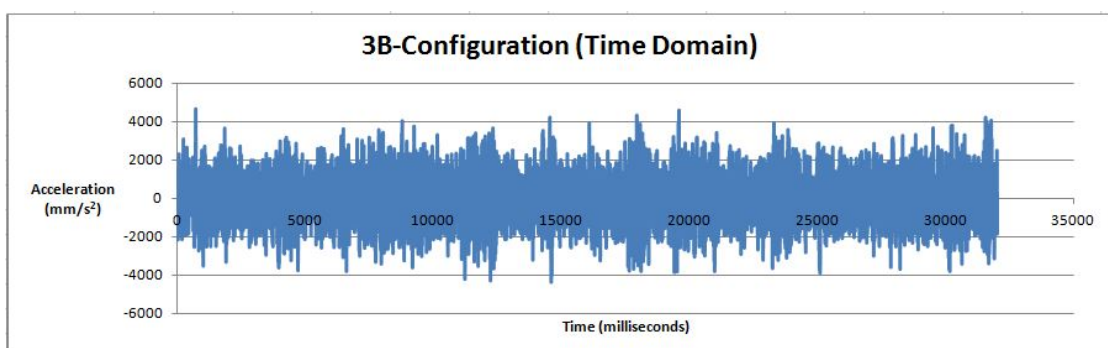


FIGURE 5.22: Acceleration results in time domain for configuration 3B

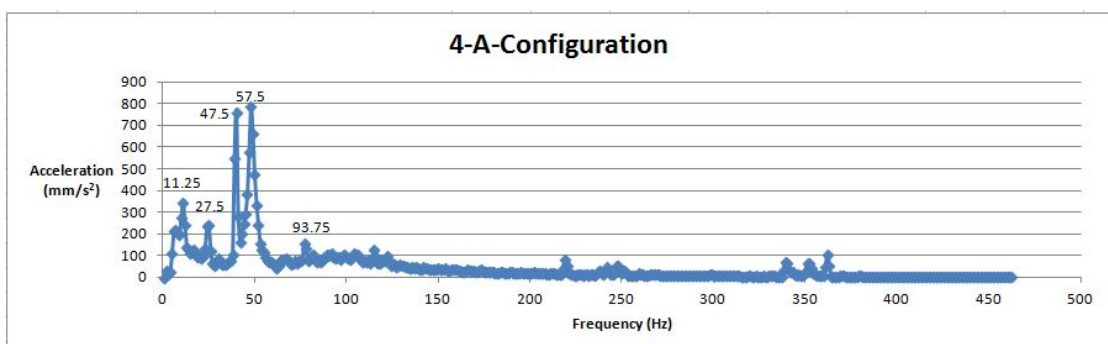


FIGURE 5.23: Acceleration results in frequency domain for configuration 4A

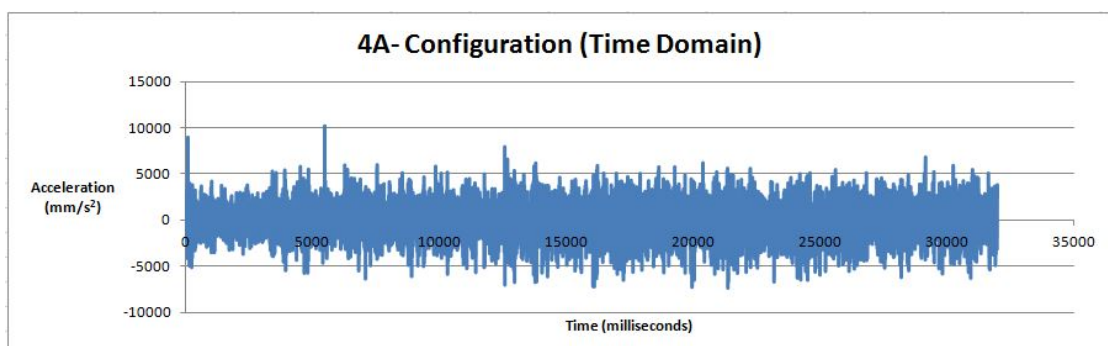


FIGURE 5.24: Acceleration results in time domain for configuration 4A

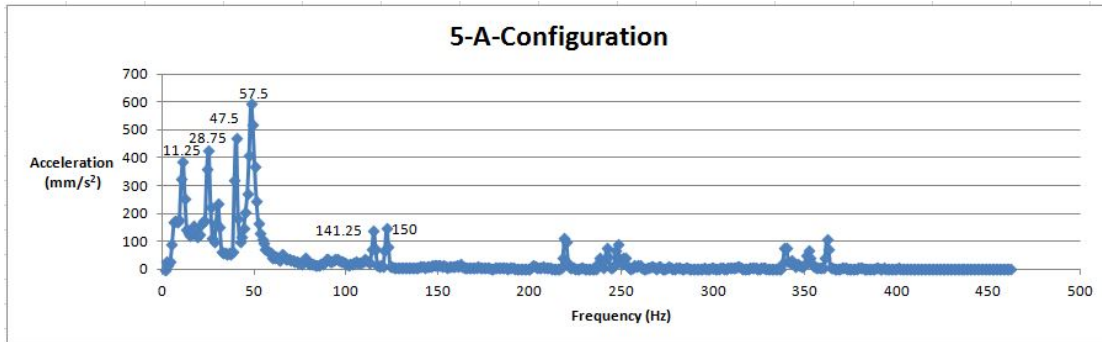


FIGURE 5.25: Acceleration results in frequency domain for configuration 5A

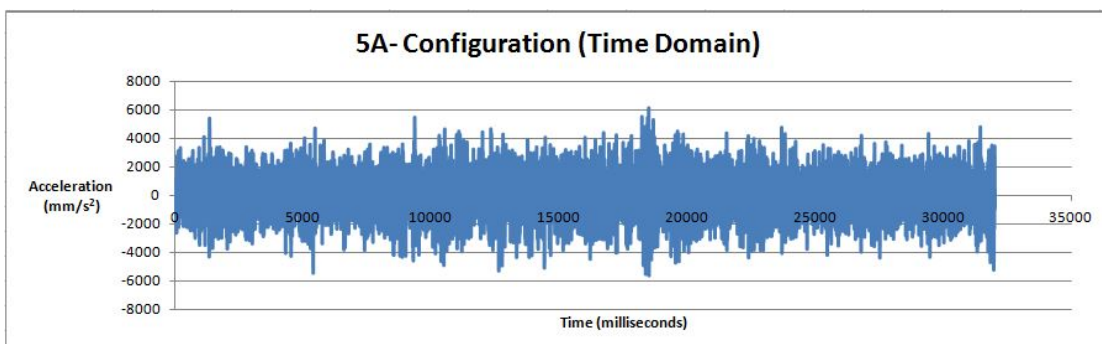


FIGURE 5.26: Acceleration results in time domain for configuration 5A

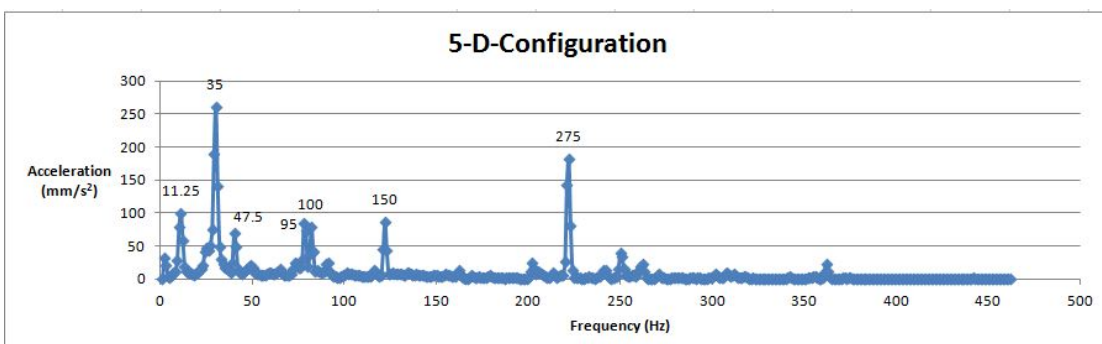


FIGURE 5.27: Acceleration results in frequency domain for configuration 5D

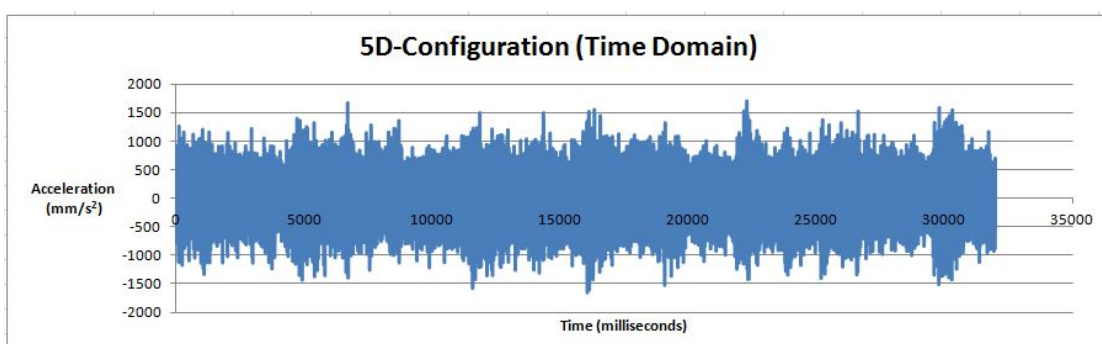


FIGURE 5.28: Acceleration results in time domain for configuration 5D

Fig. 5.17-5.29 shows the acceleration data in frequency and time domain, for the forced wet vibration of the rudder under propeller gust. As from dry and wet vibration results, $\omega_N = 87.5$ Hz, $\omega_{wet} = 56.25$ Hz and propeller-induced-vibration frequency is $\frac{rpm}{60} \times 4 = 46.67$ Hz for four-bladed propeller revolving at roughly 700 rpm. The peaks in the frequency spectrum show the abscissa of the frequency spectrum i.e. excited frequencies. As the propeller wake loading acts on the rudder in impulses with PIV frequency, and the PIV period is greater than the fundamental time period, the rudder gets enough time to vibrate at its wet natural frequency, as the external forcing on the rudder between two consecutive hydrodynamic impulses is zero. Hence, the **Fig. 5.17-5.29** shows the excitation of wet natural frequency 56.25 Hz, along with the propeller-induced-vibration frequency 47.5 Hz.

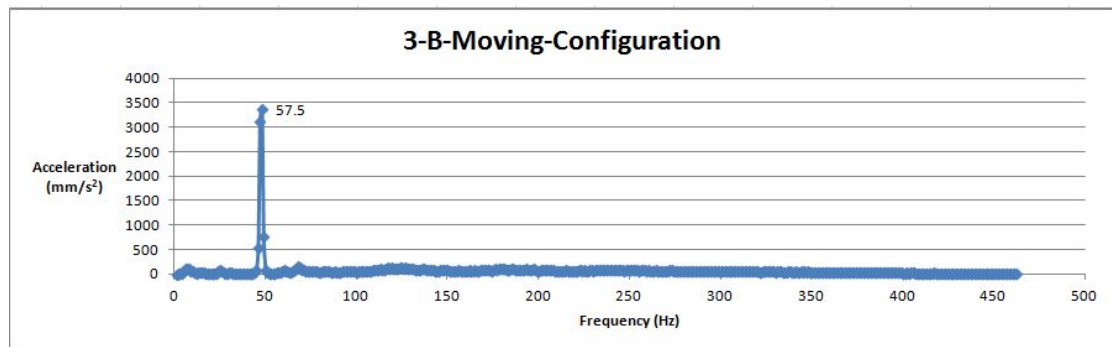


FIGURE 5.29: Acceleration results in frequency domain for configuration 3B at non-zero speed

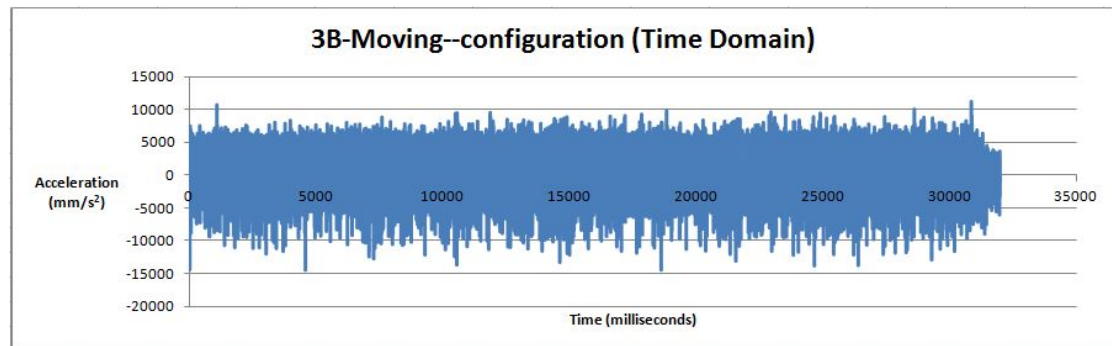


FIGURE 5.30: Acceleration results in time domain for configuration 3B at non-zero carriage speed

Table 5.5 shows the variation of dry natural frequencies and wet natural frequencies at various positions of the accelerometer. Due to the added inertia of the surrounding water, the fundamental natural frequency decreases from 65.00 Hz to 56.25 Hz, along with other frequencies.

TABLE 5.5: Comparison of free dry and wet natural frequencies for different configuration of accelerometer

Dry	Dry natural frequencies (Hz)	Wet	Wet Natural frequencies
D-3A	20 , 65.00 , 87.5 , 152.5	W-3A	10.00 , 56.25 , 78.75 , 117.5
D-3C	20 , 65.00 , 87.5 , 152.5	W-3C	10.00 , 56.25 , 78.75 , 117.5
D-5A	20 , 65.00 , 85.0 , 151.2	W-5A	11.25 , 55.00 , 78.75 , 115.0
D-5C	20 , 63.75 , 87.5 , 152.5	W-5C	10.00 , 55.00 , 78.75 , 117.5

Table 5.6 shows the frequencies excited most dominantly in propeller-induced-vibration test for different configurations of the accelerometer. As the wake loading on the rudder is in the form of periodic impulses, acting at PIV frequency, the rudder gets also excited at wet natural frequency in between two consecutive impulses. However, when the carriage has non-zero speed, the *rpm* of the propeller is 536. The PIV frequency corresponding to this *rpm* is 35.73; but in the results, the rudder is seen to be excited only at the wet natural frequency.

TABLE 5.6: Comparison of excitation frequencies with the blade passing frequencies (PIV) for different configuration of accelerometer

Location	Frequencies (Hz)	Location	Frequencies (Hz)
1B	28.75 , 57.5	5A	57.50 , 47.5
2C	58.75 , 47.5	5D	35.00 , 47.5
3B	58.75 , 47.5	3B-Moving	57.5
4A	57.50 , 47.5	PIV	46.67

Chapter 6

Discussion, Conclusion and Future Work

6.1 Discussion

6.1.1 Rudder - I

A study of free dry and wet vibration analysis of Rudder I, in the model scale, is done by the theoretical method. The rudder can be considered as a thin 2-way non-uniform Kirchhoff's plate, with a hollow structure and the interior stiffeners implicitly taken into account. The pivot is modelled as realistically as possible, with one translational and two torsional degrees of freedom. The internal stiffening arrangement of rudder is taken into account by the technique of 'smeared' thickness. Since a submerged vibrating body is affected by the fluid inertia, the need for wet vibration analysis becomes significant. The added mass is calculated by the Potential flow theory and 2D strip theory. The 3D added mass is calculated by integrating the 2D added masses of each section along the span of the rudder subjected to the correction factors (to take account of the ends and the modeshapes), dependent on modeshapes itself. The frequencies in the model scale are converted to that of full-scale rudder by using the non-dimensional frequency similarity. As the frequencies of full scale rudder are quite high as compared to propeller induced frequencies (propeller shaft frequency number of blades), the PIV resonance is very unlikely to occur. The fluid inertia of rudder is very high as it reduces the frequencies significantly.

6.1.2 Rudder - II

A theoretical analysis of the forced wet vibration is done for marine Rudder - II. The free dry vibration analysis is done bypassing the cumbersome FEA, facilitated by the generation of the non-uniform beam modeshapes in the two orthogonal directions by the Rayleigh-Ritz method. The 2-way non-mathematical taper of the rudder is considered

to generate the admissible functions in the Galerkin's method. Since the rudder is trapezoidal, and has bi-quadratically varying plate rigidity due to the hollow interior, the natural frequencies are all unique. The Eigen vectors each have one dominant term only, preventing any conjugate frequencies. The wet, free vibration of the submerged rudder is done bypassing the cumbersome CFD, by the 3D panel method. The inertia of motion of each modeshape self-couples and cross-couples with the inertia of motion of every modeshape. The added mass associated with each mode depends on the volume enclosed under each modeshape.

6.1.3 Rudder - III

The experiment on the free dry and wet, forced wet vibration of the spade Rudder - III is done here. The significant decrease in natural frequencies in wet vibration is found compared to that in dry vibration due to added virtual mass increment (AVMI). The rudder was found to be excited on the PIV frequencies and also on the wet natural frequency as the forcing on the rudder is in terms of impulses acting at blade passing frequency. As wet natural period is lower compared to PIV period, it gives enough time to rudder to vibrate at wet natural frequency between two consecutive impulses because, here, the rudder acts, as if it vibrates under water without any external force.

6.2 Conclusion

6.2.1 Rudder - I

Galerkin's method is shown to give appreciably good estimates of the rudder dry and wet natural frequencies, bypassing the computationally cumbersome Finite Element Method. The two-way tapered hollow rudder can be safely considered as a Kirchhoff's plate for initial studies of dynamic behaviour. The parametric studies give insights into the influence of the taper ratios and the pivot positions on the natural frequencies of beam vibration. The Galerkin's I method over-predicts the plate flexural rigidity, as its components are considered on an average over the span/chord. The Galerkin's II method is superior as it considers the plate flexural rigidity locally. The vibration analysis to calculate full scale rudder frequencies can be done by following the theoretical procedure for modal scale and scaling the frequencies down by non-dimensional similarity.

6.2.2 Rudder - II

The propeller slipstream causes a harmonically varying load on the rudder, whose spatial distribution has been calculated empirically. It varies parabolically over the span, with the maximum at the mean chord. Increasing the rudder angle cause an increase in the angle of attack of the flow on the rudder. Given the NACA profile of the chord

section, this will leads to increase in the lift and the drag coefficients subsequently. This increases the total normal hydrodynamic pressure on the rudder, leading to larger displacements and dynamic stresses. The shaft frequency is considered as 80 rpm, with a 5-bladed propeller. The PIV frequency is 6.67 Hz. The Galerkin's method generates a dry frequency of 6.74 Hz, when the 1st non-uniform modeshape in both the span-wise and the chord-wise directions dominate to generate a plate modeshape.

6.2.3 Rudder - III

The forced wet vibration experiment of rudder in the wake of propeller is done at bollard-pull condition i.e. no carriage speed. If the external force is impulsive and periodic, and if PIV frequency is less than wet natural frequency, the rudder vibrates at PIV frequency during the impulsive loading and at wet natural frequency during the time lag between two consecutive impulses.

6.3 Future Work

6.3.1 Theoretical

1. Structure

- Parametric study of dry plate vibration
- Inclusion of rigid body modeshapes
- Up gradation of spade rudder to horn rudder
- Inclusion of interior bulkhead and stiffeners in rudder vibration analysis

2. Hydrodynamics

- Wet plate vibration, and its parametric study
- Added mass calculation by 3D source distribution technique
- Partially submerged rudder vibration (Light ship arrival condition).
- Turbulent load analysis

3. Design

- Forced vibration of rudder under periodic loading (propeller wake loading)
- Non-linear rudder flutter study
- Pivot structural design recommendations
- Fatigue analysis

6.3.2 Numerical

1. Commercial tool ANSYS
 - Modelling of pivoted rudder (Rudder - I and Rudder - II)
 - Forced vibration under given external force
2. Fluent
 - Modelling of rudder under water for wet plate vibration
 - Modeling for ship hull wake and propeller wake
 - Rudder vibration behind ship hull and propeller wake

6.3.3 Experimental

1. Forced wet vibration at non-zero forward carriage speed
2. Stresses calculation at various points on rudder by strain gauges
3. Signature detection of enemy ships by analysing rudder in the waves generated from a considerable distance.
4. Propeller - Hull - Rudder trio interaction

Appendix A

Coefficient Matrices

A.1 Chord-wise 2-span beam coefficient matrix

$$M_{11}=1 \quad , \quad M_{12}=0 \quad , \quad M_{13}=1 \quad , \quad M_{14}=0 \quad , \quad M_{15}=0 \quad , \quad M_{16}=0 \quad , \quad M_{17}=0 \quad ,$$

$$M_{18}=0 \quad , \quad M_{21}=0 \quad , \quad M_{22}=-1 \quad , \quad M_{23}=0 \quad , \quad M_{24}=1 \quad , \quad M_{25}=0 \quad , \quad M_{26}=0 \quad ,$$

$$M_{27}=0 \quad , \quad M_{28}=0 \quad , \quad M_{31}=0 \quad , \quad M_{32}=0 \quad , \quad M_{33}=0 \quad , \quad M_{34}=0 \quad , \quad M_{35}=-1 \quad ,$$

$$M_{36}=0 \quad , \quad M_{37}=1 \quad , \quad M_{38}=0 \quad , \quad M_{41}=0 \quad , \quad M_{42}=0 \quad , \quad M_{43}=0 \quad , \quad M_{44}=0 \quad ,$$

$$M_{45}=0 \quad , \quad M_{46}=-1 \quad , \quad M_{47}=0 \quad , \quad M_{48}=-1 \quad , \quad M_{51}=-\sin(\beta_y l_2) \quad , \quad M_{52}=\cos(\beta_y l_1),$$

$$M_{53}=\sinh(\beta_y l_1) \quad , \quad M_{54}=\cosh(\beta_y l_1) \quad , \quad M_{55}=\sin(\beta_y l_2) \quad , \quad M_{56}=-\cos(\beta_y l_2) \quad ,$$

$$M_{57}=-\sinh(\beta_y l_2) \quad , \quad M_{58}=-\cosh(\beta_y l_2) \quad , \quad M_{61}=\cos(\beta_y l_1) \quad , \quad M_{62}=\sin(\beta_y l_1) \quad ,$$

$$M_{63}=\cosh(\beta_y l_1) \quad , \quad M_{64}=\sinh(\beta_y l_1) \quad , \quad M_{65}=\cos(\beta_y l_2) \quad , \quad M_{66}=\sin(\beta_y l_2) \quad ,$$

$$M_{67}=\cosh(\beta_y l_2) \quad , \quad M_{68}=\sinh(\beta_y l_2) \quad , \quad M_{71}=\sin(\beta_y l_1)-\left(\frac{K_T}{\beta_y^3 EI}\right)\cos(\beta_y l_1) \quad ,$$

$$M_{72}=-\cos(\beta_y l_1)-\left(\frac{K_T}{\beta_y^3 EI}\right)\sin(\beta_y l_1) \quad , \quad M_{73}=\sinh(\beta_y l_1)-\left(\frac{K_T}{\beta_y^3 EI}\right)\cosh(\beta_y l_1) \quad ,$$

$$M_{74}=\cosh(\beta_y l_1)-\left(\frac{K_T}{\beta_y^3 EI}\right)\sinh(\beta_y l_1) \quad , \quad M_{75}=-\sin(\beta_y l_2) \quad , \quad M_{76}=\cos(\beta_y l_2) \quad ,$$

$$M_{77}=-\sinh(\beta_y l_2) \quad , \quad M_{78}=-\cosh(\beta_y l_2) \quad , \quad M_{81}=-\cos(\beta_y l_1)+\left(\frac{K_{\theta_c}}{\beta_y EI}\right)\sin(\beta_y l_1) \quad ,$$

$$M_{82} = -\sin(\beta_y l_1) - \left(\frac{K_{\theta_c}}{\beta_y EI} \right) \cos(\beta_y l_1) , \quad M_{83} = \sinh(\beta_y l_1) - \left(\frac{K_{\theta_c}}{\beta_y EI} \right) \sinh(\beta_y l_1) ,$$

$$M_{84} = \sinh(\beta_y l_1) - \left(\frac{K_{\theta_c}}{\beta_y EI} \right) \cosh(\beta_y l_1) , \quad M_{85} = \cos(\beta_y l_2) , \quad M_{86} = \sin(\beta_y l_2) ,$$

$$M_{87} = -\cosh(\beta_y l_2) , \quad M_{88} = -\sinh(\beta_y l_2)$$

A.2 Span-wise beam coefficient matrix

$$N_{11} = -1 , \quad N_{12} = 0 , \quad N_{13} = 1 , \quad N_{14} = 0 , \quad N_{21} = 0 , \quad N_{22} = -1 , \quad N_{23} = 0 ,$$

$$N_{24} = 1 , \quad N_{31} = \sin(\beta_x L) - \left(\frac{K_T}{\beta_x^3 EI} \right) \cos(\beta_x L) , \quad N_{32} = -\cos(\beta_x L) - \left(\frac{K_T}{\beta_x^3 EI} \right) \sin(\beta_x L) ,$$

$$N_{33} = \sinh(\beta_x L) - \left(\frac{K_T}{\beta_x^3 EI} \right) \cosh(\beta_x L) , \quad N_{34} = \cosh(\beta_x L) - \left(\frac{K_T}{\beta_x^3 EI} \right) \sinh(\beta_x L) ,$$

$$N_{41} = -\cos(\beta_x L) + \left(\frac{K_{\theta_s}}{\beta_x EI} \right) \sin(\beta_x L) , \quad N_{42} = -\sin(\beta_x L) - \left(\frac{K_{\theta_s}}{\beta_x EI} \right) \cos(\beta_x L) ,$$

$$N_{43} = \cosh(\beta_x L) - \left(\frac{K_{\theta_s}}{\beta_x EI} \right) \sinh(\beta_x L) , \quad N_{44} = \sinh(\beta_x L) - \left(\frac{K_{\theta_s}}{\beta_x EI} \right) \cosh(\beta_x L)$$

Appendix B

Joukowski Transformation

The airfoil is been represented in the (ξ, ς) coordinate system, which depends parametrically on local variable θ , where $0 \leq \theta \leq \pi$. Thus,

$$\xi = b \cos \theta \quad \text{and} \quad \varsigma = b e(1 + \cos \theta) \sin \theta \quad (\text{B.1})$$

Therefore, Chord length = $2b$.

B.1 Average chord section thickness

Average thickness of airfoil is calculated by integrating twice of ordinate over the whole local variable range, as

$$\begin{aligned} h_{avg} &= \frac{2 \int_{-b}^b \varsigma(\xi) d\xi}{\int_{-b}^b d\xi} \Rightarrow - \int_0^\pi e(1 + \cos \theta) \sin \theta (-b \sin \theta) d\theta \\ &\Rightarrow be \int_0^\pi \sin^2 \theta d\theta - \int_0^\pi \sin^2 \theta \cos \theta d\theta \\ &\Rightarrow \frac{be}{2} \int_0^\pi (1 - \cos 2\theta) d\theta - \frac{\sin^3 \theta}{3} \Big|_0^\pi \\ &\Rightarrow \frac{be}{2} \left[\theta - \frac{\sin 2\theta}{2} \right]_0^{2\pi} - 0 \Rightarrow \frac{be\pi}{2} \end{aligned} \quad (\text{B.2})$$

Maximum thickness occurs at $\theta = \pm \frac{\pi}{3}$, Therefore,

$$h_{max} = \frac{3\sqrt{3}be}{4}$$

B.2 Slenderness ratio in beams

The slenderness ratio is defined as the ratio of the average thickness to the length of beam. For chord-wise direction, the slenderness ratio is

$$\frac{\frac{4be}{\pi}}{2b} \quad or \quad \frac{2e}{\pi}$$

for span-wise direction, it is

$$\frac{\frac{4be}{\pi}}{L} \quad or \quad \frac{2e}{\pi L}$$

B.3 Area of the aerofoil

The area of the aerofoil can be expressed as :

$$\begin{aligned} \text{Area} &= \int_{-b}^b 2\xi d\xi \Rightarrow - \int_0^\pi 2\xi(\theta) \frac{d\xi}{d\theta} d\theta \\ &\Rightarrow -2 \int_0^\pi be(1 + \cos \theta) \sin \theta (-b \sin \theta) d\theta \\ &\Rightarrow \int_0^\pi 2b^2 e(1 + \cos \theta) \sin^2 \theta d\theta = \pi eb^2 \end{aligned} \quad (\text{B.3})$$

B.4 Centroid of the aerofoil

The centroid of the aerofoil from the origin can be expressed as the ratio of first moment of area about origin to the area itself.

$$\begin{aligned} \text{Centroid} &= \frac{\int_{-b}^b 2\xi \xi d\xi}{\int_{-b}^b 2\xi d\xi} \Rightarrow \frac{- \int_0^\pi 2\xi(\theta) \xi(\theta) \frac{d\xi}{d\theta} d\theta}{- \int_0^\pi 2\xi(\theta) \frac{d\xi}{d\theta} d\theta} \\ &\Rightarrow \frac{-2 \int_0^\pi be(1 + \cos \theta) \sin \theta (b \cos \theta) (-b \sin \theta) d\theta}{\pi eb^2} \\ &\Rightarrow \frac{2b}{\pi} \int_0^\pi (1 + \cos \theta) \cos \theta \sin^2 \theta d\theta = \frac{b}{4} \end{aligned} \quad (\text{B.4})$$

B.5 Moment of inertia of the aerofoil in yaw (about CG)

$$\begin{aligned} \text{Moment of inertia} &= \int_{-b}^b 2\xi \xi^2 d\xi \\ &\Rightarrow - \int_0^\pi 2\xi(\theta) [\xi(\theta)]^2 \frac{d\xi}{d\theta} d\theta \\ &\Rightarrow -2 \int_0^\pi be(1 + \cos \theta) \sin \theta (b \cos \theta)^2 (-b \sin \theta) d\theta \end{aligned} \quad (\text{B.5})$$

$$\Rightarrow 2 \int_0^\pi b^4 e(1 + \cos \theta) \sin^2 \theta \cos^2 \theta d\theta = \frac{\pi b^4 e}{4}$$

B.6 Normal vector on aerofoil perimeter

The tangent at a point (ξ, ς) on the perimeter of the aerofoil can be expressed as:

$$\begin{aligned} \text{Tangent angle} &= \tan^{-1} \left[\frac{d\varsigma}{d\xi} \right] & (B.6) \\ \Rightarrow \tan^{-1} \left[\frac{d\varsigma}{d\theta} \frac{d\theta}{d\xi} \right] &\Rightarrow \tan^{-1} \left[\frac{be(\cos \theta + \cos 2\theta)}{-b \sin \theta} \right] \\ \Rightarrow \tan^{-1} \left[\frac{e(\cos \theta + \cos 2\theta)}{-\sin \theta} \right] \end{aligned}$$

Therefore, the normal angle can be expressed as

$$\text{Normal angle} = \tan^{-1} \left[\frac{e(\cos \theta + \cos 2\theta)}{-\sin \theta} \right] + \frac{\pi}{2} \quad (B.7)$$

Appendix C

Galerkin II : Expansion of biharmonic operator

$$\begin{aligned}
F_1 &= A_{rs} \int_0^L p_{xxxx} \varphi_{sr}^2(x) dx \int_0^C q \varphi_{cs}^2(y) dy \\
F_2 &= 4 \sum_{j=1}^{\infty} \sum_{l=1}^{\infty} A_{jl} \int_0^L p_{xxx} \varphi'_{sj}(x) \varphi_{sr} dx \int_0^C q \varphi_{cl}(y) \varphi_{cs}(y) dy \\
F_3 &= 6 \sum_{j=1}^{\infty} \sum_{l=1}^{\infty} A_{jl} \int_0^L p_{xx} \varphi''_{sj}(x) \varphi_{sr} dx \int_0^C q \varphi_{cl}(y) \varphi_{cs}(y) dy \\
F_4 &= 4 \sum_{j=1}^{\infty} \sum_{l=1}^{\infty} A_{jl} \int_0^L p_x \varphi'''_{sj}(x) \varphi_{sr} dx \int_0^C q \varphi_{cl}(y) \varphi_{cs}(y) dy \\
F_5 &= A_{rs} \int_0^L p \beta_{sr}^4 \varphi_{sr}^2(x) dx \int_0^C q \varphi_{cs}^2(y) dy \\
M_1 &= 2 \sum_{j=1}^{\infty} \sum_{l=1}^{\infty} A_{jl} \int_0^L p_{xx} \varphi_{sj}(x) \varphi_{sr} dx \int_0^C q_{yy} \varphi_{cl}(y) \varphi_{cs}(y) dy \\
M_2 &= 4 \sum_{j=1}^{\infty} \sum_{l=1}^{\infty} A_{jl} \int_0^L p_x \varphi'_{sj}(x) \varphi_{sr} dx \int_0^C q_{yy} \varphi_{cl}(y) \varphi_{cs}(y) dy \\
M_3 &= 2\mu \sum_{j=1}^{\infty} \sum_{l=1}^{\infty} A_{jl} \int_0^L p \varphi''_{sj}(x) \varphi_{sr} dx \int_0^C q_{yy} \varphi_{cl}(y) \varphi_{cs}(y) dy \\
M_4 &= 4 \sum_{j=1}^{\infty} \sum_{l=1}^{\infty} A_{jl} \int_0^L p_{xx} \varphi_{sj}(x) \varphi_{sr} dx \int_0^C q_y \varphi'_{cl}(y) \varphi_{cs}(y) dy \\
M_5 &= 16(1-\mu) \sum_{j=1}^{\infty} \sum_{l=1}^{\infty} A_{jl} \int_0^L p_x \varphi'_{sj}(x) \varphi_{sr} dx \int_0^C q_y \varphi'_{cl}(y) \varphi_{cs}(y) dy \\
M_6 &= 4 \sum_{j=1}^{\infty} \sum_{l=1}^{\infty} A_{jl} \int_0^L p \varphi''_{sj}(x) \varphi_{sr} dx \int_0^C q_y \varphi'_{cl}(y) \varphi_{cs}(y) dy \\
M_7 &= 2\mu \sum_{j=1}^{\infty} \sum_{l=1}^{\infty} A_{jl} \int_0^L p_{xx} \varphi_{sj}(x) \varphi_{sr} dx \int_0^C q \varphi''_{cl}(y) \varphi_{cs}(y) dy \\
M_8 &= 4 \sum_{j=1}^{\infty} \sum_{l=1}^{\infty} A_{jl} \int_0^L p_x \varphi'_{sj}(x) \varphi_{sr} dx \int_0^C q \varphi''_{cl}(y) \varphi_{cs}(y) dy \\
M_9 &= 2 \sum_{j=1}^{\infty} \sum_{l=1}^{\infty} A_{jl} \int_0^L p \varphi''_{sj}(x) \varphi_{sr} dx \int_0^C q \varphi''_{cl}(y) \varphi_{cs}(y) dy \\
L_1 &= A_{rs} \int_0^L p \varphi_{sr}^2(x) dx \int_0^C q_{yyyy} \varphi_{cs}^2(y) dy \\
L_2 &= 4 \sum_{j=1}^{\infty} \sum_{l=1}^{\infty} A_{jl} \int_0^L p \varphi_{sj}(x) \varphi_{sr} dx \int_0^C q_{yyyy} \varphi'_{cl}(y) \varphi_{cs}(y) dy \\
L_3 &= 6 \sum_{j=1}^{\infty} \sum_{l=1}^{\infty} A_{jl} \int_0^L p \varphi_{sj}(x) \varphi_{sr} dx \int_0^C q_{yy} \varphi''_{cl}(y) \varphi_{cs}(y) dy \\
L_4 &= 4 \sum_{j=1}^{\infty} \sum_{l=1}^{\infty} A_{jl} \int_0^L p \varphi_{sj}(x) \varphi_{sr} dx \int_0^C q_y \varphi'''_{cl}(y) \varphi_{cs}(y) dy \\
L_5 &= A_{rs} \int_0^L p \varphi_{sr}^2(x) dx \int_0^C q \beta_{cs}^4 \varphi_{cs}^2(y) dy
\end{aligned}$$

Appendix D

Source Distribution Technique

D.1 3D Constant-Strength Source Distribution Technique

Let say, in the 3D domain around the rudder, the velocity potential satisfying Laplace equation are Φ^{3D} and Ψ^{3D} . Therefore, by using Gauss's theorem, the Green's second identity can be expressed as

$$\int \int_s \left[\Phi^{3D} \frac{\partial \Psi^{3D}}{\partial n} - \Psi^{3D} \frac{\partial \Phi^{3D}}{\partial n} \right] ds = \int \int \int_V \nabla(\Phi^{3D} \nabla \Psi^{3D} - \Psi^{3D} \nabla \Phi^{3D}) dV$$

or

$$\int \int_V \int (\Phi^{3D} \nabla^2 \Psi^{3D} - \nabla \Psi^{3D} \nabla \Phi^{3D} + \nabla \Phi^{3D} \nabla \Psi^{3D} + \Psi^{3D} \nabla^2 \Phi^{3D}) dV = 0 \quad (D.1)$$

Ψ^{3D} is assumed to be the source potential distributed over the surface which include the body, bottom sea bed and free surface, can be expressed as

$$\Psi^{3D} = \frac{1}{4\pi r} \quad (D.2)$$

where r is the distance from the source point to the field point. Substituting Ψ^{3D} in Eq. (D.1),

$$\frac{1}{4\pi} \int \int_s \left[\Phi^{3D} \frac{\partial}{\partial n} \frac{1}{r} - \frac{1}{r} \frac{\partial \Phi^{3D}}{\partial n} \right] ds = -\frac{1}{4\pi} \int \int_{s_\epsilon} \left[\Phi^{3D} \frac{\partial}{\partial n} \frac{1}{r} - \frac{1}{r} \frac{\partial \Phi^{3D}}{\partial n} \right] ds_\epsilon \quad (D.3)$$

Here, $S_\epsilon = 2\pi r^2$, as the sources are been distributed over the surface boundary of the domain and as $\epsilon \rightarrow 0$, Φ^{3D} becomes constant. Therefore, substituting value of S_ϵ and keeping Φ^{3D} constant, we get,

$$\frac{1}{4\pi} \Phi^{3D}(x, y, z) \left(\frac{-1}{r^2} \right) 2\pi r^2 = \frac{-1}{4\pi} \int \int_s \Phi^{3D}(x, y, z) \frac{\partial}{\partial n} \left(\frac{1}{r} \right) ds \quad (D.4)$$

$$\Rightarrow \frac{-1}{2\pi} \Phi^{3D}(x, y, z) \int \int_s \frac{\partial}{\partial n} \left(\frac{1}{r} \right) ds = -\Phi^{3D}(x, y, z)$$

Therefore,

$$\Phi^{3D}(x, y, z) = \frac{-1}{2\pi} \int \int_s \left[\Phi^{3D} \frac{\partial}{\partial n} \frac{1}{r} - \frac{1}{r} \frac{\partial \Phi^{3D}}{\partial n} \right] ds \quad (\text{D.5})$$

After descretizing the surface into 'N' panels, the upper equation becomes

$$\Phi^{3D}(x, y, z) = \frac{-1}{2\pi} \sum_{i=1}^N \left[\Phi_i^{3D} \frac{\partial}{\partial n_i} \frac{1}{r} - \frac{1}{r} \left(\frac{\partial \Phi_i^{3D}}{\partial n_i} \right)_{mode=k} \right] dA_i \quad (\text{D.6})$$

In a six degrees of freedom system,

$$\left(\frac{\partial \Phi_i^{3D}}{\partial n_i} \right)_{mode=k} = [n_i]_k$$

where, $n_k = (n_x, n_y, n_z)$ for $k=1,2,3$

$n_k = (\vec{r} \times \vec{n})_{k-3}$ for $k = 4, 5, 6$

Now,

$$\frac{\partial}{\partial n_i} \frac{1}{r} = \left(\nabla \left(\frac{1}{r} \right) \right) \cdot \vec{n} = \frac{\vec{R} \cdot \vec{n}}{|R|^3}$$

Equation (D.6) can be rewritten as

$$\Phi_j^{3D}(x, y, z) = \frac{-1}{2\pi} \sum_{i=1}^N \left[\Phi_i^{3D} \frac{\vec{R} \cdot \vec{n}}{|R|^3} - \frac{1}{|R_i|} [n_i]_{mode=k} \right] dA_i \quad j \in (1, N) \quad (\text{D.7})$$

If $\alpha(P) = -2\pi$ + effect of self influenced panel,

$$a_{j,i} = \left(\frac{\vec{R} \cdot \vec{n}}{|R|^3} \right) dA_i,$$

$$b_j = \sum_{i=1}^N \frac{1}{|R_i|} [n_i]_{mode=k} dA_i \quad for \quad i \neq j$$

the above equation for $j \in (1, N)$, is been converted into a system of equations which can be expressed as follows, leads to the calculation of 3-dimensional radiation potential.

$$\begin{bmatrix} \alpha(P) & a_{1,1} & \dots & a_{1,N} \\ a_{2,1} & \alpha(P) & \dots & a_{2,N} \\ \vdots & \vdots & \ddots & \vdots \\ M_{N,1} & \dots & \dots & \alpha(P) \end{bmatrix} \begin{bmatrix} \Phi_1^{3D} \\ \Phi_2^{3D} \\ \vdots \\ \Phi_N^{3D} \end{bmatrix} = \begin{bmatrix} b_1 \\ b_2 \\ \vdots \\ b_N \end{bmatrix} \quad (\text{D.8})$$

D.2 2D Constant-Strength Source Distribution Technique

Let say, in the 2D domain around the rudder strips or airfoil sections, the velocity potential satisfying laplace equation are Φ^{2D} and Ψ^{2D} . Therefore, by using Gauss's theorem, the Green's second identity can be expressed as

$$\int_l \left[\Phi^{2D} \frac{\partial \Psi^{2D}}{\partial n} - \Psi^{2D} \frac{\partial \Phi^{2D}}{\partial n} \right] ds = \int \int_s \nabla(\Phi^{2D} \nabla \Psi^{2D} - \Psi^{2D} \nabla \Phi^{2D}) ds$$

or

$$= \int \int_s (\Phi^{2D} \nabla^2 \Psi^{2D} - \nabla \Psi^{2D} \nabla \Phi^{2D} + \nabla \Phi^{2D} \nabla \Psi^{2D} + \Psi^{2D} \nabla^2 \Phi^{2D}) ds$$

or

$$= 0 \quad (D.9)$$

Ψ^{2D} is assumed to be the source potential distributed over the parameter of surface, can be expressed as

$$\Psi^{2D} = \frac{1}{2\pi} \ln r \quad (D.10)$$

After substituting the value of Ψ^{2D} in Eq. (D.9) and repeating the same procedure as of 3D source distribution technique, leads to set of linear equations for calculation of source potentials.

The self influenced panel effect can be obtained as follows

$$\begin{aligned} \int_{-\frac{\Delta s}{2}}^{-\frac{\Delta s}{2}} \frac{1}{2\pi} \ln r dl &= r(lnr - 1)|_{\frac{-\Delta s}{2}}^{-\epsilon} + r(lnr - 1)|_{\epsilon}^{\frac{\Delta s}{2}} \quad as \quad \epsilon \rightarrow 0 \quad (D.11) \\ &\Rightarrow r(-1 + \ln r)|_{\epsilon}^{-\frac{\Delta s}{2}} + r(\ln r - 1)|_{\epsilon}^{\frac{\Delta s}{2}} \\ &\Rightarrow \frac{\Delta s}{2} \left(-1 + \ln \frac{\Delta s}{2} \right) + \frac{\Delta s}{2} \left(\ln \frac{\Delta s}{2} - 1 \right) \\ &\Rightarrow \Delta s \left(\ln \frac{\Delta s}{2} - 1 \right) \end{aligned}$$

Consequent Publications

1. **R. Jindal** and N. Datta , “Free dry and wet vibration of 2-way tapered hollow marine rudder with non-classical pivot : theoretical study”, **Paper accepted**, *ASME 2015 34th International Conference on Ocean, Offshore and Arctic Engineering (OMAE2015)*, St. John’s, Newfoundland, Canada, May 31 - June 5, 2015.
 - Date of submission of first draft : 15 Dec, 2014
 - Date of submission of first draft : 4 March, 2015
 - Speaker : Mr. Rahul Jindal
2. N. Datta and **R. Jindal** , “Wake-induced flutter of 2-way tapered hollow marine spade rudder in non-uniform propeller slipstream”, **Paper accepted**, *ICSV 2015 22nd International Congress on Sound and Vibration (ICSV2015)*, Florence, Italy, July 12-16, 2015.
 - Date of submission of first draft : 31 Jan, 2015
 - Date of submission of first draft : 5 April, 2015
 - Speaker : Dr. N. Datta
3. A.N. Kannamwar, N. Datta and **R. Jindal**, “Free dry and wet vibration : Theoretical and numerical analysis with experimental verification ”, **Paper in progress**, *Journal of Marine Structures*.
 - To be submitted in June 2015
4. **R. Jindal**, N. Datta and A.N. Kannamwar , “Theoretical analysis of free dry and wet vibration of 2-way tapered hollow marine rudder with numerical verification”, **Paper in progress**, *Journal of Ship Research, SNAME*.
 - To be submitted in June 2015
5. N. Datta, Ankit, **R. Jindal** and A.N. Kannamwar , “Free and forced vibration analysis of stiffened pivoted hollow marine spade rudder : theoretical, numerical nad experimental study”, **Paper in progress**, *Ocean Engineering*.
 - To be submitted in June 2015

Bibliography

- [1] S.A. Eftekhari and A.A. Jafari. Accurate variational approach for free vibration of variable thickness thin and thick plates with edges elastically restrained against translation and rotation. *International Journal of Mechanical Sciences*, 68:35–46, 2013.
- [2] A. Kannamwar and N. Datta. Free vibration of marine rudder: Theoretical and numerical analysis with experimental verification. *Proceedings of SNAME maritime convention*, 2014.
- [3] B. Liu and Y. Xing. Exact solutions for free vibrations of orthotropic rectangular mindlin plates. *Composite Structures*, (93):1664–1672, 2011.
- [4] A.W. Leissa. The free vibration of rectangular plates. *Journal of sound and vibration*, 31(3):257–293, 1973.
- [5] M. A. El-Sayad. Rayleigh-ritz method for free vibration of mindlin trapezoidal plates. *International Journal of Emerging Technology and Advanced Engineering*, 2, Issue 5:2250–2459, May 2012.
- [6] Bae J.S. Inman, D.J. and I. Lee. Effects of structural nonlinearity on subsonic aeroelastic characteristics of an aircraft wing with control surfaces. *Journal of fluid and structures*, 19:747–763, 2004.
- [7] E. Bahmyari and A. Rahbar-Ranji. Free vibration analysis of orthotropic plates with variable thickness resting on non-uniform elastic foundation by element free galerkin method. *Journal of mechanical science and technology*, 26(9):2685–2694, 2012.
- [8] Lal R. Gupta, U.S. and S. Rastogi. Chebyshev polynomials in the study of vibrations of non-uniform rectangular plates. *Indian journal of pure applied mathematics*, 27 (10):1017–1028, 1996.
- [9] A. Ergin and B. Ugurlu. Linear vibration analysis of cantilever plates partially submerged in fluid. *Journal of fluid and structures*, 17:927–939, 2003.

- [10] M.E. McCormick and Caracoglia. Hydroelastic instability if low aspect ratio control surfaces. *Journal of offshore mechanics and arctic engineering*, 126:84–89, 2004.
- [11] Tenerov V. Yadykin, Y. and D. Levin. The added mass of a flexible plate oscillating in a fluid. *Journal of fluid and structures*, 17:115–123, 2003.
- [12] C.A. Van Eysden and J.E. Sader. Resonant frequencies of a rectangular cantilever beam immersed in a fluid. *Journal of applied physics*, 100, 2006.
- [13] N. Datta and A.W. Troesch. Dynamic response of kirchhoffs plates to the transient hydrodynamic impact loads. *Journal of Marine systems and Ocean Technology*, 7 (2):79–94, December 2012.
- [14] R. L. Harrington. Rudder torque prediction. *Trans. SNAME*, 1981.
- [15] J. Holtrop and G.G.J. Mennen. A statistical power prediction method. *International shipbuilding progress*, 25, October 1978.
- [16] Bertram V. Practical ship hydrodynamics. *Butterworth-Heinemann, Elsevier*, 1999.

About the author



Mr. Rahul Jindal is a 4th year, undergraduate student enrolled in the Bachelor of Technology course in the department of Ocean Engineering and Naval Architecture, Indian Institute of Technology, Kharagpur for the duration of July 2011 - May 2015. He consistently maintained the department rank #1 for this duration. His specialisation is in the area of rudder vibration. He has been awarded full financial support from his parent institute for attending the OMAE 2015 conference and presenting the first paper generated from his thesis. He was awarded Prof. J.C. Ghosh memorial award for academic excellence at the end of 6th semester. He was also the recipient of Singapore Technologies Engineering scholarship. He is joining the Indian Register of Shipping as an assistant-surveyor in June 2015.

Endorsement



*Mr. Rahul Jindal, has been my undergraduate student from March 2013 to May 2015. He has done his **B.Tech Project (BTP)** under my guidance, during July 2014 May 2015, titled “Theoretical analysis of free and forced dry and wet vibration of 2-way tapered hollow marine rudder with numerical verification”. This required him to study solid mechanics structural dynamics, theoretical hydrodynamics, computational fluid dynamics, and linear and non-linear ordinary and partial differential equations. He sequentially studied in each and every subject area, encompassing his project with diligence and dedication. He has excellent analytical skills, constantly seeking deeper understanding in every work that he does or is assigned. The complete problem of fluid-structure interaction was written efficiently by him in MATLAB, sharpening his coding skills. His 8-month project resulted in two conference publications (in the best academic conferences of the world in the field of Ocean Engineering and Naval Architecture) and two under-review journal papers, submitted to specialized high-impact Elsevier/Springer journals. This is an amazing feat for an undergraduate student of the Department of Ocean Engineering and Naval Architecture, Indian Institute of Technology, Kharagpur. His is very sharp, focused, logical, methodical, extremely hardworking, persistent in his efforts, perseverant in his endeavors (both curricular and independent study), mindful, and has a sharp memory. He works systematically on set targets, and meets his deadlines consistently. He is always ready to take up new challenges, and strive to overcome them with his never-give-up attitude. He manages his time well, and never messes up his schedule. It has been an absolute pleasure to work with such a student for a whole academic year. He is an excellent student in the class, scoring EX grade (Excellent) in all my subjects, i.e. Ship Strength (Spring 2013), Vibration of Floating Structures (Autumn 2013), CAD/CAM in Marine Design and Production (Spring 2014), and High Performance Marine Vehicles (Spring 2014). He is very attentive in the class, and always asks intelligent questions. He successfully completed all of the challenging homeworks in all the above four subjects. As a person, he is well-mannered, obedient, very dependable, consistent to his words, patient, calm, responsible, and well-behaved. He is a very well-brought-up young man, who deserves everything that he achieves now, and in future.*

(NABANITA DATTA)